MULTI-SCALE MODELING OF NANOSECOND PLASMA ASSISTED COMBUSTION

A Dissertation
Presented to
The Academic Faculty

by

Sharath Nagaraja

In Partial Fulfillment
of the Requirements for the Degree
of Doctor of Philosophy in the
School of Aerospace Engineering

Georgia Institute of Technology
August 2014

MULTI-SCALE MODELING OF NANOSECOND PLASMA ASSISTED COMBUSTION

Approved by:

Dr. Vigor Yang, Advisor
School of Aerospace Engineering
Georgia Institute of Technology

Dr. Jechiel Jagoda
School of Aerospace Engineering
Georgia Institute of Technology

Dr. Suresh Menon
School of Aerospace Engineering
Georgia Institute of Technology

Dr. Wenting Sun
School of Aerospace Engineering
Georgia Institute of Technology

Dr. Igor Adamovich
School of Mechanical and Aerospace Engineering
Ohio State University

Date Approved: May 8, 2014

To my wife and parents for their encouragement and sacrifices

ACKNOWLEDGEMENTS

This work was supported by MURI research grant FA9550-09-0602 from the Air Force Office of Scientific Research. The support and encouragement of Dr. Chiping Li and the MURI team is greatly appreciated.

I wish to express my deepest gratitude to my thesis advisor Prof. Vigor Yang for his valuable guidance, continuous support and encouragement throughout the course of my PhD. His rigorous pursuit of perfection, responsiveness, super-active work style, and encouraging students to become independent and ambitious researchers have changed my outlook towards life. I would also like to thank Profs. Jechiel Jagoda, Suresh Menon, Wenting Sun and Igor Adamovich for agreeing to serve on my thesis committee and providing helpful comments on the work.

I am especially indebted to Prof. Igor Adamovich for patiently mentoring and answering my numerous questions about the various aspects of plasma assisted combustion. He was of invaluable help in defining my research plan and key issues to address, and for the fruitful collaboration which resulted in several publications.

Special thanks to Prof. Seitzman for his important contributions to my education at Georgia Tech. I would also like to thank Prof. Jagoda, Margaret Ojala, Susan Jackson, and staff of School of Aerospace Engineering for their patient assistance at numerous occasions during my studies at Georgia Tech. I would also like to thank friends and colleagues at Georgia Tech, for making this the most enjoyable period of my life.

Finally, I could not have successfully completed this journey without the encouragement, help and sacrifices of my family.

TABLE OF CONTENTS

LIST OF FIGURES

NOMENCLATURE

a_i - e_i	Curve-fit coefficients obtained from BOLSIG solutions
$C_{p,k}$	Specific heat at constant pressure of species *k*
D_k, D_i,	Diffusion coefficient of species *k*, ion, and electron energy, $cmV^{-1}s^{-1}$
E/N	Ratio of electric field to gas number density, *Td*
EEDF	Electron energy distribution function
F^{EHD}	Electro-hydrodynamic force per unit volume
f	Electron transport or reaction rate parameter
G(t)	A non-dimensional heat transfer parameter
h	Mixture enthalpy per unit mass, Jkg^{-1}
h_f^0	Enthalpy of formation at constant pressure of species *k*
J_k, J_e	Number density flux of species and electron respectively, $cm^{-2}s^{-1}$
J_ε	Electron Energy Flux, $eVcm^{-2}s^{-1}$
J_+, J_-	Net positive and negative charge fluxes
$J_{+,s}, J_{-,s}, J_{e,s}, J_{\varepsilon,s}$	Electron, positive ion, negative ion, and electron energy fluxes at the boundary wall
k_g, k_{dw}	Thermal conductivity of quartz (1.3 $Wm^{-1}K^{-1}$), and of the gas mixture
T_b	Wall boundary temperature, *K*
L	Gap length, *cm*
l_d	Thickness of the dielectric layer, *cm*
M	Average molecular mass of air, *kg*
m_e	Electron mass, *kg*
n_k , n_e	Number density of species *k* , and electrons respectively, cm^{-3}
n_ε	Electron energy density, $eV\,cm^{-3}$

$\boldsymbol{n}$	Normal vector pointing outwards
p	Pressure, $kgcm^{-1}s^{-1}$
q_k	Charge number (-1 for -ve ions and electrons, +1 for +ve ions and 0 for neutrals)
q_j	Energy flux from heat conduction and diffusion
Q^{JH}	Heat release rate from Joule heating
Q_ε	Rate of electron energy production, $eVcm^{-3}s^{-1}$
T_i, T_e, T_g	Ion, electron, and gas temperature respectively, K
T_{se}	Temperature of secondary electrons ejected from the surface
T_b, T_{amb}, T_{gw}	Boundary, external ambient, and gas temperature at a distance Δx from the wall
$\boldsymbol{u}$	Convection velocity of the gas mixture, cms^{-1}
u_i, u_j	Flow velocity components in *ith* and *jth* directions, respectively.
V_{gap}	Gap voltage

Greek Symbols

γ_s	Secondary electron emission coefficient for ionic species colliding with the surface
ΔE_i	Heat of *ith* reaction with reaction rate r_i ($cm^{-3}\ s^{-1}$), eV
ε	Electron energy, eV
ϵ_d	Dielectric constant (4.8 for quartz)
κ	Dynamic viscosity, $kgcm^{-1}s^{-1}$
λ	Thermal conductivity of the gas mixture, $Wcm^{-1}K^{-1}$
μ_k, μ_e, μ_ε	Mobility of the kth ion, electron and electron energy, $cm^2V^{-1}s^{-1}$
υ_{el}	Elastic collision frequency of electrons, s^{-1}
ρ	Density of the plasma mixture, $kgcm^{-3}$

ρE	Total energy per unit volume, Jcm^{-3}
τ	Viscous shear stress tensor, $kgcm^{-1}s^{-2}$
φ	Electric potential , V
ω_k	Production term, $cm^{-3}s^{-1}$

Subscripts

amb	External ambient
b	Boundary
d	Dielectric layer
e	Electron
el	Elastic
g	Gas
gap	Gap
gw	Glow discharge
i	Ion
k	Species *k*
p	Constant pressure
s	At the boundary wall
se	Secondary electrons ejected from the surface
ε	Electron energy
+	Positive ion
-	Negative ion

Superscripts

EHD	Electro-hydrodynamic
JH	Joule heating
0	At a reference temperature

SUMMARY

The effect of temperature on fuel-air ignition and combustion (thermal effects) have been widely studied and well understood. However, a comprehensive understanding of nonequilibrium plasma effects (*in situ* generation of reactive species and radicals combined with gas heating) on the combustion process is still lacking. Over the past decade, research efforts have advanced our knowledge of electron impact kinetics and low temperature chain branching in fuel-air mixtures considerably. In contrast to numerous experimental investigations, research on modeling and simulation of plasma assisted combustion has received less attention. There is a dire need for development of self-consistent numerical models for construction and validation of plasma chemistry mechanisms. High-fidelity numerical models can be invaluable in exploring the plasma effects on ignition and combustion in turbulent and high-speed flow environments, owing to the difficulty in performing spatially resolved quantitative measurements.

In this work, we establish a multi-scale modeling framework to simulate the physical and chemical effects of nonequilibrium, nanosecond plasma discharges on reacting flows. The model is capable of resolving electric field transients and electron impact dynamics in sub-*ns* timescales, as well as calculating the cumulative effects of multiple discharge pulses over *ms* timescales. Detailed chemistry mechanisms are incorporated to provide deep insight into the plasma kinetic pathways.

The modeling framework is utilized to study ignition of H_2-air mixtures subjected to pulsed, nanosecond dielectric barrier discharges in a plane-to-plane geometry. The key kinetic pathways responsible for radicals such as O, H and OH generation from nanosecond discharges over multiple voltage pulses (*ns-ms* timescales) are quantified.

The relative contributions of plasma thermal and kinetic effects in the ignition process are presented. The plasma generated radicals trigger partial fuel oxidation and heat release when the temperature rises above 700 K, after which the process becomes self-sustaining leading to igntion. The ignition kernel growth is primarily due to local plasma chemistry effects rather than flame propagation, and heat transport does not play a significant role. The nanosecond pulse discharge plasma excitation resulted in nearly simultaneous ignition over a large volume, in sharp contrast to hot-spot igniters.

Next, the effect of nanosecond pulsed plasma discharges on the ignition characteristics of nC_7H_{16} and air in a plane-to-plane geometry is studied at a reduced pressure of 20.3 kPa. The plasma generated radicals initiate and significantly accelerate the H abstraction reaction from fuel molecules and trigger a "self-accelerating" feedback loop via low-temperature kinetic pathways. Application of only a few discharge pulses at the beginning reduces the initiation time of the first-stage temperature rise by a factor of 10. The plasma effect after the first stage is shown to be predominantly thermal.

A novel plasma-flame modeling framework is developed to study the direct coupling of steady, laminar, low-pressure, premixed flames to highly non-equilibrium, nanosecond-pulsed plasma discharges. The simulations are performed with and without a burst of 200 nanosecond discharge pulses to quantify the effect of non-equilibrium plasma on a pre-existing lean premixed $H_2/O_2/N_2$ ($\phi = 0.5$) flame at 25 torr. Simulation results showed a significant increase in O and H densities due to plasma chemistry, with peak values increasing by a factor of 6 and a factor of 4, respectively. It is demonstrated that Joule heating alone cannot move the temperature and species profiles as far upstream (i.e. closer to the burner surface) as the pulsed plasma source of the same total power.

LES (large eddy simulation) of ignition and combustion of H_2 jets injected into a supersonic O_2 crossflow is performed. Nanosecond plasma discharges are studied for their potential to produce radicals and impact on the flame-holding process. The plasma has a significant effect on the O atom distribution near the discharge domain as well as in the leeward side of the second jet. The other species distributions, however, remained unchanged with or without plasma. We believe the reason for this behavior was the high jet momentum ratios considered in the present study. The plasma generated radicals were unable to have an effect on the flame development downstream because of the strong penetration of the cold fuel jet.

CHAPTER 1

INTRODUCTION

The high energy density and relatively low cost of fossil fuels make them by far the most popular energy source of the modern world. In the coming years, combustion of fossil fuels will continue to be the dominant energy source as shown in Fig. 1.1 [1]. 9 out of 10 cars will still use internal combustion engines by the year 2040, although a large shift towards hybrid vehicles is predicted [2]. Gas turbines are expected to remain the primary form of aircraft propulsion, and also play a major role in electricity generation through natural gas fired power-plants [2].

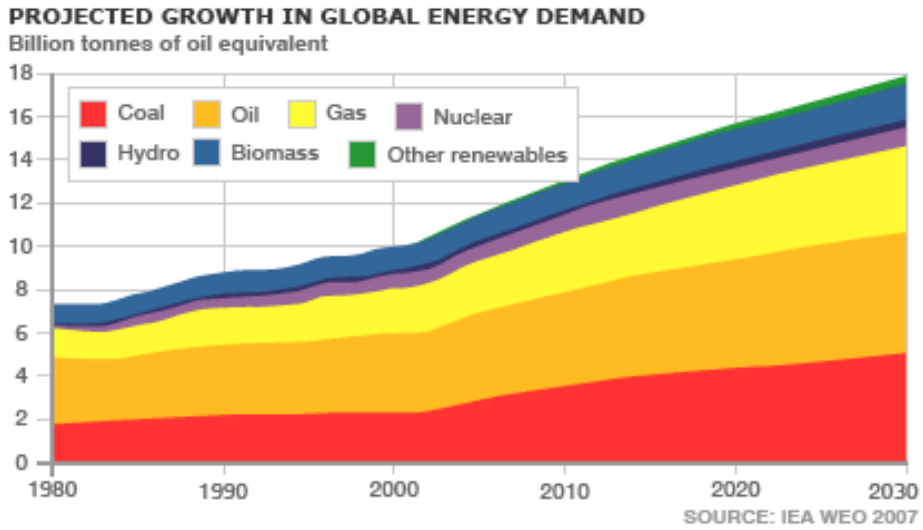

Figure 1.1 Projected growth in global energy demand with contributions from various energy sources (IEA World Energy Outlook 2007)

However, harmful emissions from combustion of fossil fuels remain a grave concern. CO_2 which is a primary byproduct of hydrocarbon combustion has been shown to cause global warming. Combustion also generates several pollutants such as oxides of nitrogen (NO_x), sulphur (SO_x), soot and unburnt hydrocarbons. Stringent government

regulations have been put in place to improve air quality and reduce global warming. Consumers are demanding higher fuel efficiency from engine manufacturers because of increasing fuel prices. Massive investments in renewable and clean sources of energy are having a noticeable impact on the global energy mix. Demand for greater efficiency and stringent emission regulations have pushed the modern combustion systems to operate close to the lean flammability limits. The latest generation gas turbines use the lean premixed combustion concept to increase fuel efficiency and reduce flame temperature (NO_x emissions are directly correlated to flame temperatures). Further reduction in emissions and increase in efficiency would require more advanced combustion concepts and innovations.

Development of scramjet combustion systems for hypersonic aircrafts has suffered from issues associated with efficient ignition and flame-holding [3]. At high combustor flow velocities, time available for fuel injection, fuel-air mixing, and combustion can be of the order of 1 ms. Conventional ignition devices such as spark igniters have difficulty in igniting the fuel, and extracting the chemical energy before it blows out of the combustor. Introduction of a cavity in the combustor geometry has shown promise in promoting combustion and flameholding under supersonic flow conditions [3-4]. However, thermoacoustic instabilities have hampered the stable operation of cavity combustors and result in flame oscillations and blowout. In addition, the cavity introduces stagnation pressure losses which reduce the overall engine efficiency. The above challenges have motivated the search for fast and robust ignition methods, and stable flameholding techniques with minimal flow interference in supersonic flow environments.

In recent years, nonequilibrium plasma discharges have shown great promise in improving ignition and combustion characteristics for a variety of fuels in a wide range of operating conditions [5-15]. Nonequilibrium plasma provides a propulsion system designer an opportunity to change the energy branching during ignition from mainly heating (as in equilibrium spark or arc discharges) to excitation of vibrational and electronic states, electron impact dissociation and ionization [5]. Consider the elementary example of H_2 - O_2 ignition to illustrate the benefits of using a nonequilibrium discharge. The kinetics is broadly described by reactions in Eqns. 1.1 to 1.5 [5]. In case of autoignition, the ignition delay time depends on relative rates of chain initiation and branching reactions compared to rates of chain termination process. Chain reactions given in Eqns. 1.1 - 1.3 are endothermic, with their rates rising exponentially with temperature, whereas 1.4 -1.5 are exothermic. Hence, at a given pressure, for low temperatures, rate of branching is lower than termination rates, and overall fuel oxidation proceeds at a slow constant pace. At sufficiently high temperatures, chain branching rates exceed termination rates and radicals concentration increase exponentially, leading to ignition.

$$H_2 + O_2 \rightarrow OH + OH \qquad \Delta H = 78 \text{ kJ/mol} \qquad (1.1)$$

$$H + O_2 \rightarrow OH + O \qquad \Delta H = 70 \text{ kJ/mol} \qquad (1.2)$$

$$H_2 + O \rightarrow OH + H \qquad \Delta H = 8 \text{ kJ/mol} \qquad (1.3)$$

$$H_2 + OH \rightarrow H_2O + H \qquad \Delta H = -62 \text{ kJ/mol} \qquad (1.4)$$

$$H + O_2 + M \rightarrow HO_2 + M \qquad \Delta H = -203 \text{ kJ/mol} \qquad (1.5)$$

Instead of relying on purely thermal means to initiate ignition, one can imagine introducing active radicals and creating additional chain initiation and branching

pathways. For example, electron impact reactions in a plasma discharge can act as a source of radicals, as seen in the following reactions,

$$H_2 + e \rightarrow H + H + e \quad (1.6)$$

$$O_2 + e \rightarrow O + O + e \quad (1.7)$$

Figure 1.2 shows the O_2 dissociation rate constants relative to other chain branching rate constants as a function of temperature. It can be clearly seen that discharge based reaction rates can be two orders greater than the typical chain branching reaction rates, especially at lower temperatures.

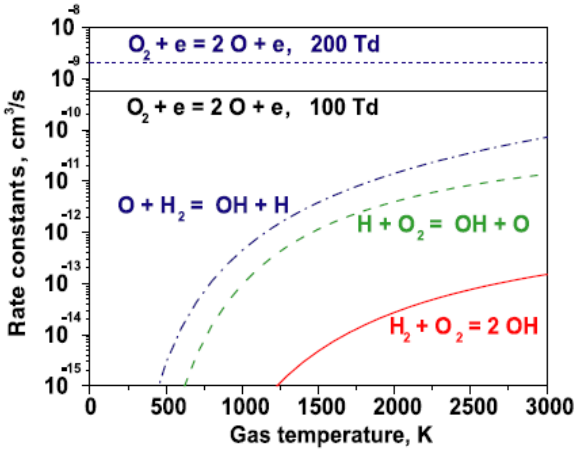

Figure 1.2 electron impact dissociation rate constants of O_2 at 100 Td and 200 Td as compared to H_2-O_2 chain branching rates [3]

1.1 Plasma Discharge Physics and Chemistry

In plasma discharges, the electrons gain energy through an external electric field, and lose via elastic and inelastic collisions with gas molecules [16]. The large difference of mass between electrons and gas species make elastic collisions inefficient, and the rate of transfer of electron energy to translational degrees of freedom of the gas is slow. On the other hand, inelastic collisions of high energy electrons with gas molecules cause rapid excitation of internal energy modes as well as dissociation and ionization. The reduced electric field, E/N (ratio of electric field to gas number density) is a critical

parameter governing the electron energy. Depending on the E/N value, the plasma physics and chemistry can be vastly different.

In a nonequilibrium discharge, the electron energy distribution function (EEDF) deviates significantly from an equilibrium Maxwellian distribution, with the mean electron temperature being several times greater than the gas temperature [16]. Several open-source codes such as BOLSIG [17] are available to calculate the EEDF by solving the Boltzmann equation. Electron impact elastic and inelastic collision cross-sections are used as input data. The nonequilibrium EEDF is approximated by a two-term expansion and assumed to be a function of only the local electric field value. Figure 1.3 shows a sample result of a BOLSIG calculation for air (79% N_2 and 21 % O_2) at 300 *K*. The fraction of input electrical power consumed in electron impact excitation and ionization is obtained as a function of E/N.

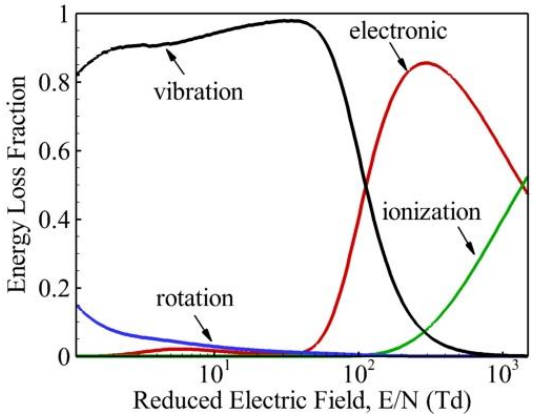

Figure 1.3 Fraction of electron energy lost in excitation of internal energy modes and ionization of O_2 and N_2 molecules in air as a function of reduced electric field, E/N.

Rotational excitation is the major channel for electron energy transfer at E/N < 1 *Td*. The excited levels rapidly relax to create a high-temperature equilibrium plasma. For E/N between 1 and 100 *Td*, electrons have sufficient kinetic energy to excite

progressively higher vibrational levels of air molecules. The average vibrational temperature can be significantly higher than the translational counterpart, with substantial nonequilibrium among the vibrational levels as well. Vibrational relaxation in air plasma is controlled primarily by the density of O atoms [18]. The relaxation time has been measured to be 20-30 *ms* after a burst of nanosecond pulse discharges in air [18]. This is much slower compared to discharge pulse duration (~50 *ns*), and time interval between the pulses (1-100 μs). Excitation of singlet states of oxygen ($O_2(a^1)$, $O_2(b^1)$) and triplet states of nitrogen ($N_2(A^3)$, $N_2(B^3)$, $N_2(C^3)$) consumes a major fraction of electron energy when E/N is in the range of 100-1000 *Td*, with a small portion used in dissociation of O_2 molecules. Ionization becomes progressively important for E/N > 500 *Td*, and dominates over all other energy modes beyond 1000 *Td*.

1.2 Literature Survey

Nonequilibrium plasma discharges (NPD) have shown great promise in thermal and kinetic enhancement of ignition and combustion at a wide range of pressures, flow velocities and equivalence ratios [5-15]. Experiments have demonstrated significant reduction in ignition delay and improved flame stabilization at low pressures and small flow residence times encountered in high-speed propulsion systems [7-9], as well as at high pressures (1 to several bar) relevant to gas turbine and IC engine applications [10-12]. A variety of NPD systems such as pulsed coronas [13], microwave discharges [14], magnetic gliding arc [15], and pulsed nanosecond volume discharges [5-7], have been studied for potential combustion applications.

Application of nanosecond duration, high-voltage (10-100 kV) pulses results in breakdown of the gas mixture, and generates high energy electrons. A number of reactive species and radicals are then produced via electron impact reactions, which can accelerate the chain reactions leading to fuel ignition, as shown in Fig. 1.4. This type of enhancement is broadly called as "plasma chemical effect". In addition, quenching of excited species and recombination of ions produce heat and increases the translational temperature of the gas mixture, which is termed as "plasma thermal effect". The key focus of research in the area of plasma assisted combustion is to understand the relative contributions of plasma chemical and thermal effects to overall combustion enhancement process.

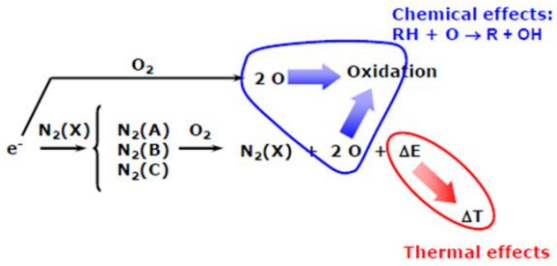

Figure 1.4. A cartoon of plasma chemical and thermal effects

Starikovskii and co-workers at the Moscow Institute of Physics and Technology were the first research group to experimentally demonstrate the advantages of using high-voltage, nanosecond plasma discharges for ignition of fuel and air mixtures [19]. The experiment consisted of coupling a shock tube with a discharge section to study plasma effect on high temperature ignition of fuel-air mixtures (above self-ignition threshold). The combustible mixture was excited by a propagating shock wave as well as by a fast ionization wave generated from the nanosecond voltage pulses. Nanosecond discharges offered two key advantages. (1) The short pulse duration (10-100 ns) greatly improved plasma stability and uniformity, since it was much shorter than characteristic timescales

for development of ionization instabilities, and glow to arc transition. (2) The high-voltage pulses created high reduced electric fields *E/N* ~ 500-1000 Td resulting in a large fraction of input energy going into vibrational and electronic excitation, and molecular dissociation. These features made it possible to generate a large number of active radical species at much higher pressures, power loadings and lower energy budgets using nanosecond pulses compared to other plasma discharge systems.

In the plasma shock tube configuration, Bozhenkov et al. [20] measured the ignition delay of H_2-O_2, H_2-air and CH_4-air mixtures diluted with Ar or He. The dependence of ignition characteristics on initial temperature, voltage amplitude and input pulse energy was studied. It was observed that the ignition delay reduction with the discharge was significant at low pressures, i.e. at higher input pulse energies. A kinetic model was developed taking into account the nonequilibrium nature of electrons, in order to calculate the density of radicals generated by the discharge and the ignition delay times. For this purpose, temporal variation of electric field was estimated from the experimental voltage and current measurements. GRI Mech 3.0 [21] was used to simulate the high temperature kinetics in the plasma afterglow. The ignition delay predictions showed good agreement with measured data although electronic excitation reactions were not taken into account in the plasma chemistry model. Kosarev et al. [22] reported the ignition of C_2H_6 - C_5H_{12}: O_2: Ar mixtures using nanosecond plasma discharges. An order of magnitude reduction in ignition delay times was observed in presence of the nonequilibrium discharge, as shown in Fig. 1.5. Kinetic calculations showed that radicals such as O, H and C_nH_{2n+1} generated by the discharge were responsible for rapid ignition. In particular, it was shown that effect of O density on the ignition delay was most

profound. The generation of radicals resulted in more rapid development of chain reactions leading to faster ignition. As pointed out by the authors, in situ quantitative measurements of radicals and active species generated by the plasma is essential for better understanding of the plasma assisted combustion process.

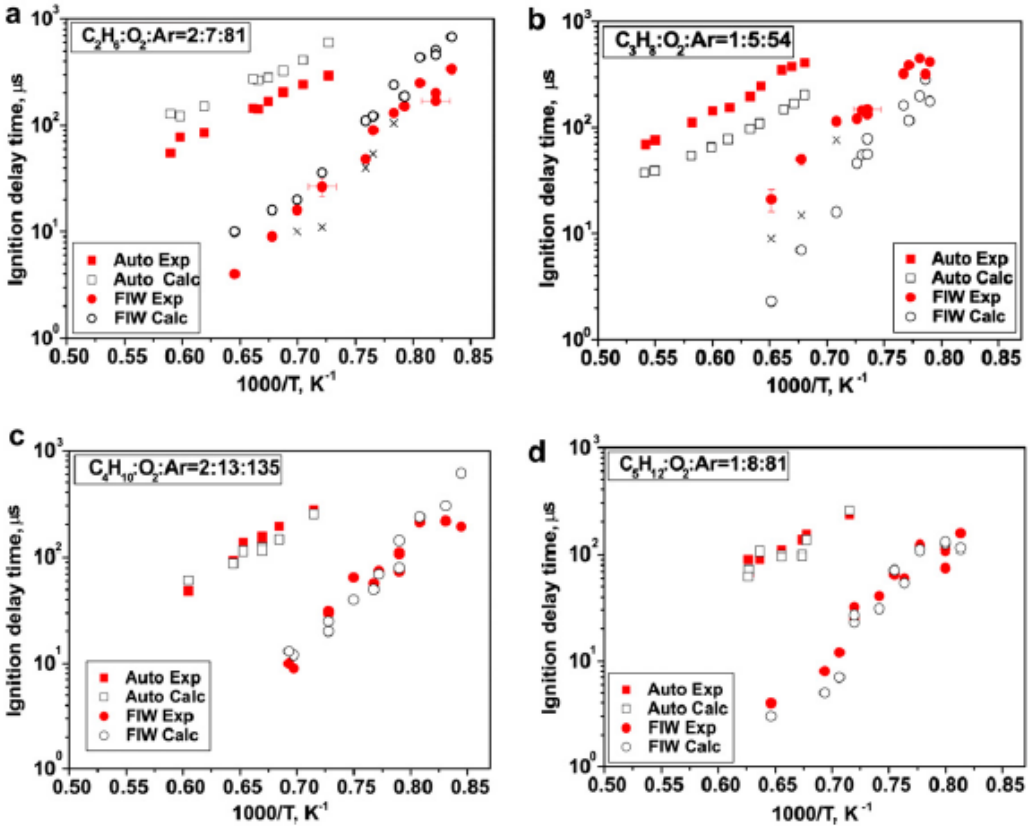

Figure 1.5: Ignition delay times with and without nanosecond plasma pulse for (a) C_2H_6:O_2:Ar, (b) C_3H_8:O_2:Ar, (c) C_4H_{10}:O_2:Ar, and (d) C_5H_{12}:O_2:Ar mixtures [22]. Closed and open symbols denote measurements and kinetic calculations respectively.

Over the past decade, researchers at Ohio State University have conducted detailed optical diagnostics of plasma generated radicals by pulsed nanosecond, plane-to-plane, dielectric barrier discharges in various fuel-air mixtures [23-28]. The primary focus has been to understand the effect of repetitive application of nanosecond voltage

pulses on ignition of fuel-air mixtures with initial temperatures below the self-ignition threshold. Lou et al. [23] demonstrated that pulsed nanosecond discharges could ignite premixed CH_4- and C_2H_4-air mixtures at low temperatures (140 - 300°C). The reacted fuel fraction measured using Fourier Transform Infrared (FTIR) absorption spectroscopy indicated that significant fuel oxidation and temperature rise even under conditions when no ignition was observed. It was inferred from the results that radical species generated by the pulsed discharges triggered a self-accelerating process of partial fuel oxidation and heat release. The plasma triggered fuel oxidation process was studied in more detail in Mintusov et al. [24]. Two sets of experiments were conducted where in C_2H_4-air and C_2H_4/N_2 mixtures were subjected to pulsed nanosecond discharges in a quartz flow reactor. It was observed that oxidized ethylene fraction was much higher (~80%) in fuel-air mixtures compared to dissociated ethylene fraction in fuel-nitrogen mixtures with plasma excitation. In addition, substantial temperature rise of upto 400 °C was detected in C_2H_4-air, as compared to only 40 °C in C_2H_4/N_2 mixtures. This demonstrated that fuel oxidation triggered by the discharge was essential for rapid heat release, fuel consumption and ultimately ignition. Kinetic modeling calculations poorly predicted several combustion species such as CH_2O, CO and CO2, highlighting the need for better validated low temperature plasma chemistry mechanisms.

Uddi et al [25] reported O atom measurements using two photon absorption laser induced fluorescence (TALIF) in air, methane-air, and ethylene-air mixtures subjected to a single nanosecond voltage pulse in a flow reactor at 60 torr. It was observed that the peak values of O atom density in air and stoichiometric methane-air plasma plasmas were nearly same, however, the decay rate was much faster in the latter case (see Fig. 1.6a). Kinetic modeling revealed that this was due to reactions of O with H and CH_3 radicals

produced by electron impact dissociation of CH_4 and quenching of excited N_2 molecules. O atom concentrations in lean ethylene-air plasmas (ϕ = 0.5) was nearly four times smaller, and the rate of decay was two orders of magnitude faster than corresponding values in air (see Fig 1.6b). This behavior was attributed to rapid reactions between ethylene and atomic oxygen at room temperature.

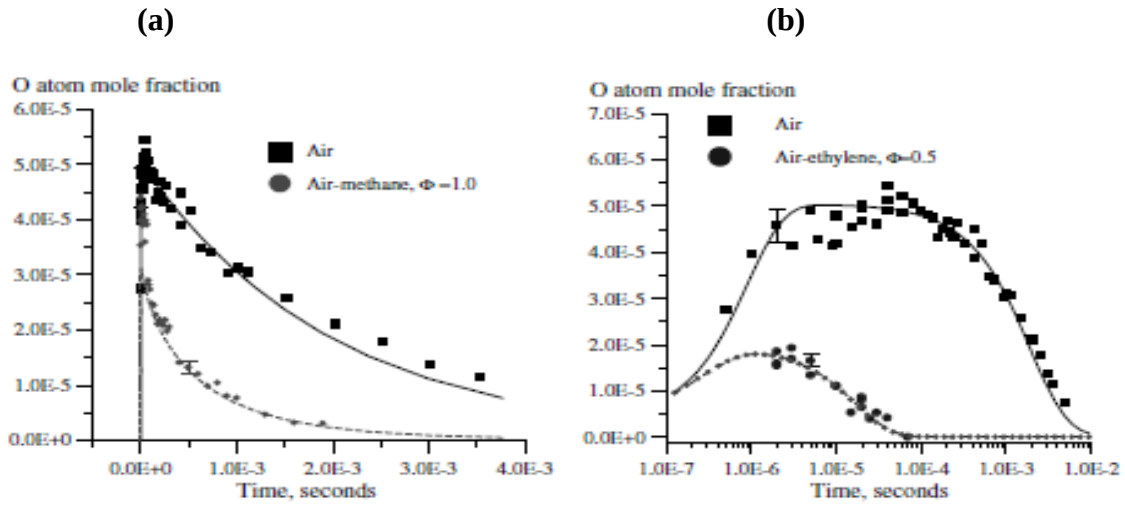

Figure 1.6. Time evolution of O atom density at the center of the discharge cell after a single nanosecond voltage pulse in (a) air and methane-air (ϕ = 1), and (b) air and ethylene-air (ϕ = 0.5) [25]

NO produced by the nonequilibrium discharges can potentially have a catalytic effect on ignition of fuel-air mixtures. For example, it was observed that trace quantities of NO had a significant effect on n-butane-air ignition [26], and was attributed to OH production via the reaction between HO_2 and NO molecules. In order to further the knowledge of plasma kinetics, Uddi et al. [27] measured NO densities in air, methane-air and ethylene-air plasmas after a single nanosecond pulse using laser induced fluorescence technique. Peak values, rise and decay rates of NO density in air and methane-air mixtures (ϕ = 0.5) were found to nearly the same. The peak NO density in ethylene-air mixture (ϕ = 0.5) was reduced by a factor of 2.5, though the rise and decay rates was similar as in air plasma. Kinetic modeling revealed that rise in NO concentration was

much faster than that predicted by the Zeldovich mechanism. It was argued that the major excited N_2 species such as $N_2(A^3)$ are quenched rapidly, and cannot explain the NO rise times from their reactions with O atoms. It was concluded that reaction of vibrationally excited N_2 species with O atoms was the most probable pathway to explain the rise trend in NO density. On the other hand, the decay in NO density was sufficiently explained by the reverse Zeldovich reaction, $NO + O \rightarrow N + O_2$, and $NO + O_3 \rightarrow NO_2 + O_2$.

Yin et al. measured the ignition delay [28] and OH concentration [29] in mildly preheated (100-200^{o}C) H_2-air mixtures subjected to nanosecond voltage waveforms in the flow reactor configuration. The number of pulses leading to ignition was found to be a weak function of mixture equivalence ratio, but showed a nonlinear dependence on pulsing frequency. At a given temperature and pressure, there existed an optimum repetition rate at which the number of pulses needed for ignition reached a minimum. Reduction in coupled pulsed energy at high repetition rates, due to increase in residual electron density, has been suggested as a possible cause for this behavior. Recent pulse energy measurements in air [30] did not show significant reduction in coupled energy at high repetition rates, suggesting a more comprehensive kinetic analysis is necessary to explain this phenomenon. In Yin et al. [28], sustained application of voltage pulses at a high repetition rate “masked" the sensitivity of ignition characteristics to the details of plasma kinetics. In order to circumvent this behavior, experiments were recently conducted in a decaying plasma in mildly preheated H_2-air mixtures [31]. The ignition characteristics were found to be highly sensitive to temperature and radical concentration at the end of a pulse burst. Ignition delay increased steeply as the number of pulses in the discharge burst was reduced. Kinetic model calculations showed that rise in temperature and H atom concentration beyond a critical threshold triggered chain reaction pathways

leading to ignition. The combination of thermal and kinetic effects resulted in a reduction of threshold ignition temperature by ~200 K as compared to thermal ignition. It should be noted that the species and temperature measurements in the plasma flow reactor experiments were conducted in the central region of the discharge volume. The heating and species production rates near the plasma boundary (sheath) layers, however, remain unknown.

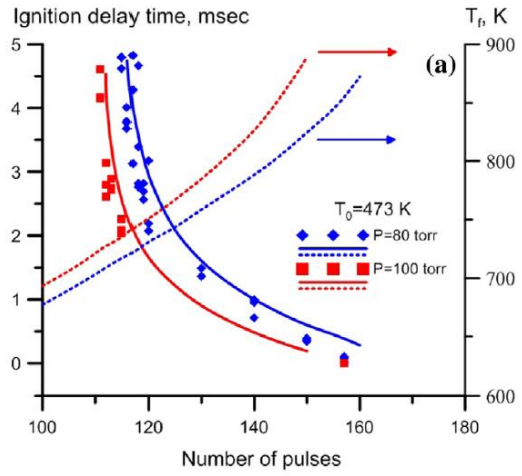

Figure 1.7. Ignition delay times as a function of number of pulses in the burst at 80 and 100 torr pressures, initial temperature of 473 K for a stoichiometric H_2-air mixture [31].

Ju and co-workers at Princeton University were the first to systematically study the effects of nonequilibrium plasma on diffusion and partially premixed laminar flames in a counterflow configuration [32-35]. Ombrello et al. [32] integrated a gliding arc discharge upstream of the oxidizer inlet to study the plasma effects on ignition of H_2-air and CH_4-air diffusion flames at 1 atm pressure. It was observed that the plasma enhancement was primarily due to NO generated from the discharge. The high pressure resulted in rapid recombination of other active species produced in the plasma zone. The effect of plasma on the flame was deduced to predominantly thermal, owing to rapid

quenching of excited species and recombination of radicals. Sun et al. [33] integrated a counterflow burner with a pulsed, nanosecond discharge system upstream of the oxidizer inlet to study the effects of O atom production of extinction of CH_4-air flames at low pressures (8 kPa). The O atom density and temperature were measured at the oxidizer duct exit using TALIF and a thermocouple respectively. At 20 kHz repetition frequency, the extinction strain rates were increased by a factor of two with plasma activation of the oxidizer flow. It was concluded that significant plasma kinetic enhancement could be achieved if the discharge temperature was above a cross-over temperature which defines the transition point from radical termination to chain branching. Sun et al. [34] developed an *in situ* nanosecond discharge coupled counterflow burner configuration using porous metal electrodes. The ignition and extinction characteristics of plasma enhanced CH_4/O_2/He flames were investigated by measuring the OH* emission at different fuel fractions, while maintaining constant oxidizer flow rates. Spatially resolved OH density and temperature measurements were also performed in the discharge/flame zone using planar laser induced fluorescence (PLIF) and Rayleigh scattering respectively. The radicals and heat generated from the discharge resulted in a monotonic, stretched ignition-extinction curve at high O_2 mole fractions as shown in Fig. 1.8. Kinetic modeling revealed that O atom generated from the discharge was crucial for controlling radical generation and promoting chain branching closer to the stagnation reaction zone.

Recently, using the *in situ* nanosecond plasma coupled counterflow configuration, Sun et al. [35] studied the ignition and extinction of Dimethyl ether/O_2/He diffusion flames at 72 torr. OH and CH_2O concentrations were measured using PLIF at constant oxidizer mole fraction and strain rates. The study focused on understanding the effect of nonequilibrium plasma on the low temperature chemistry of the DME ignition process. It

was demonstrated that plasma generated radicals accelerated the ignition process at low initial temperatures. Path flux analysis showed that atomic oxygen generated by the nanosecond discharge significantly accelerated the H abstraction from the fuel molecule, which is the rate limiting step in the decomposition of DME to form CH_2O at low temperatures. PLIF CH_2O measurements showed a marked increase in CH_2O density before the rapid temperature rise indicative of ignition, providing strong evidence for above described plasma activated low temperature chemistry process. It was also shown that addition of equivalent amount of thermal energy had negligible impact on the low temperature ignition chemistry, and radical pool generated by the nonequilibrium discharge source was the key ingredient in the plasma effect.

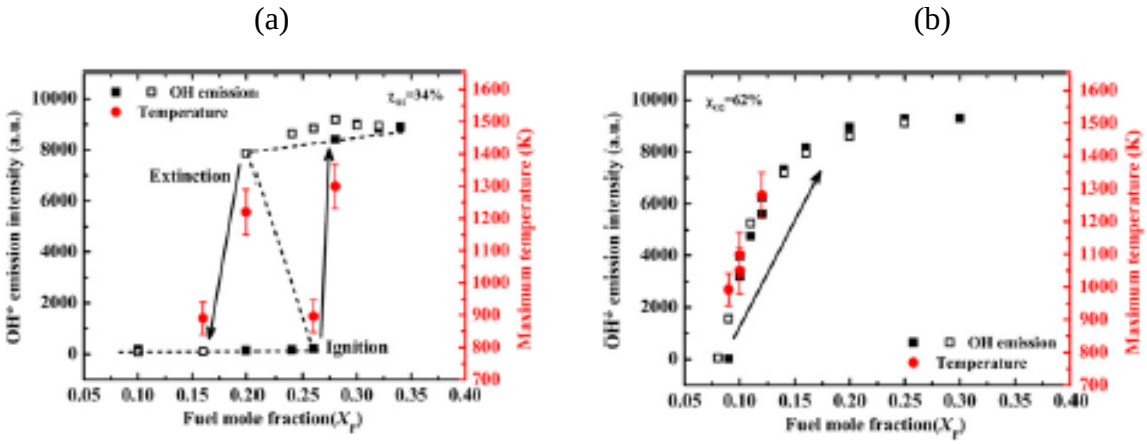

Figure 1.8: Measured OH* emission intensity and temperature in the flame zone as a function of fuel mole fraction at 9.6 kPa, 24 kHz discharge pulsing rate, and oxidizer mole fraction of (a) 0.34 and (b) 0.62. (open square symbols: decreasing X_f, closed square symbols, increasing X_f) [34].

The various research efforts described above focused on understanding the nonequilibrium plasma effects on ignition and combustion at low pressures (sub-atmospheric) and at small flow velocities (laminar flows). Under such operating environments, nanosecond discharges have been found to be uniform and devoid of

filaments [28-31, 34-35]. This allowed for spatially resolved optical diagnostics and simplified numerical modeling of the plasma chemistry processes. The ultimate goal of the above described controlled laminar experiments was to gain a fundamental understanding of plasma radical generation and chemistry processes, as well as to develop well validated plasma combustion chemistry mechanisms. However, the flow-fields in practical combustors are highly turbulent and non-uniform. Understanding plasma effects at high pressures and on turbulent flames is of great importance.

Laux and co-workers at Ecole Centrale, Paris have focused on understanding the fundamental physics and chemistry of pulsed, nanosecond discharges at atmospheric pressure and their effect on premixed jet flames [36-40]. Pilla et al. [36] demonstrated the stabilization of a lean premixed propane-air flame at atmospheric pressure using pulsed, nanosecond discharges. The discharge was created in the recirculation region downstream of a bluff-body where the flame was held. Existence of a stable flame was observed at low equivalence ratios or at high flow velocities with the plasma source, at which operating regimes blowoff occurred without plasma. The stability limits could be further stretched towards the lean side with the plasma source and a pilot flame. Pancheshyi et al. [37] studied the ignition of propane-air mixtures with pulsed, nanosecond discharges in the pressure range of 0.35-2 bar, in a pin-to-plane configuration. An inverse dependence with pressure of the minimum ignition energy was observed suggesting that the efficiency of nanosecond plasmas increase with pressure. However, the discharge onset time increased with pressure. Higher voltage pulses, or additional preionization was required to produce breakdown at higher pressures. Stancu et al. [38] performed spatially resolved optical measurements of atomic oxygen, and

excited states of nitrogen in a pin-to-pin nanosecond discharge at atmospheric pressure. O atom density was measured using TALIF, $N_2(A^3)$ density using cavity ring down spectroscopy (CRDS), $N_2(B^3)$ and $N_2(C^3)$ densities using optical emission spectroscopy (OES). Depending on the applied voltage, two discharge regimes, namely diffuse and filamentary regimes were observed as shown in Fig. 1.9. Electron impact excitation of nitrogen molecules resulted in efficient generation of excited states, which were quenched by O_2 to produce atomic oxygen. The densities of these excited states and O atoms in filamentary discharges were about one order of magnitude greater than in the diffuse regime. Pai et al. [39] studied the nature of pulsed, nanosecond discharges as a function of gas temperature, pulsing rates, and inter electrode distance. The diffuse discharge regime was only observed in a limited range of conditions, mainly a function of electrode gap width and gas temperature.

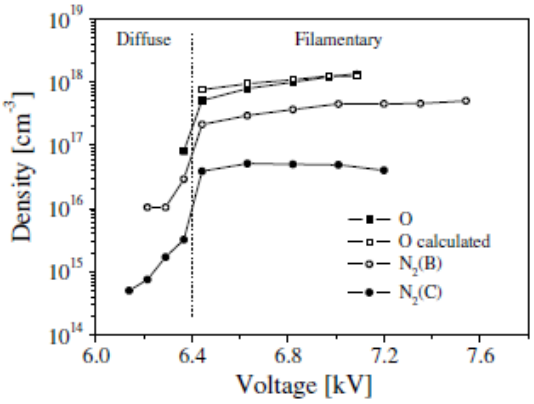

Figure 1.9: O, N2(B3) and N2(C3) measurements in diffuse and filamentary discharges as a function of applied voltage in Stancu et al. [38].

Lacoste et al. [40] studied the temporal response of weakly turbulent, bluff-body stabilized, lean premixed propane-air flame to pulsed, nanosecond discharges. The reduction in flame lift-off height induced by the plasma was inferred from CH* emission.

OH concentrations were measured using LIF in the recirculation region of the bluff-body to understand the plasma effect. It was concluded that the discharge was able to reduce the liftoff height through a combination of heating and generation of radicals. The discharge heated the mixture in the recirculation zone from 1500 K to 2000 K, and also rapidly generated excited states of N2. Quenching of these excited states produced atomic oxygen which aided in production of OH in the lower part of the recirculation zone.

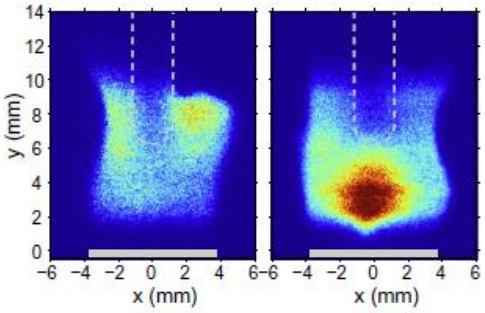

Figure 1.10: OH PLIF images without (left) and with (right) pulsed nanosecond discharges in the recirculation zone above the burner, 10 ms after starting plasma pulses at 30 kHz repetition rate [40].

In a similar work, Lacoste et al. [41] studied the effect of nanosecond discharges on the dynamics of a swirl stabilized, lean premixed methane-air flame. It was observed that the nonequilibrium plasma had a significant impact on the flame response to acoustic perturbations. For one specific case, the nanosecond discharge was demonstrated to mitigate self-sustained thermoacoustic instabilities, with and order of magnitude reduction in velocity oscillations, as shown in Fig 1.11.

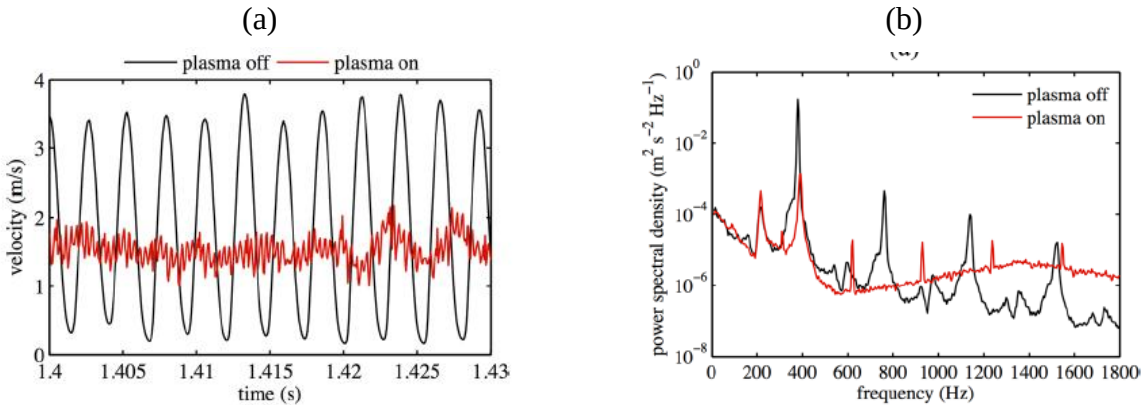

Figure 1.11. (a) Velocity fluctuations, and (b) power spectral density measured in the flame tube with and without nanosecond discharges [41].

Capelli and co-workers at Stanford University studied the pulsed, nanosecond plasma activated ignition of jet flames in subsonic and supersonic flow conditions [42-44]. Do et al. [42-43] experimentally investigated the nanosecond plasma assisted ignition and flame development for hydrogen jets injected into supersonic oxygen cross-flow. The discharge was produced via two flush mounted electrodes on a flat plate between two injectors. A combination of subsonic and sonic hydrogen jets were injected into a pure oxygen supersonic crossflow with free stream conditions ranging from M = 1.7 to 2.3. The complex flow dynamics was characterized using Schlieren imaging. PLIF and emission imaging were employed to obtain the spatial distribution of OH radicals and confirm jet flame ignition by the plasma, as shown in Fig. 1.12. A combination of experimental evidence and reduced order numerical model results was used to suggest that the jet flame ignition and stabilization occur through two steps. First, the oblique, subsonic injector seeds the hot boundary layer with fuel which is subjected to pulsed, nanosecond discharge. The discharge generated radicals trigger partial oxidation of the

fuel and create a “pilot flame”. The radicals generated by the pilot flame help in igniting the fuel coming in from the transverse, sonic injector.

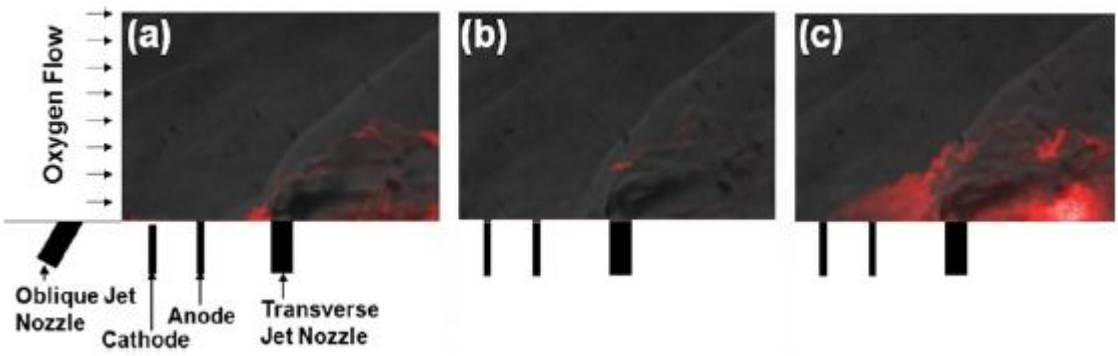

Figure 1.12. OH PLIF images overlapped with a typical Schlieren image; (a) without upstream jet, (b) both jets active, without plasma, and (c) in the presence of plasma with both jets [43].

Kim et al. [44] reported the effect of pulsed, nanosecond discharges on swirl stabilized, lean, premixed methane-air flames, shown in Fig. 1.13. The results suggested the presence of a cool pre-flame region just above the burner of temperature 500-600 K, and composed of stable intermediate species such as H_2 and CO. OH PLIF images suggested that OH concentrations in the preflame were lower than that in main flame. NO sampling measurements indicated that the discharge generated NO was consumed in the preflame region. It was found that plasma enhancement extended the blowout limit of methane-air flame by ~10%. A similar study found no discernible effect of plasma on blowout limits of hydrogen-air flames.

Cathy et al. [45] proposed a nanosecond plasma ignition device to expand the lean combustion limit in an automotive gasoline engine operating under high pressure (1400 kpa) conditions. It was found that the initial combustion period was shortened compared with conventional spark ignition while the input energy remained the same. Using a

shorter duration voltage pulse (25 ns vs 85 ns) provided greater benefits suggesting that the transient nanosecond plasma ignition mechanism is greatly influenced by the electric field strength and electron impact reaction rates in the discharge volume.

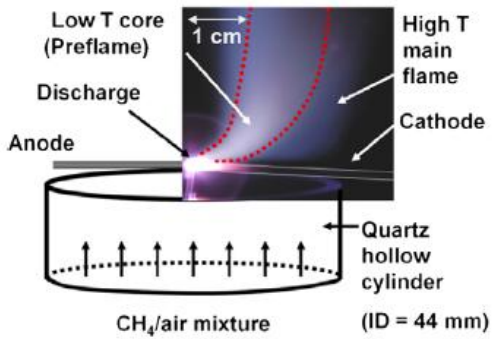

Figure 1.13. Time average image of nanosecond plasma assisted CH_4-air lean, premixed flame. Red dotted lines represent the visible boundary of the flame [44].

There have been only a few attempts in self-consistent modeling of the nonequilibrium plasma effects on ignition and combustion processes, unlike numerous experimental studies. In this context, self-consistency refers to the numerical solution of the coupled system of equations for electric potential, species continuity and flow motions, without any adjustable parameters. High fidelity NRPD simulations can be immensely beneficial in understanding the complex electric field dynamics and in quantifying the key kinetic pathways for active species production and their ensuing chemical reactions. The multi-scale nature of the problem offers enormous challenges in maintaining numerical resolution, accuracy and stability. The wide disparity in timescales between different physical phenomena is illustrated in Fig. 1.14.

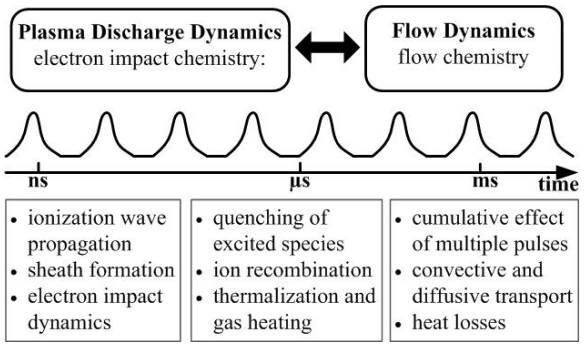

Figure 1.14. The disparity in timescales of different physical phenomena for repetitively pulsed nanosecond plasma and flow interactions.

Electron impact reactions generate ions and excited species during a high voltage nanosecond pulse. The sheath layers form near the boundaries within a few *ns* after electrical breakdown. Quenching of excited species, recombination of ions and electrons, and gas heating are observed a few μs after the voltage pulse has ended. The effects of repetitive pulsing, such as accumulation of active species become apparent over longer timescales (μs - *ms*). The numerical model should resolve both the sub-*ns* transients as well as slower processes taking place at *ms* timescales to provide useful information about the underlying physical phenomena. In addition, detailed chemistry mechanisms are essential for quantitative prediction of plasma heating rates and species production.

Macheret et al. [46] performed 1D simulations of plasma generated by a trapezoidal pulse (2 *ns* duration and 10 *kV* peak voltage) in a plane-to-plane geometry. The energy cost of ionization and electric field dynamics were analyzed using a hydrodynamic model with 3 species (positive ion, negative ion and electron). Pacheshnyi et al. [47] reported 2D simulations of cathode directed streamer discharge in a pin-to-plane geometry. Only electrons and charged species reactions were included in the

kinetics scheme, since the focus of the study was on small timescale transients (up to 100 *ns*). Unfer et al. [48] proposed a 2D model to study the interaction of flow over a flat plate with a surface barrier nanosecond discharge in air, within the context of plasma flow control. The chemical kinetics scheme consisted of only two species to reduce the computational burden. Fast gas heating and formation of compression waves were investigated using a phenomenological model for thermalization. Poggie et al. [49] carried out 1D simulations of nanosecond dielectric barrier discharges with a detailed chemical kinetics scheme consisting of 23 species and 50 reactions. The model was able to predict the generation of weak compression waves through fast gas heating from quenching of excited species. Breden et al. [50] performed 2D simulations of nanosecond streamer plasma propagation in a helium jet ejecting into quiescent air, a topic of interest in biomedical applications. Detailed chemical kinetics (16 species and 40 reactions) and photoionization effects were taken into account to provide fundamental insight into the streamer dynamics.

It must be emphasized that the high computational costs restricted above analyses [46-50] to simulate a single nanosecond voltage pulse. Tholin et al. [51] multiple nanosecond voltage pulses in air at 1 atm with a pin-to-pin configuration using a self-consistent 2D plasma model. The simulation results showed that the discharge dynamics in consecutive pulses was a weak function of the level of preionization at 300 and 1000 K. The plasma reached a “quasi-periodic” glow regime with repetitive application of voltage waveforms. The spatio-temporal evolution of electric field and electron density remained constant during each pulse. External flow aligned with the electrode axis had an impact on the ignition time of the discharge by changing the density of residual charge

density distribution in the time duration between voltage pulses. The flow field has negligible impact on the discharge dynamics as long as $U_f \times T_i << d_g$, where U_f is the flow velocity, T_i the time interval between two consecutive pulses, and d_g the gap between the electrodes.

1.3 Motivation

The effect of temperature on fuel-air ignition and combustion (thermal effects) have been widely studied and well understood. However, a comprehensive understanding of nonequilibrium plasma effects (*in situ* generation of reactive species and radicals combined with gas heating) on the combustion process is still lacking. Over the past decade, several impressive experimental investigations of plasma assisted combustion have been conducted as shown in Sec.1.2. Spatially resolved measurements of temperature and concentrations of radicals such as O, H and OH have been performed using advanced optical diagnostics. The research efforts have advanced our knowledge of electron impact kinetics and low temperature chain branching in fuel-air mixtures considerably. Nevertheless, big gaps remain in the plasma combustion chemical kinetic mechanisms of hydrocarbon fuels. The effects of nonequilibrium plasma on low temperature ignition chemistry of heavy fuels such as n-Heptane are unknown. In contrast to numerous experimental investigations, research on modeling and simulation of plasma assisted combustion has received less attention. There is a dire need for development of self-consistent numerical models for construction and validation of plasma chemistry mechanisms. A suite of numerical codes (in the lines of CHEMKIN software) capable of simulating the electric field transients, plasma kinetic and thermal

effects in homogeneous flow reactors (to study ignition), and on laminar flames (to study plasma effects on premixed/diffusion flame dynamics) would be of great benefit.

Very little is known about plasma assisted combustion in highly turbulent flow environments. Experiments investigating plasma assisted ignition and combustion in supersonic flows have relied on Schlieren imaging and qualitative diagnostics, owing to the difficulty in performing spatially resolved quantitative measurements in high speed flows. In this context, high-fidelity numerical models can be invaluable in exploring the plasma effects on ignition and combustion in turbulent and high-speed flow environments.

1.4 Research Objectives

- The primary objective of this dissertation is to establish a multi-scale modeling framework to simulate the physical and chemical effects of nonequilibrium, nanosecond plasma discharges on reacting flows. Equations for charged and neutral species, electric field and electron energy are solved. In addition, conservation equations for mass, momentum and energy are considered to simulate flow dynamics. The electron transport and reaction rate coefficients are calculated as functions of electron energy in advance using a Boltzmann equation solver, BOLSIG [17]. During the simulation, the coefficients are read from a lookup table and interpolated every timestep. The model is capable of resolving electric field transients and electron impact dynamics in sub-*ns* timescales, as well as calculating the cumulative effects of multiple discharge pulses over *ms* timescales. Detailed chemistry mechanisms are incorporated to provide deep insight into the plasma kinetic pathways.

- The modeling framework is utilized to conduct 1D simulations of plane-to-plane pulsed, nanosecond discharge dynamics in air. The calculations are validated against temperature and O atom density measurements at the center of discharge volume conducted in the OSU (Ohio State University) plasma flow reactor setup. Further, the predicted input energy coupled during the voltage pulses is compared against experimental values. The key kinetic pathways responsible for O atom generation from nanosecond discharges over multiple voltage pulses (*ns*-*ms* timescales) are quantified.
- Ignition of H_2-air mixtures subjected to pulsed nanosecond discharges is studied using 1D simulations with detailed plasma combustion kinetics. Parametric studies are performed to understand the effect of pressure (40-140 torr), initial temperature (373-573 K), pulsing frequency (10-40 kHz), equivalence ratio (0.5-1.5), and number of pulses in a burst on the ignition characteristics. The predictions are compared with experimental ignition delay measurements conducted in the OSU plasma flow reactor setup. The relative contributions of plasma thermal and kinetic effects in the ignition process are investigated.
- An effective numerical strategy is proposed to expedite the simulations of nanosecond repetitively pulsed discharges (NRPD) without compromise on the solution accuracy. The "frozen electric field" modeling approach is based on the periodic nature of NRPD, wherein the electrical characteristics reached a stationary state after a few voltage pulses. The spatial distributions and temporal evolution of the electric field, electron density and electron energy are stored in a lookup library. The subsequent pulses are simulated by freezing the electrical properties to the values

in the library. This allows for the timestep size to be increased by four orders of magnitude from 10^{-13}s to 10^{-9}s. It is found that the frozen model is 5 times faster than the complete model in simulating 50 voltage pulses, and show a speedup of upto 30 times for large scale simulations (200 - 300 pulses).

- The effect of nonequilibrium plasma on the low temperature ignition of nC_7H_{16}-air mixtures is investigated through self-consistent 1D simulations in a plane-to-plane geometry at 160 torr (0.2 atm). Special focus is provided to the effect of radicals generated by the discharge on the first stage of the nC_7H_{16}-air ignition process. A detailed path flux analysis is conducted to elucidate the low temperature chemistry. The impact of the plasma on ignition at different equivalence ratios and initial temperature are studied.
- Numerical simulations are performed to study the effect of pulsed, nanosecond discharges on a $H_2/O_2/N_2$ laminar premixed flat flame at low pressures (25 torr). Spatial distribution of OH density and temperature are compared with experimental measurements. Simulations are conducted with and without the electron based reactions to compare the plasma thermal and kinetic effects on the flame.
- The effect of nanosecond streamer discharges on ignition of two H_2 jets (upstream and downstream of the discharge region respectively) injected into supersonic O_2 cross-flow is investigated using high fidelity Large Eddy Simulations (LES). A H_2-O_2 reaction mechanism consisting of 9 species and 79 reactions including electron impact dissociation and excitation processes is utilized. The discharge development is simulated using a physics-based reduced order plasma model. Electron density and E/N (ratio of electric field magnitude and number density) are specified in the

discharge domain such that the predicted input energy matches the measurements in Do et al. [43]. The importance of the plasma generated radicals and the upstream jet on the ignition and flameholding is studied in detail.

1.5 Dissertation Outline

The dissertation is organized into 9 chapters. Chapter 2 describes the numerical framework for modeling the interactions between nonequilibrium plasma discharges and reacting flows. Simulation results of pulsed nanosecond plane-to-plane dielectric barrier discharges in air are presented in Chapter 3. Ignition of H_2-air mixtures subjected to pulsed nanosecond plane-to-plane dielectric barrier discharges is investigated in Chapter 4. A novel strategy to expedite the simulations of pulsed nanosecond discharges called the "frozen electric field approach" is described in Chapter 5. The effect of nanosecond plasma on the low temperature ignition characteristics of n-Heptane and air mixtures is presented in Chapter 6. The effect of pulsed nanosecond discharges on the dynamics of a premixed $H_2/O_2/N_2$ burner stabilized, laminar flat flame is investigated in Chapter 7. Large eddy simulation of nanosecond plasma assisted ignition and flame-holding of hydrogen jets injected into supersonic oxygen crossflow is studied in Chapter 8. Finally, the conclusions and suggestions for future work are provided in Chapter 9.

CHAPTER 2

NUMERICAL FRAMEWORK

The primary objective of the present work is to establish a multi-scale theoretical/numerical framework to study the spatio-temporal evolution of nanosecond plasma over multiple discharge pulses with detailed chemical kinetics. Equations for electric potential, electron energy, and charged and neutral species continuity are considered. In addition, the conservation equations for mass, momentum and energy of the gas mixture are solved simultaneously to model flow motions. The electron transport and reaction coefficients are expressed as functions of electron energy from solutions of point Boltzmann equation [17]. An adaptive time-step approach is utilized to take advantage of large disparity in timescales of various physical phenomena of interest. Implicit time integration is performed for stiff chemical source terms, whereas species and flow transport are treated explicitly for computational efficiency [51]. A domain decomposition approach with MPI (message passing interface) is utilized to compute the solution in parallel over multiple processors.

2.1 Governing Equations

In the present work, we use the plasma drift-diffusion fluid model with the "local electron mean energy approximation" [52]. By adopting this strategy, the conservation of electron energy is automatically enforced. The important assumptions and detailed derivation of the plasma fluid equations are provided in [53]. The continuity equation for each plasma species takes the following form,

$$\frac{\partial n_k}{\partial t} + \nabla \cdot \boldsymbol{J}_k = \omega_{\mathrm{k}} \tag{2.1}$$

where n_k (cm^{-3}) is the number density of species k, and ω_k ($cm^{-3}s^{-1}$) the production term. The species flux $\boldsymbol{J_k}$ ($cm^{-2}s^{-1}$) is obtained from the following equation,

$$\boldsymbol{J}_k = q_k \mu_k n_k \boldsymbol{E} - \nabla(D_k n_k) + n_k \boldsymbol{u} \tag{2.2}$$

where q_k is the charge number (-1 for negative ions and electrons, +1 for positive ions and 0 for neutral species), μ_k ($cm^2V^{-1}s^{-1}$) the mobility in the electric field $\boldsymbol{E}$ (Vcm^{-1}), and D_k ($cmV^{-1}s^{-1}$) the diffusion coefficient of species k. $\boldsymbol{u}$ (cms^{-1}) is the convection velocity of the gas mixture. The electron energy density n_ε ($eV\ cm^{-3}$) is obtained from the following equation,

$$\frac{\partial n_\varepsilon}{\partial t} + \nabla \cdot \boldsymbol{J}_\varepsilon = Q_\varepsilon \tag{2.3}$$

where n_ε is given by the product of electron number density, n_e, and the electron energy, ε. The flux J_ε ($eVcm^{-2}s^{-1}$) and rate of production Q_ε ($eVcm^{-3}s^{-1}$) are defined in the following equations,

$$Q_\varepsilon = -(\frac{3k_B m_e}{M}) n_e \nu_{el} (T_e - T_g) - \sum \Delta E_i r_i - \sum \boldsymbol{J_e} \cdot \boldsymbol{E} \tag{2.4}$$

$$\boldsymbol{J}_\varepsilon = -\mu_\varepsilon n_\varepsilon \boldsymbol{E} - \nabla(D_\varepsilon n_\varepsilon) + n_\varepsilon \boldsymbol{u} \tag{2.5}$$

where μ_ε ($cm^2V^{-1}s^{-1}$) is the electron energy mobility, and D_ε ($cmV^{-1}s^{-1}$) the electron energy diffusion coefficient. The first term on the right side of Eq. 5 denotes electron energy loss from elastic collisions with gas molecules, where n_e (cm^{-3}) and υ_{el} (s^{-1}) denote the number density and elastic collision frequency of electrons, respectively, m_e the electron mass (kg), M the average molecular mass of air (kg), T_e (K) the electron temperature, and T_g (K) the gas temperature. The second and third terms represent energy loss from electron impact excitation and ionization reactions, and energy gain from acceleration in the

applied field, respectively. ΔE_i (eV) is the heat of *ith* reaction with reaction rate r_i ($cm^{-3}s^{-1}$), and $\boldsymbol{J_e}$ the electron density flux ($cm^{-2}s^{-1}$).

The electric potential φ (V) is computed using the Poisson equation below, with the electric field, $\boldsymbol{E}$ obtained from Eq. 7,

$$\nabla.(\varepsilon\nabla\varphi) = -e(n_+ - n_- - n_e) \tag{2.6}$$

$$\boldsymbol{E} = -\nabla\varphi \tag{2.7}$$

where n_+ and n_- are the sum of number densities of positive ions and negative ions respectively. The plasma fluid equations described previously are coupled with the following conservation equations of mass, momentum and energy.

$$\frac{\partial\rho}{\partial t} + \frac{\partial\rho u_i}{\partial x_i} = 0 \tag{2.8}$$

$$\frac{\partial\rho u_i}{\partial t} + \frac{\partial(\rho u_i u_j)}{\partial x_j} = -\frac{\partial p}{\partial x_i} + \frac{\partial\tau_{ij}}{\partial x_j} + F_i^{EHD} \tag{2.9}$$

$$\frac{\partial\rho E}{\partial t} + \frac{\partial[(\rho E + p)u_i]}{\partial x_i} = -\frac{\partial q_i}{\partial x_i} + \frac{\partial(u_i\tau_{ij})}{\partial x_j} + Q^{JH} \tag{2.10}$$

where ρ ($kgcm^{-3}$) is the density of the plasma mixture, p ($kgcm^{-1}s^{-1}$) the pressure, and u_i and u_j the flow velocity components in *ith* and *jth* directions, respectively. τ ($kgcm^{-1}s^{-2}$) is the viscous shear stress tensor, q_j the energy flux from heat conduction and diffusion, F_i^{EHD} the electro- hydrodynamic force per unit volume, and Q^{JH} the heat release rate from Joule heating given by Eqs. 11, 12, 13 and 14 respectively.

$$\tau_{ij} = \kappa(\partial u_i/\partial x_j + \partial u_j/\partial x_i) \tag{2.11}$$

$$q_j = -\lambda(\partial T/\partial x_j) + \rho\sum_k h_k Y_k D_k(\partial Y_k/\partial x_j) \tag{2.12}$$

$$F_i^{EHD} = eE_i(n_+ - n_- - n_e) \tag{2.13}$$

$$Q^{JH} = e\boldsymbol{E}.\sum(\boldsymbol{J}_+ - \boldsymbol{J}_- - \boldsymbol{J}_e) \tag{2.14}$$

where κ ($kgcm^{-1}s^{-1}$) is the dynamic viscosity, λ ($Wcm^{-1}K^{-1}$) the thermal conductivity of the gas mixture, and D_k the effective diffusion coefficient for species *k* obtained using Wilke's mixing rule [8]. The total energy per unit volume ρE (Jcm^{-3}) is given by the following equation,

$$\rho E = \rho h - p + \rho(u_j u_j / 2) \tag{2.15}$$

where *h* (Jkg^{-1}) is the mixture enthalpy per unit mass obtained from Eq. 16,

$$h = \sum_k Y_k \{h_k^0(T_{ref}) + \int_{T_{ref}}^{T} C_{p,k}(T')dT'\} \tag{2.16}$$

where h_k^0 and $C_{p,k}$ are the enthalpy of formation at a reference temperature T_{ref}, and the specific heat at constant pressure of species *k*, respectively.

2.2 Physical Configurations

2.2.1 Plane-to-Plane Discharge

The plane-to-plane dielectric barrier discharge configuration is shown in Fig. 2.1. It is used to study the ignition of fuel-air mixtures subjected to pulsed nanosecond discharges at low pressures (40-160 torr). Two copper electrodes covered with a thin layer (1.75 *mm* thickness) of quartz as dielectric are placed 1*cm* apart with the gap filled with synthetic air (79% N_2 and 21% O_2 by mole fraction) or pure N_2 (for comparison with analytical model results). A high voltage pulse generator is connected to the right electrode in Fig. 4(a), whereas the left electrode is grounded at all times.

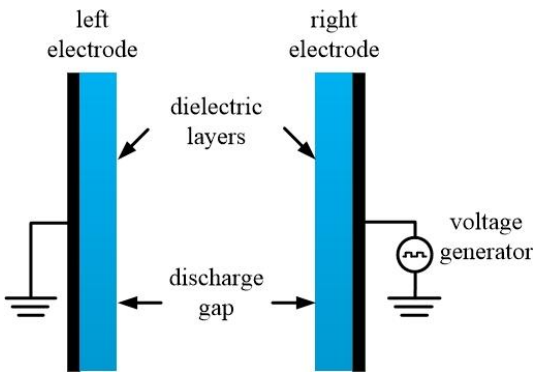

Figure 2.1 Schematic of simulation configuration for plane-to-plane dielectric barrier discharge.

2.2.1.1 Boundary Conditions

At solid walls, a zero flux boundary condition is imposed for neutral species, with electron, positive ion and negative ion fluxes given by Eqs. 17, 18 and 19 respectively

$$\boldsymbol{J}_{e,s}\cdot\boldsymbol{n}_s = \frac{1}{4}n_e\left(\frac{8k_bT_e}{\pi m_e}\right)^{\frac{1}{2}} - a\sum_k \gamma \boldsymbol{J}_{+k,s}\cdot\boldsymbol{n}_s + (a-1)\mu_e n_e \boldsymbol{E}\cdot\boldsymbol{n}_s \tag{2.17}$$

$$\boldsymbol{J}_{+,s}\cdot\boldsymbol{n}_s = \frac{1}{4}n_+\left(\frac{8k_bT_g}{\pi m_+}\right)^{\frac{1}{2}} + a\mu_+ n_+ \boldsymbol{E}\cdot\boldsymbol{n}_s \tag{2.18}$$

$$\boldsymbol{J}_{-,s}\cdot\boldsymbol{n}_s = \frac{1}{4}n_-\left(\frac{8k_bT_g}{\pi m_-}\right)^{\frac{1}{2}} + (a-1)\mu_- n_- \boldsymbol{E}\cdot\boldsymbol{n}_s \tag{2.19}$$

where $\boldsymbol{J}_{e,s}$, $\boldsymbol{J}_{+,s}$, $\boldsymbol{J}_{-,s}$ are the electron, positive ion and negative ion fluxes at the boundary, is $\boldsymbol{n}_s$ the normal vector pointing outwards, and γ the secondary electron emission coefficient for ionic species colliding with the surface. a = 1 if $\boldsymbol{E}\cdot\boldsymbol{n}_s$ < 0, and a = 0 otherwise [54]. The electron energy flux at the solid boundary is given by the following equation,

$$\boldsymbol{J}_{\varepsilon,s}\cdot\boldsymbol{n}_s = \left(\frac{5}{2}k_bT_e\right)\left[\frac{1}{4}n_e\left(\frac{8k_bT_e}{\pi m_e}\right)^{\frac{1}{2}} + (a-1)\mu_e n_e \boldsymbol{E}\cdot\boldsymbol{n}_s\right] - a\left(\frac{5}{2}k_bT_{se}\right)\sum_k \gamma \boldsymbol{J}_{+k,s}\cdot\boldsymbol{n}_s \tag{2.20}$$

where $\boldsymbol{J}_{\varepsilon,s}$ is the electron energy flux at the wall, and T_{se} the temperature of secondary electrons ejected from the surface.

A zero flux condition is used for mass and momentum conservation equations at solid boundaries. Treatment of the wall boundary condition for the gas energy equation (Eq. 10) needs special care. Rapid heating occurs in the cathode layer during each nanosecond voltage pulse, due to the ion Joule effect. Subsequent heat loss to the solid surface takes place over a much longer timescale. Because of the low thermal diffusivity of quartz ($\alpha \sim 1.4\text{x}10^{-6}\ m^2s^{-1}$), only a small portion of the dielectric layer can be assumed to be affected by the heat transfer from the gas. We make use of analytic self-similar solutions for transient temperature distributions in a semi-infinite solid with constant heat flux [55] to arrive at the following expression for boundary temperature,

$$\mathrm{T_b} = \frac{T_{amb} + G(t) * T_{gw}}{1 + G(t)}; G(t) = \frac{4k_{gw}\sqrt{(\alpha_d t/\pi)}}{k_d \Delta x} \tag{2.21}$$

where $\mathrm{T_b}$, T_{amb}, and T_{gw} are the boundary temperature, external ambient temperature and gas temperature at a distance Δx from the wall, respectively. $G(t)$ is a non-dimensional heat transfer parameter, k_d the thermal conductivity of quartz (1.3 $Wm^{-1}K^{-1}$), and k_{gw} the thermal conductivity of the gas mixture ($Wm^{-1}K^{-1}$) at temperature T_{gw}. $G(t)$ is negligibly small (less than 0.1) until about 2 *ms*, which indicates that the boundary is, in reality, closer to isothermal than adiabatic conditions.

The Poisson equation is solved only in the gas, assuming zero potential at the left boundary, and the gap voltage V_{gap} at right boundary. V_{gap} is obtained from the applied voltage V_{app} using equation below [45],

$$\frac{dV_{app}}{dt} = (1 + \frac{2l_d}{\varepsilon_d L})\frac{dV_{gap}}{dt} - \frac{2l_d e}{\varepsilon_d \varepsilon_0 L}\int_0^L [J_+ - J_-]dx \qquad (2.22)$$

where L (cm) is the gap length, l_d (cm) the thickness of the dielectric layer, ε_d the dielectric constant (4.8 for quartz), and J_+ and J_- the net positive and negative charge fluxes, respectively.

2.2.2 Plasma enhanced premixed flame

Figure 2.2 shows the plasma enhanced premixed flat flame configuration, which consists of encapsulating the "entire" combustion process (preheating, high-temperature reaction zone, and products) within the plasma discharge. The burner surface acts as the ground electrode, and the high-voltage electrode is a 12-cm-diameter Tungsten mesh (open area = 90%) located 40 mm above the burner surface, which is supported by four ceramic posts mounted to the outer portion of the McKenna burner. This location of the high-voltage electrode results in direct coupling of the plasma processes to the combustion chemistry of interest, while providing minimal disturbance to the laminar flow field.

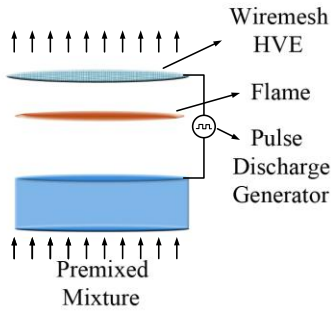

Figure 2.2 Schematic of simulation configuration for plasma enhanced premixed flame.

2.2.2.1 Boundary Conditions

Temperature, velocity, and species mole fractions are specified at the inlet. Vanishing gradient boundary condition is applied for the energy equation, whereas species mole fractions are extrapolated at the outlet. Charged species fluxes include a drift component (due to electric field), and electron flux at the cathode boundary has contribution from secondary emission.

2.3 Nanosecond Voltage Waveforms

The voltage waveforms used in the plasma assisted ignition studies is shown in Fig 2.3. The CPT pulse consists of a bipolar negative-positive waveform with voltage peaks at -22.5 *kV* and +20 *kV* respectively. The total pulse duration is 100 *ns* with 12 *ns* FWHM each cycle. On the other hand, the FID waveform is 120 ns long, and is approximated by three Gaussian waves of peak voltages 27.5 kV, -20 kV and 13.5 kV respectively.

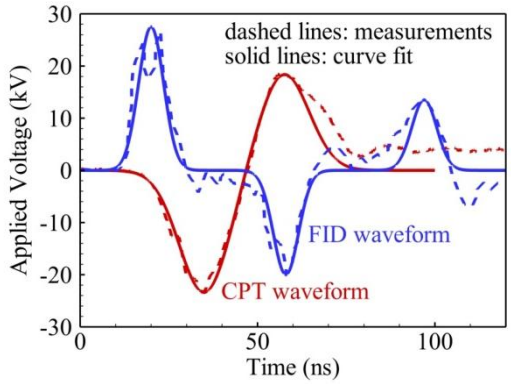

Figure 2.3 Experimental waveforms and corresponding curve-fits used in model calculations.

2.4 Plasma Combustion Chemistry

The plasma combustion chemistry mechanism consists of electrons, ions, excited and neutral species. The reaction set includes electron impact dissociation, ionization,

excitation and attachment, along with quenching processes of excited states. In addition, the conventional combustion kinetics pathways such as radical initiation, branching, oxidation and recombination are incorporated in the chemistry dataset.

The uncertainty in electron impact rate constants is about +/-30%, and mainly depends on the accuracy of collision cross-section calculations and measurements [56]. For bi-molecular and tri-molecular reactions, the error limits depend inversely on the magnitude of rate constants [57], and can be as high as 100% for slower reactions. In addition, most of the rate measurements are performed at room temperature (300 *K*); this may be an additional source of error for temperature sensitive reactions. We have performed the simulations within the limitations of available kinetics data. Recent CARS measurements in air [58] demonstrate that vibrational energy per molecule for the first ~100 pulses increases linearly with pulse number, and vibrational temperature levels off at ~1250 *K*. At 40-100 *torr* pressure and 300-600 *K* temperature, the vibrational relaxation takes 20-30 ms [4]. Hence, vibrationally excited species are not explicitly included in the kinetics mechanism. The energy coupled to the plasma when E/N is below 100 Td is assumed to be "locked" in the N_2 molecules and not considered as a source of gas heating.

2.4.1 Air (N_2/O_2) discharge kinetics

The chemical kinetic model of the air plasma used in the present work consists of 20 species and 176 reactions. It is derived through a sensitivity study from a larger chemistry mechanism described in [27]. The model incorporates the neutral species N, N_2, O, O_2, O_3, and NO; charged species e^-, N_2^+, N_4^+, O_2^+, O_4^+, and O_2^-; and excited species $N_2(A^3\Sigma)$, $N_2(B^3\Pi)$, $N_2(C^3\Pi)$, $N_2(a'^1\Sigma)$, $O_2(a^1\Delta)$, $O_2(b^1\Sigma)$, $N(^2D)$, and $O(^1D)$.

Atomic oxygen is the dominant species in air plasma generated by electron impact dissociation of oxygen during voltage pulses and via excited nitrogen quenching by oxygen during afterglow. Other important neutral species include excited electronic states of nitrogen $A^3\Sigma$, $B^3\Pi$, $C^3\Pi$, and $a'^1\Sigma$, as well as ozone.

2.4.2 $H_2/N_2/O_2$ plasma ignition kinetics

A detailed mechanism consisting of 35 species and 248 reactions was compiled by combining plasma air chemistry data with traditional H_2-O_2 ignition kinetics and hydrogen plasma reactions [27,59-60]. A reduced chemistry model was deduced through sensitivity analysis and consists of 19 species and 112 reactions. The reduced mechanism incorporates the neutral species N_2, H_2, O_2, H, O, O_3, OH, HO_2, and H_2O; charged species N_2^+, HN_2^+, H_3O^+, O_2^-, and e^-; and excited species $N_2(A^3)$, $N_2(B^3)$, $N_2(C^3)$, $N_2(a^1)$ and $O(^1D)$.

2.4.3 $H_2/N_2/O_2$ plasma flame kinetics

A detailed kinetics mechanism consisting of 42 species and 310 reactions was compiled by combining $H_2/O_2/N_2$ plasma chemistry data [27,59] with conventional H_2-O_2 combustion kinetics [60] and NO_x kinetics [61-63]. The mechanism incorporates charged species O^+, N_2^+, O_2^+, N_4^+, O_4^+, H_2^+, H_3^+, HN_2^+, HO_2^+, H_2O^+, H_3O^+, O^-, O_2^-, and e^-, excited species $N_2(A^3\Sigma)$, $N_2(B^3\Pi)$, $N_2(C^3\Pi)$, $N_2(a'^1\Sigma)$, $N(^2D)$, $O_2(a^1\Delta)$, $O_2(b^1\Sigma)$, $O_2(c^1\Sigma)$, and $O(^1D)$; neutral species N_2, H_2, O_2, H, O, N, O_3, OH, HO_2, H_2O_2, H_2O, NO, NO_2, NH, NNH, NH_2, NH_3, N_2O and HNO. The plasma chemistry processes pertaining to H_2O (ionization, dissociation etc.) have also been included since they are important in accurately predicting the discharge development downstream of the flame.

2.4.4 $nC_7H_{16}/N_2/O_2$ plasma ignition kinetics

In order to understand the effect of radicals generated by the pulsed discharge process on the low and high temperature chemical pathways in the nC_7H_{16} ignition process, an optimized kinetic model is developed. The model combines a reduced nC_7H_{16} chemical kinetic model [64-65], fuel and air plasma reactions [27, 59-60] and NO_x reactions [61-63].The kinetic model consists 166 species and 611 reactions, incorporating charged species N_2^+, O_2^+, HN_2^+, H_3O^+, $C_7H_{15}^+$, $C_6H_{13}^+$, $C_5H_{11}^+$, O_2^-, and e^-; excited species $N_2(A^3)$, $N_2(B^3)$, $N_2(C^3)$, $N_2(a^1)$, $O(^1D)$ and neutral species. Electron impact processes (ionization, dissociation, excitation and attachment) along with quenching, detachment and recombination reactions are considered. Self-consistent sets of electron impact cross-sections were used for O_2 [66] and N_2 [67]. However, there are no cross-section data available for nC_7H_{16}, so it is assumed that the cross-sections for nC_7H_{16} are similar to that of C_2H_6 taken from [67]. NO_x kinetics (from GRI Mech 3.0 [61]) is included in the kinetic model to study the catalytic effect of NO on ignition.

2.5 Heat and Mass Transport

2.5.1 Electron and Electron Energy Mobility and Diffusion Coefficients

The electron transport and reaction rate coefficients are expressed as functions of electron energy using BOLSIG [17], and updated at every time-step through interpolation. The general format of the interpolation function is given by the following equation,

$$f_i = \exp(a_i + b_i \log(\varepsilon) + \frac{c_i}{\varepsilon} + \frac{d_i}{\varepsilon^2} + \frac{e_i}{\varepsilon^3}) \tag{2.23}$$

where f is the electron transport or reaction rate parameter, ε the electron energy (eV units), a_i - e_i are the curve-fit coefficients obtained from BOLSIG solutions. The validity

of the two-term approximation used in BOLSIG to compute the solution of the local electron Boltzman equation is verified in Fig 2.4, which compares measurements of the Townsend ionization coefficient [68] in N_2 plasma with predictions as a function of E/N.

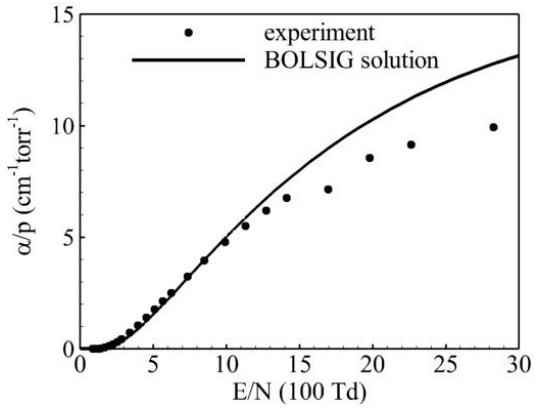

Figure 2.4 Comparison between Townsend ionization coefficients predicted by BOLSIG [3] and experiments [24] in nitrogen as a function of reduced electric field.

The estimated ionization rate is in excellent agreement with measurements up to 1000 *Td*, and about 20% higher at 1500 *Td*. In general, the reduced electric field is greater than 1000 Td only in the interior of cathode sheath region (~0.2 mm thickness at 60 torr and 300 K). The ionization rates in the cathode sheath, however, are negligible since it is essentially free of electrons. It has been shown that runaway ionization processes are dominant only in very short gaps and low pressures even at extremely high electric fields [70-71]. Hence for our purpose, the electron impact transport and reaction coefficients provided by BOLSIG are sufficiently accurate.

2.5.2 Ion Mobility and Diffusion Coefficients

Electrical mobility refers to the convection of charged particles (electrons and ions) in the direction of applied electric field. In the present work, the mobility of ions is

obtained (or estimated using data for similar species) from [71-72]. The ion diffusion coefficients are calculated from the mobility data using the Einstein relation given in the following equation,

$$D_i = (\frac{k_B T_i}{e})\mu_i \tag{2.24}$$

where D_i is the ion diffusion coefficient, μ_i the mobility, and T_i the ion temperature (assumed to be same as gas temperature).

2.5.3 Mixture Averaged Diffusion Coefficients, Thermal Conductivity and Viscosity

The subroutines available in the CHEMKIN-III transport package [73] are used to calculate the mixture averaged diffusion coefficients, thermal conductivity and viscosity. The transport data is supplied in CHEMKIN format for all the species. The transport parameters of electronically excited species and ions were assumed to be identical to the corresponding values of the ground state molecule.

2.6 Numerical Methods

The governing equations can be cast in the following vector notation,

$$\frac{\partial U}{\partial t} + \nabla.F - \nabla.\mathrm{G} = S \tag{2.25}$$

In 1D case, the vector quantities in Eqn. 19 are given by,

$$\begin{aligned} U &= [\rho u \quad \rho E \quad \rho Y_1 \quad \ldots \quad \rho Y_N]^T \\ F &= [\rho u^2 + P \quad (\rho E + P)u \quad (q_1 \mu_1 E + u)\rho \mathrm{Y}_1 \quad \ldots \quad (q_N \mu_N E + u)\rho \mathrm{Y}_N]^T \\ G &= [\frac{2\upsilon}{3}\frac{\partial u}{\partial x} \quad -\lambda \frac{\partial T}{\partial x} + \sum_k \rho h_k Y_k D_k \frac{\partial Y_k}{\partial x} \quad \rho Y_1 D_1 \frac{\partial Y_1}{\partial x} \quad \ldots \quad \rho Y_N D_N \frac{\partial Y_N}{\partial x}]^T \\ S &= [F_{EHD} \quad Q_{JH} \quad \dot{\omega}_1 \quad \ldots \quad \dot{\omega}_N] \end{aligned} \tag{2.26}$$

The above formulation does not include the equations for electron continuity, electron energy and electric potential, which are solved separately. Note that the mass

conservation is not solved in the present formulation, and density at each grid location is calculated as the sum of the species densities.

A fractional timestep approach [51] is used to treat the convection-diffusion term and the chemical source term separately in the species equations. The spatial discretization of species and conservation equations are performed using an exponential Scharfetter-Gummel scheme [74]. Implicit time integration of electron continuity and energy equations is performed using a Generalized Minimal residual (GMRES)-based ODE solver [75]. The chemical source term in species equations is treated implicitly using a dense matrix solver [75]. Explicit time integration of species and flow conservation equations ion is performed with a fourth-order Runge-Kutta method. A uniform grid consisting of 1000 node points was found necessary to obtain a grid convergent solution. The solution is computed in parallel over multiple processors with domain decomposition using MPI. The strong coupling between electron density (solved in Eq. 1) and electric potential (in Eq. 6) results in a severe time-step restriction [76]. In order to overcome this constraint, the following semi-implicit form of the Poisson equation [76] is solved for electric potential,

$$\nabla.(\varepsilon + \frac{e}{\varepsilon_0}\mu_e n_e \Delta t)\nabla\varphi = -\frac{e}{\varepsilon_0}(n_+ - n_- - n_e + \Delta t(\nabla.D_e\nabla n_e + S_e)) \qquad (2.27)$$

Specifically, the electron density, n_e at (k+1)th timestep on the right hand side of Eq. 6, is estimated by making use of the continuity equation for electrons (Eq. 1). The above modifications to the Poisson equation have negligible effects on the accuracy of the results.

An adaptive time-step approach [48] is adopted, taking advantage of the large disparity in the timescales of the dominant physical processes. The numerical time step is fixed at 1 *ps* during the voltage pulses. The electron energy equation and semi-implicit version of the Poisson equation are solved only during voltage pulses, since electric-field effects become negligible and the space charge density rapidly decays as the applied voltage goes to zero. Beyond this juncture, the electric field and space charge are set to zero, and the time step is raised to 1 *ns*. The time step is reset to 1*ps* at the beginning of the next voltage pulse, and the process is repeated. By adopting this strategy, we are able to simulate a variety of physical phenomena occurring at different time scales (1 *ps*-10 *ms*) over multiple discharge pulses.

CHAPTER 3

PULSED NANOSECOND PLASMA DISCHARGES IN AIR IN A PLANE-TO-PLANE GEOMETRY

In this chapter, we make use of the nonequilibrium plasma modeling framework described previously to understand the dynamics of pulsed nanosecond dielectric barrier discharges (NS DBD) in a plane-to-plane geometry. One dimensional simulations are conducted in the pressure and pulsing frequency range of 40-100 *torr* and 1-10^5 *Hz*, respectively. The uniform and diffuse nature of the discharge in ICCD images [28-30] justifies the 1D assumption. The present work simulates the operating conditions and physical parameters such as voltage pulse shape and duration described in Yin et al. [28]. The model predictions are validated against results of a quasi-1D analytical model [77] as well as experimental measurements [25-26, 30]. The underlying mechanisms and key chemical pathways governing plasma gas heating and radical species production are investigated in detail. Implications of current results on applications such as plasma assisted ignition are discussed.

3.1 Physical Configuration

The physical configuration of concern is shown in Fig. 3.1(a). In all the cases considered in this study, the discharge geometry and operating conditions closely match the NS DBD flow reactor experiment in [25]. Two copper electrodes covered with a thin layer (1.75 *mm* thickness) of quartz as dielectric are placed 1*cm* apart with the gap filled with synthetic air (79% N_2 and 21% O_2 by mole fraction) or pure N_2 (for comparison

with analytical model results). A high voltage pulse generator is connected to the right electrode in Fig. 3.1(a), whereas the left electrode is grounded at all times. The voltage pulse considered in this study is a Gaussian fit to the experimental CPT waveform [25] as shown in Fig. 3.2(b). The CPT pulse consists of a bipolar negative-positive waveform with voltage peaks at -22.5 *kV* and +20 *kV* respectively. The total pulse duration is 100 *ns* with 12 *ns* FWHM each cycle.

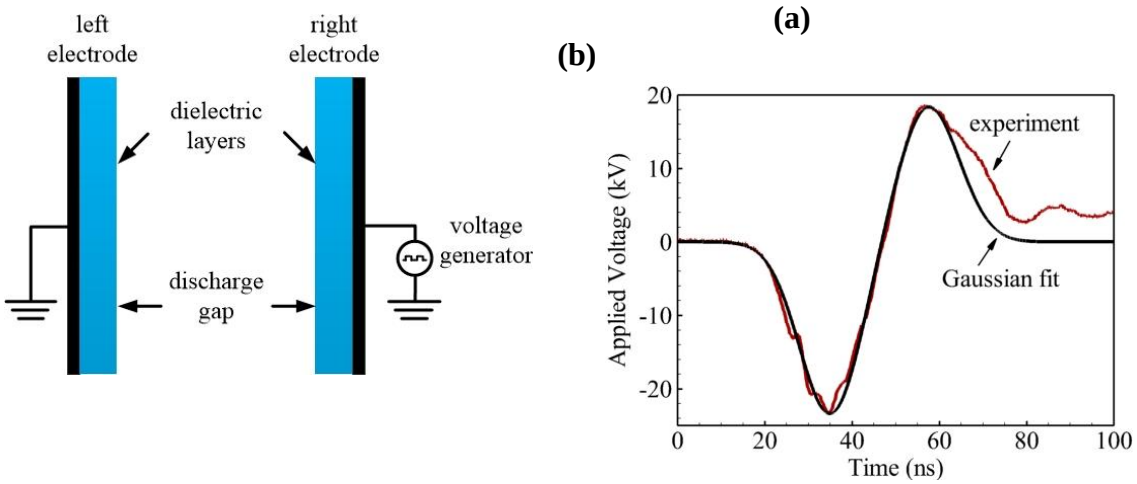

Figure 3.1. (a) Schematic of simulation configuration. (b) Gaussian fit to CPT experimental waveform [21] used in current work. The applied voltage shown is representative of a single discharge pulse. The same waveform is applied in repetitive fashion at a prescribed frequency in the pulsed NS DBD simulations.

3.2 Results and Discussion

In this section, we describe the physiochemical nature of pulsed NS DBD with the help of one-dimensional simulations, which are validated against experimental data and analytical model calculations. All simulations are performed assuming a constant initial electron density in the computational domain. Due to the repetitive nature of the discharge process, the residual electrons from one pulse are responsible for initiation of

discharge during subsequent pulses. Figure 3.2 shows that the nanosecond discharge is not sensitive to variation in initial electron densities. The electron number density in the quasi-neutral plasma (x = 0.5 *cm*) after breakdown differs by less than 5% when the initial electron density is increased by three orders of magnitude (10^7-10^{10} cm^{-3}). In the presence of residual electrons, photo-ionization does not play an important role in initiating the discharge, and hence is not considered as a source term in the electron and positive ion continuity equations.

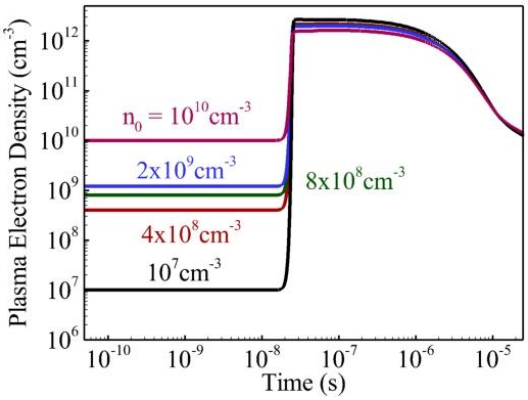

Figure 3.2 Sensitivity of evolution of electron number density in plasma (x = 0.5 *cm* location) for changes in initial electron density.

3.2.1 Comparison with Analytical Model

Adamovich et al. [77] developed a quasi-one-dimensional model to describe the energy coupling in the plasma based on experimental evidence of uniformity of NS DBD. The model demonstrates that the input energy is primarily a function of breakdown voltage and capacitance of dielectric layers, as given by the following relation,

$$Q_{pulse} \approx \frac{1}{2} C \left[V_b^{\,2} + V_{peak}^2 \frac{\sqrt{2\pi}}{(\tau / RC)} \right] = \frac{1}{2} \frac{\varepsilon_d \varepsilon_0 A}{2 l_d} \left[V_b^{\,2} + V_{peak}^2 \frac{\sqrt{2\pi}}{(\tau / RC)} \right] \qquad (3.1)$$

where Q_{pulse} is the input pulse energy, C the effective capacitance of dielectric layers on electrodes, V_b and V_{peak} breakdown voltage and peak voltage, respectively, R the resistance of shielded plasma after breakdown, τ the pulse duration parameter in Gaussian fit of voltage waveform, ε_d and l_d the dielectric constant and dielectric thickness, respectively, and A the electrode surface area. Similar analytic expressions have been obtained for electric field and electron density in plasma, cathode sheath location and electric field at sheath edge, and input power during the voltage pulse.

Figure 3.3 shows a comparison between analytical results and the present 1D model calculations. The simulation is performed in pure N_2 at 300 *K* and 60 *torr* initial temperature and pressure respectively using only nitrogen-based species from the plasma air chemistry mechanism described previously in chapter 2. The voltage waveform is a positive-negative bipolar pulse with voltage peaks at 23.5 *kV* and -17.5 *kV* respectively, FWHM 10 *ns* for each cycle, and pulse duration of 200 *ns*. Good agreement with analytical calculations provides confidence in the 1D model predictions. It is evident in Fig. 3.3(a) that breakdown in the discharge gap occurs at approximately 10 *kV*, and the electric field in the plasma drops rapidly, due to positive and negative space charge accumulation at the cathode and anode sheath boundaries. The coupled power and energy shown in Fig. 3.3(b) are calculated using the following relations for the present model,

$$W_p = A\left|\int_0^L e\boldsymbol{E}.(\boldsymbol{J}_+ - \boldsymbol{J}_- - \boldsymbol{J}_{\boldsymbol{e}})dx\right|; Q_p = \int_0^{T_p} W_p dt \tag{3.2}$$

where W_p and Q_p are coupled power (*W*) and coupled energy (*J*) respectively, and T_p is the pulse duration. Approximately 60% of the pulse energy is input during the breakdown process. The remaining energy is coupled when the field in the plasma reverses in

direction. Similar behavior is observed for discharges in air as described in the next section. Fig. 3.3(c) depicts the location of the cathode sheath boundary and electric field at that location during breakdown. The quasi-steady sheath is located at ~0.2 *mm*, as predicted by the model. The electric field in the sheath reaches 140 *kV/cm* when the sheath attains its quasi-steady location. The deviations in the sheath field predicted by the present 1D analysis and the analytical model can be attributed to differences in electron impact ionization rates obtained from BOLSIG and experimental curve-fits employed in the analytical model.

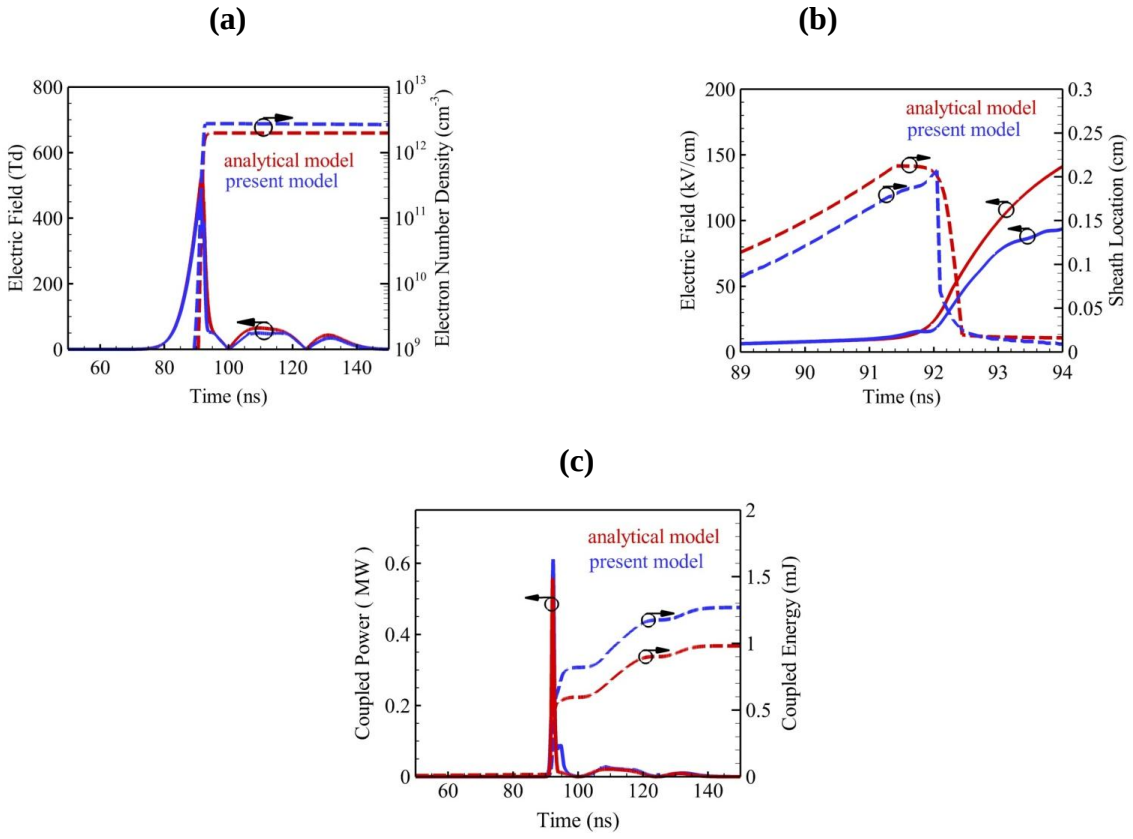

Figure 3.3 Comparison between analytical model results [25] and 1D model predictions for nanosecond discharge in N_2 at 60 *torr* and 300 *K*. (a) Electric field and electron number density in quasi-neutral plasma (x = 0.5 cm for 1D model), (b) input electrical power and input energy to the discharge, and (c) location of cathode sheath and electric field at sheath boundary as functions of time.

3.2.2 Repetitively Pulsed NS DBD in Air

Figure 3.4 shows the temporal evolution of the electric field and electron energy in the computational domain. The simulation was performed at an initial pressure and temperature of 62 *torr* and 300 *K*, respectively. The Gaussian fit of the CPT waveform shown in Fig. 3.1(b) is employed, with the voltage pulses applied at 40 *kHz* repetition rate. The initial electron density is fixed at $4x10^{8}$ cm^{-3}. The reduced electric field (E/N) at the center of the discharge volume (x = 0.5 *cm*) is shown in Fig. 3.4(a). The peak value of E/N (~450 *Td*) occurs during the primary breakdown stage approximately 25 *ns* from the beginning of the voltage pulse. Positive and negative space charge accumulation at the cathode and anode sheath boundaries respectively causes the gap voltage to drop and the field in the plasma rapidly falls to zero (by 28 *ns*). Two subsequent, albeit smaller, peaks in E/N are observed at around 38 *ns* and 60 *ns*; the time derivative of the applied voltage changes sign, causing the electric field in the plasma to change its direction. The additional energy coupled to the plasma goes almost exclusively to the vibrational mode, since E/N remains less than 60 *Td* during the two secondary breakdown phases. Repeated application of voltage pulses results in a periodic behavior of the discharge process, with the peak of E/N remaining nearly constant from pulse to pulse; the energy input during each voltage pulse remains fairly constant until a noticeable rise in temperature occurs.

The initiation of the nanosecond discharge can be clearly seen in Fig. 3.4(b), which depicts the spatial variation in the electric field. At 25 *ns*, an ionization wave moves rapidly towards the right electrode (which serves as the cathode for the negative half cycle of the CPT pulse), resulting in uniform production of charged and excited species in the discharge volume. A narrow sheath region develops near the cathode of ~ 0.2 *mm*

thickness at 27 *ns*, with the electric field reaching 140 *kV/cm*. It must be noted that the two-term expansion of the electron Boltzmann equation over-predicts ionization rates in high electric fields. Owing to the low electron density near the cathode and a small sheath thickness, however, the error incurred in predicting the overall discharge dynamics is not significant.

The evolution of electron energy during the discharge pulse is shown in Fig. 3.4(c). The overall trend follows that of the electric field with a peak value of 9 *eV* in the plasma volume at 25 *ns* when breakdown occurs. The electron energy in the region near the right electrode continues to rise and reaches 75 *eV* when the cathode sheath reaches its quasi-steady location. The left electrode serves as cathode in the positive half cycle of the CPT pulse, with electron energy peaking at 40 *eV*, close to the left boundary, at 60 *ns*.

Yin et al. [21] reported coupled pulse energy measurements during NS DBD at various pressures and repetition rates. Figure 3.5 shows the model predictions using the expression in Eq. 21 validated against experimental data. The input energy per pulse is a weak function of repetition frequency, as evident in Fig. 3.5(a). The operating conditions are 84 *torr* and 300 *K* for the initial pressure and temperature, respectively, using CPT waveforms to initiate the discharge. The model predictions are within 20% of the measured input energy of ~1.1 *mJ* per pulse, and remain fairly constant with pulse number. Figure 3.5(b) indicates that the coupled energy increases linearly with pressure, in line with experimental observations. In general, the input energy has been shown [21] to vary linearly with the number density and drop at higher pulse numbers (beyond ~200 pulses for a repetition rate of 40 *kHz*), due to a noticeable increase in temperature from the plasma heating process.

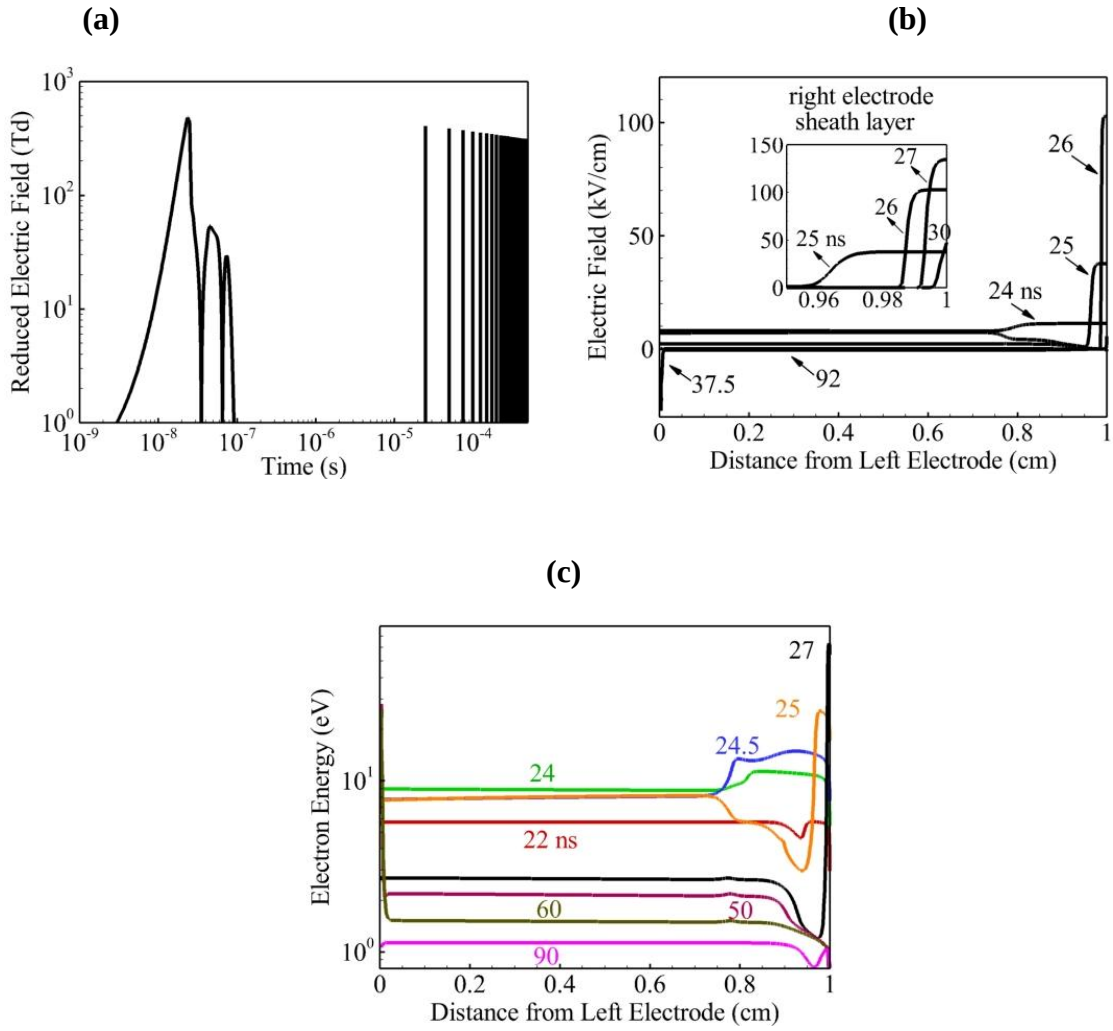

Figure 3.4 (a) Temporal evolution of reduced electric field for 25 voltage pulses. Spatial variation in (b) electric field, and (c) electron energy during the first voltage pulse. Simulation conducted in air at 60 *torr* and 300 *K* initial pressure and temperature, respectively, at 40 *kHz* repetition rate.

Figure 3.6 shows the production and decay of charged species during and after a high voltage pulse. During the primary breakdown phase (24-26 *ns*), a fast ionization wave propagates rapidly towards the cathode (right electrode, resulting in fairly uniform production of electrons over the entire domain, as evident in Fig. 3.6(a). The peak is located near the sheath boundary ~0.3 *mm* from the right electrode, with the electron

density an order of magnitude greater than that in the rest of the discharge volume ($5x10^{13}$ cm^{-3} vs. $2x10^{12}$ cm^{-3}). The disparity in time scales of production and decay of charged species in the plasma afterglow can be seen in Fig. 3.6(b). N_2^+ and O_2^+ are the dominant positive ions produced via electron impact ionization reactions during the primary breakdown timescale. By the end of the voltage pulse, N_2^+ is almost completely transformed to N_4^+ via three-body reaction and to O_2^+ via charge exchange reaction,

$$N_2^+ + N_2 + M \rightarrow N_4^+ + M \tag{3.1}$$

$$N_2^+ + O_2 \rightarrow O_2^+ + N_2 \tag{3.2}$$

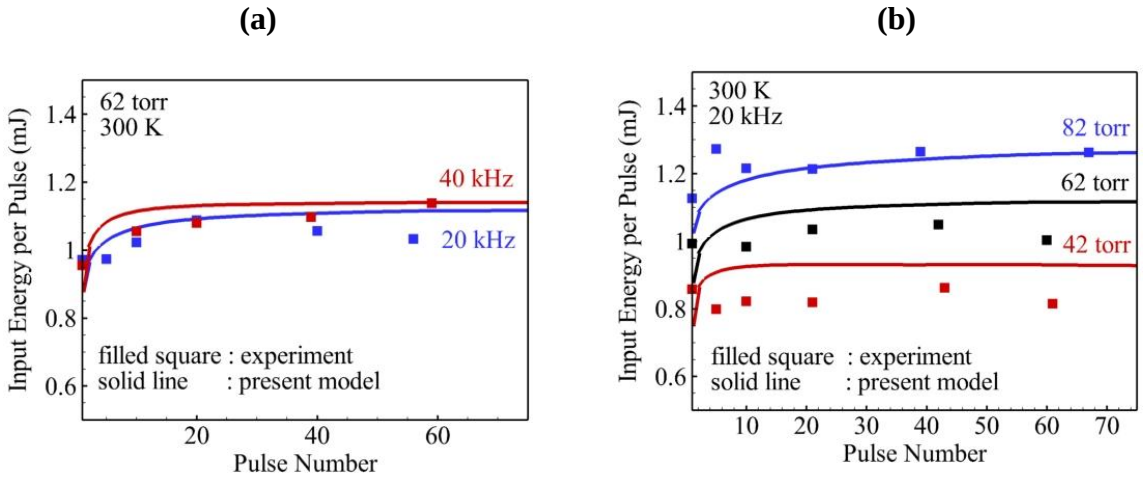

Figure 3.5 Comparison of input energy predictions with experimental measurements from [21], at (a) 62 *torr* and 300 *K* initial pressure and temperature, respectively, and (b) 300 *K* initial temperature and 20 *kHz* pulsing rate.

Decay of electron density occurs primarily through dissociative recombination of O_2^+ and N_2^+ and attachment reactions with O_2 forming O_2^- given by R3 and R4, respectively [59]. O_4^+ and O_2^- are the dominant charged species present in air plasma after 20 μs, by which time the electron density drops to ~10^{10} cm^{-3} in the entire domain.

$$O_2^+(N_2^+) + e \rightarrow O(N) + O(N) \tag{3.3}$$

$$e + O_2 + O_2 \rightarrow O_2^- + O_2 \tag{3.4}$$

Electronically excited N_2 species are produced with high efficiency in NS DBD during the initial breakdown phase, as seen in Fig. 3.7. This phenomenon can be attributed to E/N in the range of 100-300 *Td*, when electronic excitation is the dominant electron impact processes. Quenching of these excited species by O_2 is an important pathway for production of ground state and excited oxygen atoms, given in the following equation [49].

$$N_2(A^3, B^3, C^3, a^1) + O_2 \rightarrow N_2 + O + O\,(O(^1D), O(^1S)) \tag{3.5}$$

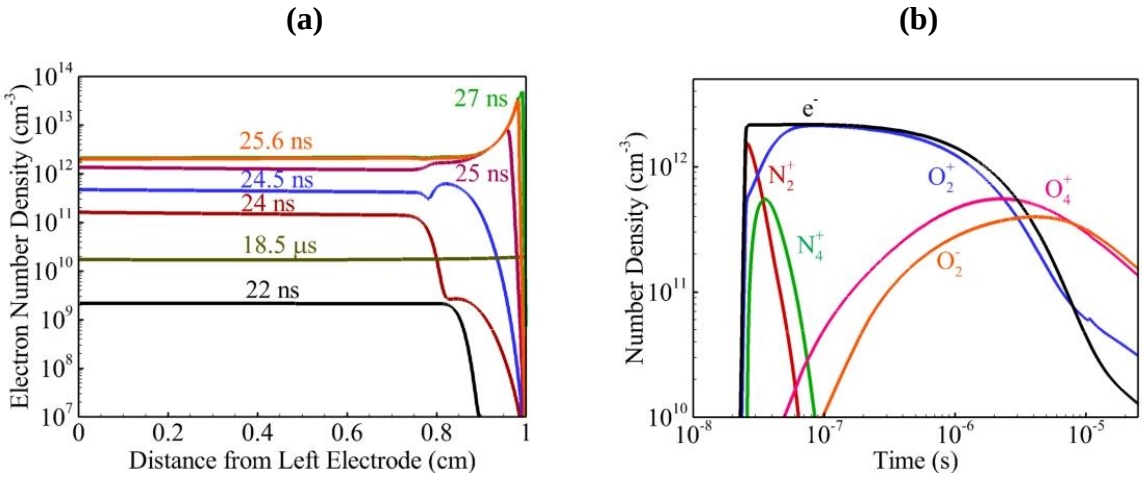

Figure 3.6 (a) Spatial and temporal evolution of electron density during a voltage pulse. (b) Variation of charged species densities in quasi-neutral plasma (x = 0.5 *cm*) as a function of time after a single nanosecond voltage pulse. Discharge in air at 60 *torr* initial pressure and 300 *K* initial temperature.

Longer lifetime active species such as O and $O_2(a^1)$ produced by nanosecond discharges have been shown to significantly influence ignition and combustion processes in fuel and air mixtures. Figure 3.8(a) shows the TALIF O atom measurements after a

single nanosecond pulse [25], and for a 100 pulse burst [27], compared with model predictions in quasi-neutral plasma (x = 0.5 *cm*). Good agreement for both single pulse and burst mode (100 *kHz*) cases suggest that the current kinetic model adequately describes the important O atom production and destruction pathways.

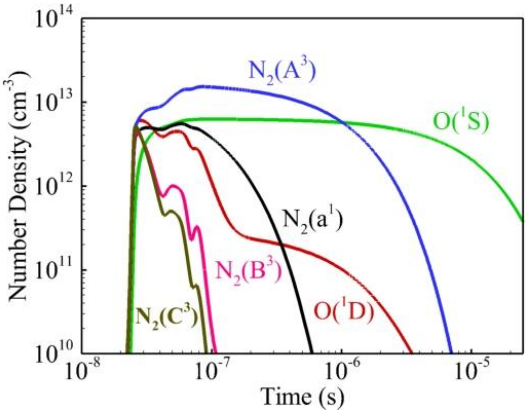

Figure 3.7 Time evolution of short lived electronically excited species after a single nanosecond pulse in air at 60 *torr* and 300 *K* initial pressure and temperature, respectively.

Temporal evolution of important longtime active species in the quasi-neutral plasma region for NS DBD in air (40 *kHz* repetition rate) is depicted in Fig. 3.8(b). Atomic oxygen is primarily produced via electron impact dissociation during the discharge pulses (R6), and then from quenching of electronically excited N_2 species by O_2 (R5), evident in Fig. 3.8(c). Approximately 40% of the O production occurs via R6, a majority of which happens within the primary breakdown phase (25-28 *ns*) of the voltage pulse. The remaining 60% is produced over ~200 *ns*, by which time the electronically excited N_2 species are completely quenched. Formation of ozone via three-body reaction R7 is the primary destruction pathway for O atom. This is a slow process and can equal or exceed O production rates only in the ms timescale.

$$O_2 + e \rightarrow O + O(O(^1D), O(^1S)) + e \tag{3.6}$$

$$O + O_2 + M \rightarrow O_3 + M \tag{3.7}$$

Singlet delta oxygen, $O_2(a^{'})$, is produced via electron impact excitation reactions during the discharge pulse, and later through relaxation of $O_2(b^1)$ excited state. Note that under the present conditions, $O_2(a^1)$ densities are an order of magnitude smaller than O atom densities, and the latter is clearly the dominant active species produced by pulsed NS DBD in air. Fig. 3.8(d) shows the spatial distribution of atomic oxygen from ns-ms timescales. The profiles are fairly uniform over the entire domain with a peak near the right electrode, where electron and excited N_2 densities are relatively high during the discharge pulses (see Fig. 3.6(a)). The destruction rate (R7) exceeds the production rate by 2 *ms*, especially near the peaks, resulting in more uniform spatial profiles.

In addition to producing active species, nanosecond plasma discharges may also influence ignition and combustion processes by heating the gas mixture over both short (*ns*) and long (*μs-ms*) timescales. During a high-voltage pulse, rapid heating is observed only near the boundaries, as shown in Fig. 3.9(a). Temperatures at the extremities rise by approximately 40 *K* within 100 *ns*. Ion Joule heating arising from the high electric fields in the sheath during breakdown, shown in Fig. 3.9(b) is responsible for this fast temperature rise. Note that both plots are shown over the duration of the first discharge pulse, with an initial temperature of 300 *K* over the entire domain.

In Fig. 3.10, the experimental measurements of temperature are plotted against model predictions at the center of the discharge volume over multiple discharge pulses at 40 *kHz* repetition rate with CPT waveform. The model results are in line with measured values, suggesting that temperature rise in air subjected to NS DBD is ~0.5-1 *K* /pulse.

Heating rates in fuel-air mixtures have been observed to be much greater, mainly due to higher chemical heat release from partial fuel oxidation [28].

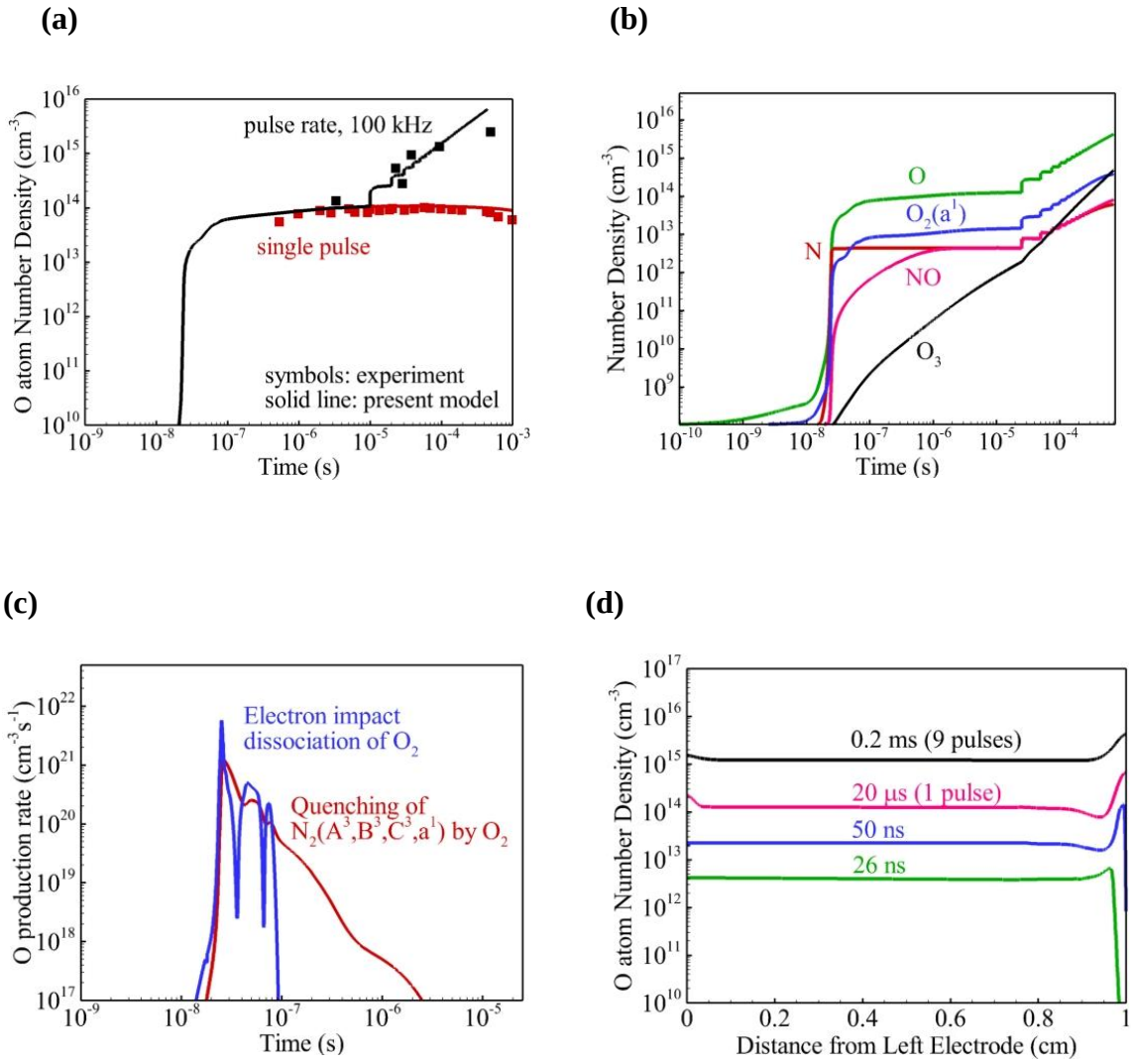

Figure 3.8 (a) TALIF O atom measurements after a single nanosecond pulse [26], and for a 100 pulse burst (100 *kHz* repetition rate) [27] compared with model predictions. (b) Temporal evolution of long lifetime active species in quasi-neutral plasma (x = 0.5 *cm*). (c) O production rate via electron impact dissociation and quenching of excited N_2 species by O_2 during and after first voltage pulse. (d) Spatial evolution of O density at various times. All simulations performed at 60 *torr* initial pressure and 300 *K* temperature, and 40 *kHz* repetition rate for cases depicted in (b), (c) and (d).

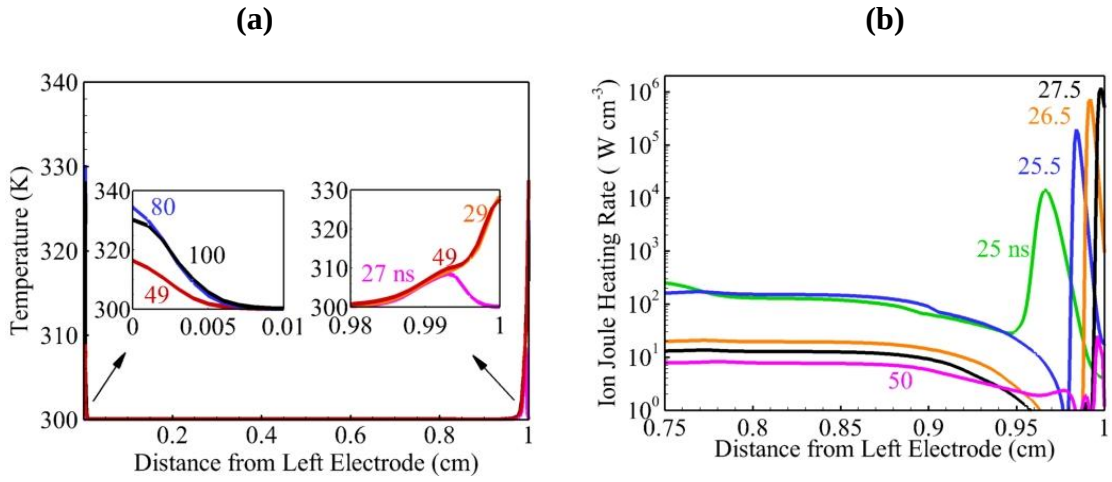

Figure 3.9 Spatial variation in (a) temperature, and (b) ion Joule heating rate during a single discharge pulse at 60 *torr* and 300 *K* initial pressure and temperature.

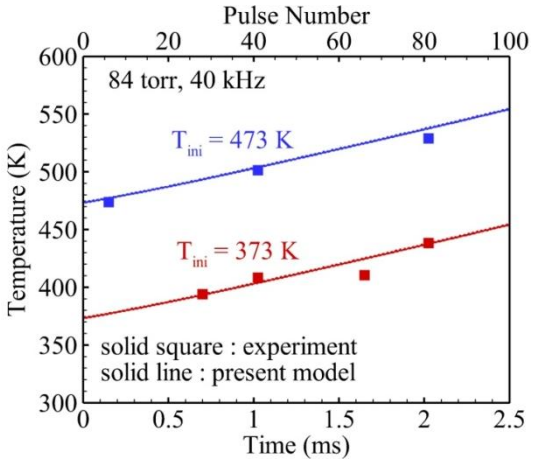

Figure 3.10 Comparison of measurements [20] and model predictions of temperature as a function of time at center of discharge volume at 84 *torr* initial pressure, 40 *kHz* repetition rate, and initial temperatures of 373 *K* and 473 *K*.

Chemical heat release from electron-ion recombination and quenching of excited species causes a fairly uniform temperature rise with kinks arising from waves generated from ion Joule heating, as shown in Fig. 3.11(a). The diffusive heat loss to the cooler

sections of the gas, along with conduction at the wall, results in rapid dissipation of thermal energy arising from ion Joule heating. It must be emphasized that intense heating rates are present only for a few *ns* during the breakdown process. The loss mechanisms, on the other hand, occur over several μs, and prevent overheating of the cathode layer and development of ionization instabilities. An interesting consequence of rapid ion Joule heating is formation of weak acoustic waves, which propagate into the discharge volume from both electrodes, as shown in Fig. 3.11(b). The speed of these acoustic waves can be estimated as ~ 500 ms^{-1}, which at 300 *K* in air is equivalent to a Mach 1.42 shock wave. Note that a normal adiabatic shock at this Mach number would result in a temperature rise of approximately 78 *K*. Homogeneous distribution of active species and thermal energy by pulsed NS DBD may help explain the volumetric ignition observed in preheated H_2-air and mixtures recently reported in [21], as opposed to traditional ignition at a hotspot.

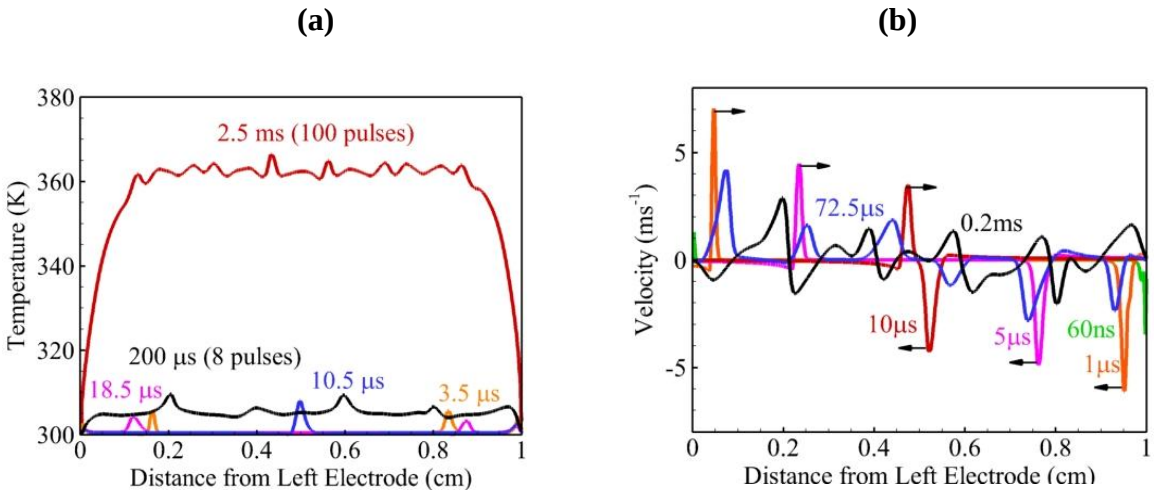

Figure 3.11 Spatial variation of (a) temperature, and (b) bulk velocity over multiple discharge pulses for 60 *torr* initial pressure and 300 *K* initial temperature at 40 *kHz* repetition rate.

3.3. Conclusion

A comprehensive analysis is performed to study the dynamics of energy coupling, gas heating, and generation of active species by repetitively pulsed nanosecond dielectric barrier discharges (NS DBD) in air. The simulations were performed with pressures between 40 and 100 *torr*, and pulsing frequency in the range of $1\text{-}10^5$ *Hz*. Results show good agreement with measurements of coupled energy, O atom density, and temperature in the discharge. During each high voltage pulse, the discharge develops in the form of a fast ionization wave resulting in nearly uniform excitation and dissociation of the gas mixture via electron impact reactions. The input electrical energy is directly proportional to the number density, and remains fairly constant on a per molecule basis from pulse to pulse. Repetitive pulsing causes uniform production of atomic oxygen in the discharge volume via electron impact dissociation during voltage pulses, and through quenching of excited nitrogen molecules in the afterglow. Charge accumulation at the sheath boundary causes the field in the plasma volume to drop immediately after breakdown. The field in the cathode sheath (~0.2 *mm* thickness), however, continues to rise with applied voltage, resulting in rapid gas heating through ion Joule effect, of approximately 40 *K* within 50 *ns*. Diffusion in the gas and conductive heat loss to the walls between voltage pulses prevents overheating of the cathode layer and development of ionization instabilities. A uniform temperature profile developed in the discharge volume after multiple pulses (~100 pulses) as a consequence of the chemical heat release from quenching of excited species. This finding explains recent experimental observations of volumetric ignition (as opposed to hot-spot ignition) in fuel-air mixtures subject to NS DBD.

CHAPTER 4

IGNITION OF H_2-AIR MIXTURES SUBJECTED TO PULSED, NANOSECOND PLASMA DISCHARGES IN A PLANE-TO-PLANE GEOMETRY

4.1 Introduction

The physio-chemical nature of pulsed nanosecond discharges in air was studied in the previous chapter. In this chapter, we make use of the modeling framework described in chapter 2 to perform comprehensive numerical investigations of pulsed nanosecond plasma assisted H_2-air (mildly preheated) ignition in a plane-to-plane geometry. Ignition is achieved in the decaying plasma after a burst of discharge pulses. One-dimensional simulations are performed to obtain information of the plasma generated radicals and heat release across the discharge gap. The uniform and diffuse nature of the preheated H_2-air plasma [28-31] justifies the 1D assumption. The accuracy of the model is assessed by comparing against experimental measurements. An accurate reduced chemistry mechanism is developed through sensitivity analysis to expedite the plasma ignition simulations. The sensitivity of input pulse energy and ignition characteristics to residual electron density and dielectric properties is analyzed. Electric field transients during each nanosecond pulse, and spatial evolution of gas temperature, excited species and radicals until ignition (ms timescales) are studied in detail. A special focus of this work is the question whether nanosecond pulsed plasma can produce volumetric ignition. The growth rate of the ignition kernel is studied in detail, investigating the roles played by heat transport and local radical chemistry.

4.2 Theoretical Framework

In the present work, we utilize the numerical model described in Chapter 2 to simulate ignition of preheated H_2-air mixtures excited by pulsed NS DBD. The electron transport and reaction coefficients are expressed as functions of electron energy using BOLSIG [17] and updated at every timestep through interpolation. The transport of species and energy is approximated using the drift-diffusion model. Equations for electric potential, electron energy, and charged and neutral species continuity are considered. In addition, the conservation equations for mass, momentum and energy of the gas mixture are solved simultaneously to model flow motions. At solid walls, a zero flux boundary condition is imposed for neutral species, mass and momentum conservation equations. Ion fluxes at the boundaries are expressed as sum of drift (due to electric field) and thermal velocity components, with the electron flux including a secondary emission component as well. The dielectric layer is treated as a semi-infinite solid to derive a self-consistent boundary condition for the gas energy equation [55]. An adaptive time-step approach is utilized to tackle the large disparity in timescales of various physical phenomena of interest. During each discharge pulse, the timestep is varied between 10^{-13} s-10^{-12} s to accurately capture the electric field transients and the electron energy relaxation process. In the time interval between pulses, the electric field is set to zero and the timestep is fixed at 10^{-9} s. Implicit time integration is performed for stiff chemical source terms, whereas species and flow transport are treated explicitly for computational efficiency. A non-uniform mesh consisting of 600 grid points, with highest resolution near the two dielectric boundaries, is used to obtain grid convergent solutions. A domain

decomposition approach with MPI (message passing interface) is implemented to compute the solution in parallel over multiple processors.

4.2.1 Physical Configuration

Figure 4.1(a) shows a schematic of the physical configuration used in the simulations, which is identical to the cross-section of the plasma flow reactor shown in Fig. 1. The total distance between the two copper electrodes is ~1.7 cm, with the discharge gap (distance between top and bottom quartz walls) being 1 cm. The quartz walls are 1.75 mm thick, and separated from each electrode by a 1.58 mm thick high temperature dielectric sheet (Kalrez, Dupont). The discharge gap is filled with a mixture of H_2 and dry air (79 % N_2, 21 % O_2). The dielectric constant specified by the manufacturer for Kalrez is $\varepsilon_s = 4.9$. Note that this value of ε_s was measured at 1 kHz field frequency, which is much lower than the characteristic frequency used in the present work (~10^7-10^8 Hz, see Fig. 4.1(b). In Sec. 4.2 the dielectric constant of Kalrez is varied between 5 and 9 to understand the sensitivity of input pulse energy and the ignition characteristics on uncertainty in dielectric properties. The dielectric constant of quartz is set at $\varepsilon_g = 3.8$ for all simulations in this work. The right electrode is connected to a high voltage power supply (CPT or FID pulser), whereas the left electrode is grounded. The measured nanosecond waveforms are shown in Fig. 2(b) along with the curve-fits used in present simulations. The CPT waveform consists of a bipolar pulse of duration 50 ns beginning to end, with peak voltages of -22.5 kV and 17.5 kV in the negative and positive half cycles respectively. The incident FID waveform is 10 ns long, followed by two reflected pulses, and is approximated by three Gaussian waves of peak voltages 27.5 kV, -20 kV and 13.5 kV respectively (see Fig. 4.1(b)).

(a) (b)

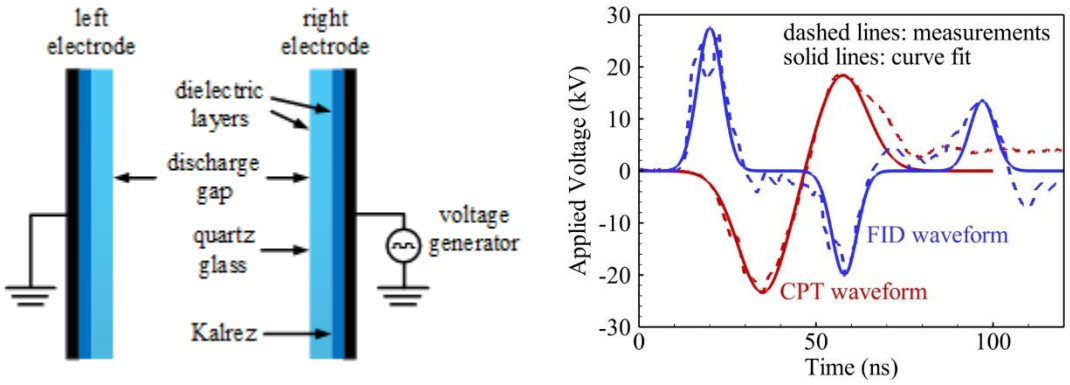

Figure 4.1 (a) Schematic of simulation configuration. (b) Experimental waveforms and corresponding curve-fits used in model calculations.

4.2.2 H_2-air Plasma Ignition Chemistry

Nanosecond discharges can produce a variety of ions, excited species and radicals. In order to gain quantitative insight into plasma ignition kinetics, a comprehensive chemistry dataset including all the important pathways is necessary. A detailed mechanism consisting of 35 species and 248 reactions was compiled by combining plasma air chemistry data with conventional H_2-O_2 reaction kinetics and hydrogen plasma reactions [27, 59]. Recent measurements [60] suggest that the rate constant of reaction $O+OH \rightarrow H+O_2$ used in [59] may not be accurate at low temperatures and is modified to give k = 5.3×10^{-11} cm^3/s at 500 K. Nitrogen vibrational temperature measured in preheated air (500 K, 100 torr) was quite low, 850 K after 50 pulses and 1050 K after 100 pulse [58]. The reason for this behavior can be attributed to the slow rate of plasma energy addition (0.8-1.0 mJ/pulse) and fast vibrational relaxation. In the present work, since the operating conditions are similar to those in [18], vibrational energy transfer processes are not considered a part of the chemistry mechanism (i.e. instantaneous relaxation assumed).

A reduced chemistry model was deduced through sensitivity analysis and consists of 19 species and 112 reactions. The reduced mechanism incorporates the neutral species N_2, H_2, O_2, H, O, O_3, OH, HO_2, and H_2O; charged species N_2^+, HN_2^+, H_3O^+, O_2^-, and e^-; and excited species $N_2(A^3)$, $N_2(B^3)$, $N_2(C^3)$, $N_2(a^1)$ and $O(^1D)$. Figure 3 shows that the model predictions with the reduced chemistry dataset are in excellent agreement with calculations using the full reaction mechanism. The evolution of charged species number density at the center of the discharge volume is depicted in Fig. 4.2(a). A stoichiometric H_2-air mixture is excited by a single nanosecond pulse (CPT waveform) at 94 torr and 473 K initial pressure and temperature. N_2^+ ions are produced via electron impact ionization during the breakdown process, but rapidly (in a few ns) reacts with H_2 to form HN_2^+ [59]. Accumulation of water vapor results in production of H_3O^+ ions 10 μs after the pulse [59]. The decay of electron density after the discharge pulse primarily occurs via recombination with positive ions (HN_2^+ and H_3O^+), and through attachment reaction with O_2 to form O_2^- [59]. Note that under present conditions, because of low ionization fraction ~10^{-6}, ion-molecule reactions do not play a significant role in neutral species kinetics. An order of magnitude comparison suggests that the ionization fraction has to increase to ~10^{-4} before ion-molecule chemistry becomes important.

The evolution of neutral species O, H, OH and H_2O for the same operating conditions is shown in Fig. 4.2(b). Atomic oxygen and hydrogen atoms are produced via electron impact dissociation and quenching of excited N_2 molecules [29]. OH is produced via quenching of $O(^1D)$ by H_2 (50-100 ns) and from HO_2 over longer timescales [59]. In order to further test the reduced model, we simulated a 7 pulse burst at 40 kHz repetition rate under the same initial conditions (94 torr and 473 K). Fig. 4.2(c) shows the evolution

of electron density at the center of the discharge volume over 7 voltage pulses. The two chemistry datasets predict almost identical electron density values, providing confidence to use the reduced chemistry mechanism for further calculations presented in this work.

(a) (b)

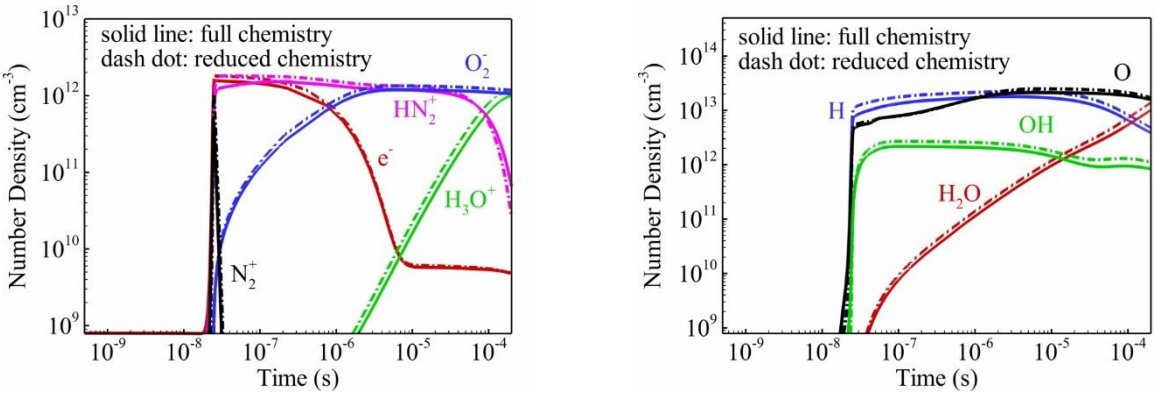

(c)

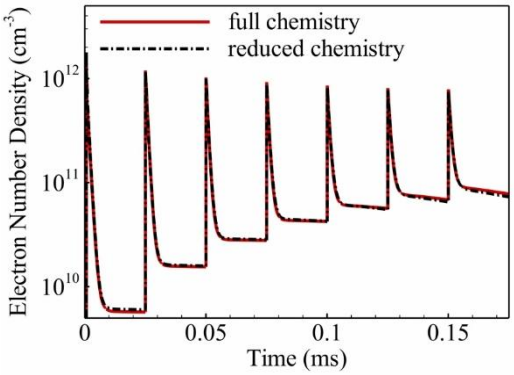

Figure 4.2: Comparison between predictions with reduced and full chemistry datasets for (a) charged, (b) neutral species densities for a single nanosecond discharge, and (c) electron density for a 7 pulse burst (94 torr, 473 K, 40 kHz, CPT pulser, ε_s = 9).

4.3 Results and Discussion

4.3.1 Electrical Characteristics of H_2-air Plasma

The applied voltage, gap voltage and conduction current over the duration of a nanosecond discharge pulse (CPT waveform) are shown in Fig. 4.3(a). The simulation is conducted for a stoichiometric H_2-air mixture at 114 torr and 473 K initial pressure and temperature (ε_g = 3.8, ε_s = 9). Breakdown in the gas volume is observed at ~9.5 kV, after which the conduction current rises rapidly to ~13 A. Charge accumulation on the dielectric layers creates a strong shielding effect, resulting in the gap voltage and current dropping to near zero within a few ns after breakdown. The current changes direction at ~36 ns, when the applied voltage begins to drop from its negative peak value.

The reduced electric field (E/N) at the center of the discharge gap, and coupled pulse energy are shown in Fig. 4.3(b). About 60 % of the total input energy (1 mJ) is coupled during the primary breakdown phase, when peak E/N ~400 Td. Note that additional energy coupled when the current reversal occurs goes primarily in vibrational excitation of N_2 molecules (E/N less than 100 Td). CARS measurements of nitrogen vibrational temperature in air [18] under present conditions, however, demonstrates that the vibrational nonequilibrium is insignificant and unlikely to have an effect on plasma kinetics. In all the modeling results presented in this work, we assume vibrational relaxation to be instantaneous.

Figure 4.4 shows variation in coupled discharge pulse energy for different pulse repetition rates at 114 torr and 473 K initial pressure and temperature. It is evident that the coupled energy changes by less than 10 % when the pulsing frequency is increased from 10 to 60 kHz. It appears that the residual electron density, which is a strong function of pulsing rate, has only a minor effect on input energy.

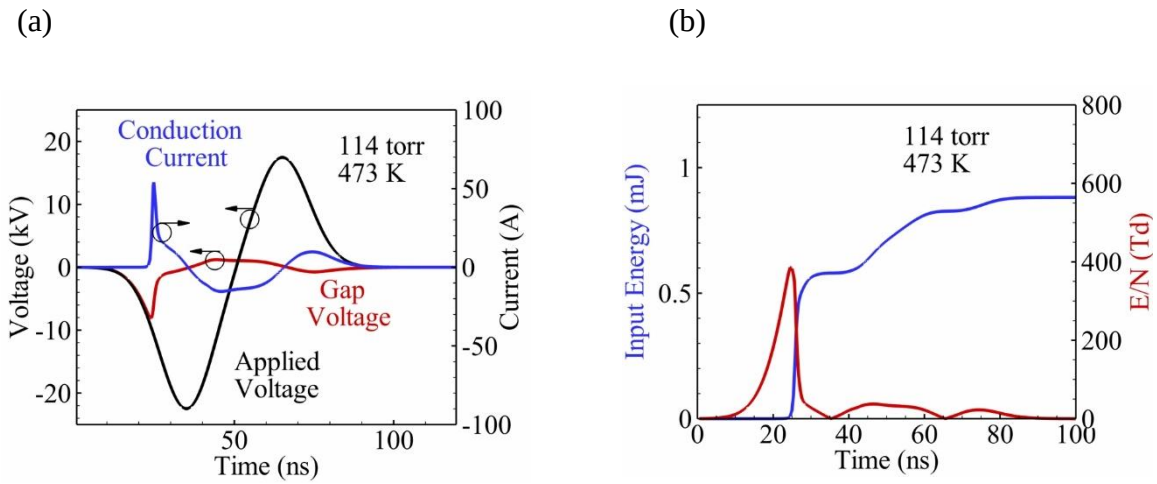

Figure 4.3: (a) Voltage current characteristics, and (b) input energy and E/N at center of discharge volume for a single nanosecond pulse in a stoichiometric H_2-air mixture (114 torr, 473 K, CPT pulser, ε_g = 3.8, ε_s = 9).

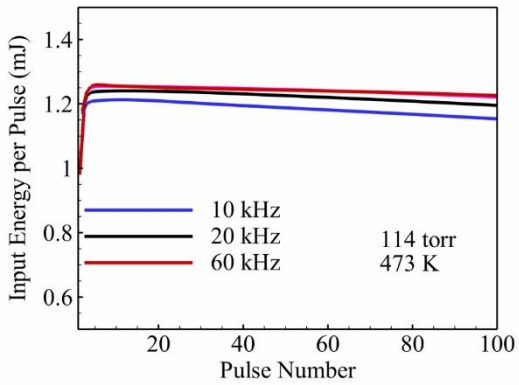

Figure 4.4: Input energy per pulse as a function of repetition rate for a burst of 100 pulses (114 torr, 473 K, CPT pulser, ε_g = 3.8, ε_s = 9).

4.4.2 Uncertainty in Dielectric Properties

The effect of uncertainty in dielectric properties on input pulse energy and plasma species production is shown in Fig. 4.5. A burst of 100 discharge pulses (CPT pulser) at 40 kHz repetition rate is simulated at 80 torr and 473 K initial pressure and temperature. Four cases are considered, with the dielectric constant of Kalrez layer set to ε_s = 5, 6, 7

and 9 respectively (ε_g = 3.8 for quartz). The input energy per pulse rises by more than 40 % as ε_s is increased from 5 to 9 as seen in Fig. 4.5(a). An analytical expression for input energy in nanosecond dielectric barrier discharges developed by Adamovich et al. [77], given by the following equation, provides insight into this behavior,

$$Q_{pulse} \approx \frac{1}{2} C \left[V_b^{\,2} + V_{peak}^2 \frac{\sqrt{2\pi}}{(\tau / RC)} \right] \tag{4.1}$$

where V_b and V_{peak} are breakdown voltage and peak voltage respectively, R the resistance of shielded plasma after breakdown, and τ the pulse duration parameter in the Gaussian fit of voltage waveform. C is the effective capacitance of dielectric layers obtained from the following equation,

$$C = \varepsilon_0 A [\frac{\varepsilon_s}{2l_s} + \frac{\varepsilon_g}{2l_g}] \tag{4.2}$$

where l_g and l_s are the thickness of quartz and Kalrez layers respectively, and A the electrode surface area. It is evident that increase in dielectric constants or decrease in thickness of the two layers has the effect of increasing the capacitance and hence the coupled pulse energy. Fig. 4.5(b) shows variation in atomic oxygen density and temperature at center of discharge volume for different dielectric constants for Kalrez layer. For ε_s = 5, the temperature at the end of the burst is 625 K, whereas for ε_s = 9, it is ~10 % higher at 680 K. As discussed in Sec. 4.3, the H_2-O_2 chain branching pathways "take-off" above a threshold temperature of ~700 K. As a consequence, the ignition delay time may drop by an order of magnitude when ε_s is increased from 5 to 9. Peak O atom density during the burst increases from 2.5x10^{14} cm^{-3} (ε_s = 5) to 3x10^{14} cm^{-3} (ε_s = 9), which is primarily due to increase in rates of electron impact excitation and dissociation (input energy increases with increase in ε_s). After 0.5 ms (20 pulses), O atom

consumption rate (via formation of OH) exceeds the production rate, irrespective of the ε_s value. Consequently, O atom concentration at the end of the burst is not sensitive to changes in the dielectric constant.

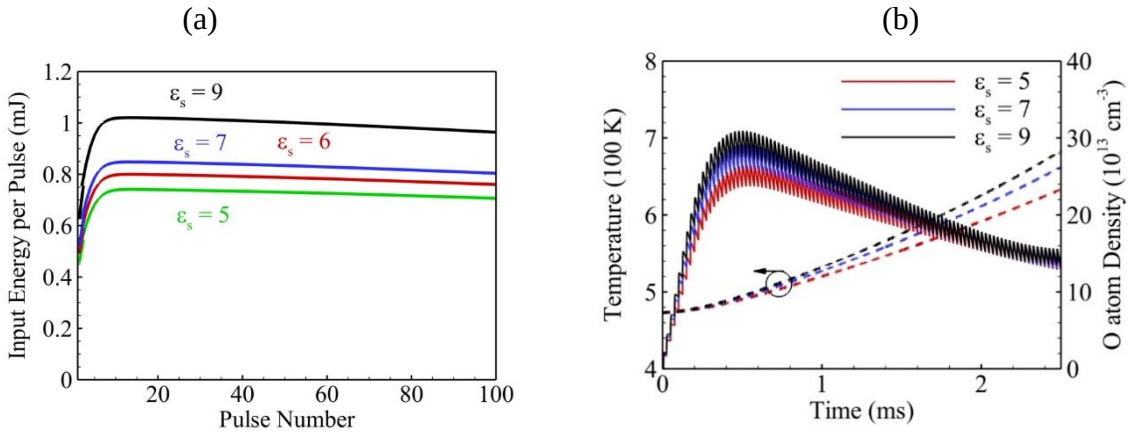

Figure 4.5: Variation in (a) input pulse energy, and (b) O atom density and temperature at center of discharge volume for different dielectric constant values of Kalrez layer (80 torr, 473 K, 40 kHz, CPT pulser, ε_g = 3.8).

4.4.3 Decaying Plasma Properties (non-ignition study)

Figure 4.6(a) shows the comparison between the measured absolute OH concentration and the model predictions after a 50 pulse burst (10 kHz repetition rate) at 100 torr and 500 K initial pressure and temperature (ε_g = 3.8, ε_s = 9). H_2-air equivalence ratios of 0.06 and 0.12 are considered in this study. Temperatures measured at the end of the discharge burst (2 μs after the last pulse) are also plotted for comparison with those predicted by the model. The model calculations agree well with the experimental data lending confidence in the chemistry dataset used and the numerical framework. The peak *OH* densities ($3x10^{13}$ cm^{-3}) are not sensitive to changes in equivalence ratio. In addition, there is no transient rise in OH concentration after the pulser is switched off. Model predictions of *O* and *H* atom densities after the pulse burst are shown in Fig. 4.6(b). The

timescales of decay of *O* and *H* densities are similar to that of OH consumption (1-2 ms) under present conditions. Peak density of *H* atoms is comparable to OH peak values, but atomic oxygen densities are higher (1-1.5x10^{14} cm^{-3}) because of the low equivalence ratios considered (ϕ = 0.06 and ϕ = 0.12). Note that *O* density is quite sensitive to change in equivalence ratio, increasing by nearly 50 % when ϕ is decreased from 0.12 to 0.06.

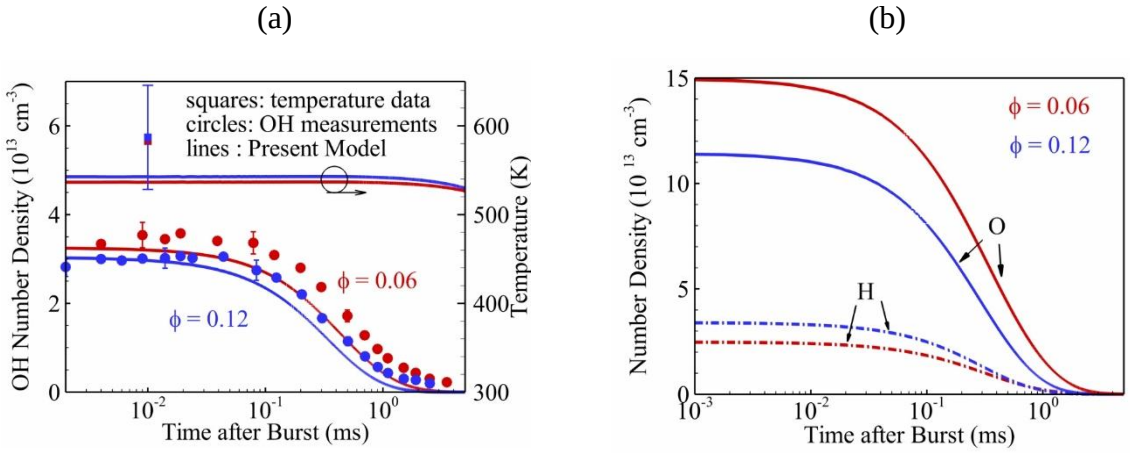

Figure 7: (a) Comparison between OH and temperature measurements with model predictions, and (b) O and H density decay at center of discharge volume after a 50 pulse burst (100 torr, 500 K, 10 kHz, FID pulser, ε_g = 3.8, ε_s = 6).

The low temperature oxidation process consists of recirculation of H and OH radicals and consumption of O through the following reactions,

$$H + O_2 + M \rightarrow HO_2 + M \tag{4.3}$$

$$O + HO_2 \rightarrow OH + O_2 \tag{4.4}$$

$$H + HO_2 \rightarrow OH + OH \tag{4.5}$$

$$OH + O \rightarrow H + O_2 \tag{4.6}$$

The H atom concentration is higher for larger ϕ, which leads to increase in OH and consumption of O via Eqns. (3-5). OH is then consumed to produce H via Eq. 6, and the

cycle repeats. The net outcome is that O consumption rate increases with ϕ. On the other hand, H and OH balance each other and are weak functions of ϕ.

4.4.4 Burst Mode Ignition Analysis

A series of experiments and simulations were conducted to investigate ignition of stoichiometric H_2-air mixtures in a decaying plasma after a burst of discharge pulses. The model predictions of temperature rise at the center of the discharge volume is shown in Fig. 4.7(a). The initial pressure and temperature are 80 torr and 473 K with ε_g = 3.8 and ε_s = 9 (CPT pulser, 40 kHz repetition rate). The measurements are made after the end of the discharge burst, with the system allowed to evolve without any further energy addition. A continuous rise in temperature is observed leading to ignition at 1.5 ms after the last discharge pulse for a burst size of 110 pulses. The ignition delay falls to 0.25 ms for a 130 pulse burst, demonstrating that the heating and radical pool generated by the nanosecond plasma substantially affect the ignition characteristics. No ignition is observed when the pulse burst is restricted to 100 pulses, with temperature rising to 710 K (1 ms after the burst), before heat loss from conduction exceeds the chemical heat release in the discharge domain. For a given set of initial conditions, the temperature at the end of the burst is critical to determine whether the mixture ignites or not. In this particular case (Figure 4.7), the threshold temperature at the end of pulse burst is ~700 K, below which no ignition is observed.

The ignition delay time, shown in Fig. 4.7(b), is calculated for different ε_s between 5 and 9, and compared with the experimental data under present conditions. Rapid rise in $OH(A \rightarrow X)$ emission is considered as the indicator of ignition in the experiments. In the simulations, ignition is defined as the point where a sharp “jump” in the temperature

profile occurs. The trend in ignition delay reduction with increase in number of pulses in a burst is well reproduced by the model. The figure also illustrates the sensitivity of ignition delay predictions to variation in dielectric properties, with ε_s = 6 providing the best match with measurements. This demonstrates that the input energy per pulse is ~0.8 mJ (see Fig. 4.5(a)) in a stoichiometric H_2-air plasma under present conditions. The ignition delay times are over-predicted by ~20% if the dielectric constant of Kalrez is taken as 4.9 (manufacturer specifications). This deviation may be because ε_s = 4.9 was measured at 1 kHz field frequency, which is much lower than the characteristic frequency used in the present work (~10^7-10^8 Hz, see Fig. 2(b)), so ε_s may change somewhat at high frequencies. In summary, Fig. 4.7(b) illustrates the importance of using a well characterized dielectric to validate the nanosecond plasma ignition model with measurements.

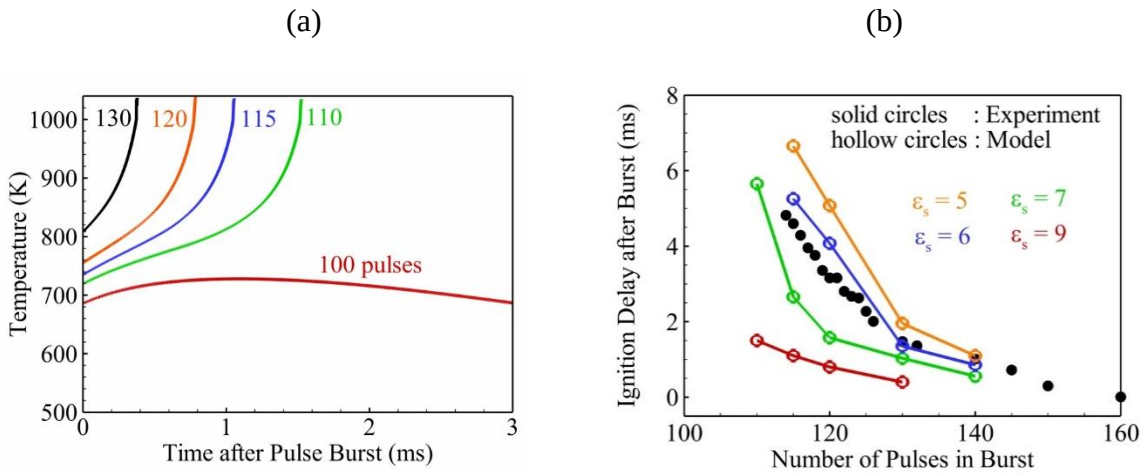

Figure 4.7. (a) Temporal evolution of temperature at center of discharge volume for ε_s = 9, and (b) ignition delay time as a function of number of voltage pulses in the burst (80 torr, 473 K, 40 kHz, CPT pulser, ε_g = 3.8).

Figure 4.8 shows the evolution of dominant radicals and temperature on the discharge centerline after a 120 pulse burst. The other operating conditions are the same as in Fig. 4.7. The concentrations of *O*, *H*, and *OH* at the end of the pulse burst are approximately $1x10^{14}$, $1x10^{15}$ and $8x10^{13}$ cm^{-3}, respectively, as seen in Fig. 4.8(a). During the discharge burst, *O* and *H* atoms are produced primarily by electron impact dissociation and quenching of excited N_2 molecules during each discharge pulse. An efficient pathway of *OH* formation is quenching of $O(^1D)$ by hydrogen molecules. Reaction of HO_2 with *O* is the dominant *OH* production pathway after 0.1 ms (4 pulses). The temperature rise in the discharge volume is ~1 K/pulse until 2.5 ms (100 pulses). The quenching of excited species is the primary source of heating in this timescale. Beyond this juncture, a substantial increase in volumetric heating rate is observed owing to fuel oxidation pathways triggered by plasma generated radicals. The dominant chain branching and oxidation processes triggered by radical generation in the plasma are given by the following reactions,

$$H + O_2 \rightarrow O + OH \tag{4.7}$$

$$O + H_2 \rightarrow H + OH \tag{4.8}$$

$$OH + H_2 \rightarrow H + H_2O \tag{4.9}$$

$$H + HO_2 \rightarrow O + H_2O \tag{4.10}$$

$$OH + HO_2 \rightarrow O_2 + H_2O \tag{4.11}$$

The rates of reactions at the center of discharge volume given by Eqns. 7-11 are shown in Fig. 4.8(b). The buildup of *O* atom density during the discharge burst triggers the chain branching processes of Eqns. 7 and 8. At 1 ms (i.e. after 40 pulses), the increase in reaction rate of Eq. 8 explains the steep reduction in *O* number density, and rapid rise in

H concentration (see Fig. 4.8(a)). Note that the chain branching reactions are highly temperature sensitive. The primary oxidation reaction is given by Eqn. 9, whereas the other two pathways (Eqns. 10 and 11) lend minor contributions to H_2O production. Increase in chain branching reaction rates produce *OH*, which then accelerates the heat release from fuel oxidation. The increase in temperature completes the cycle by further increasing the rates of Eqns. 3 and 4. This non-linear feedback cycle causes an exponential increase in temperature and radical concentration leading to ignition.

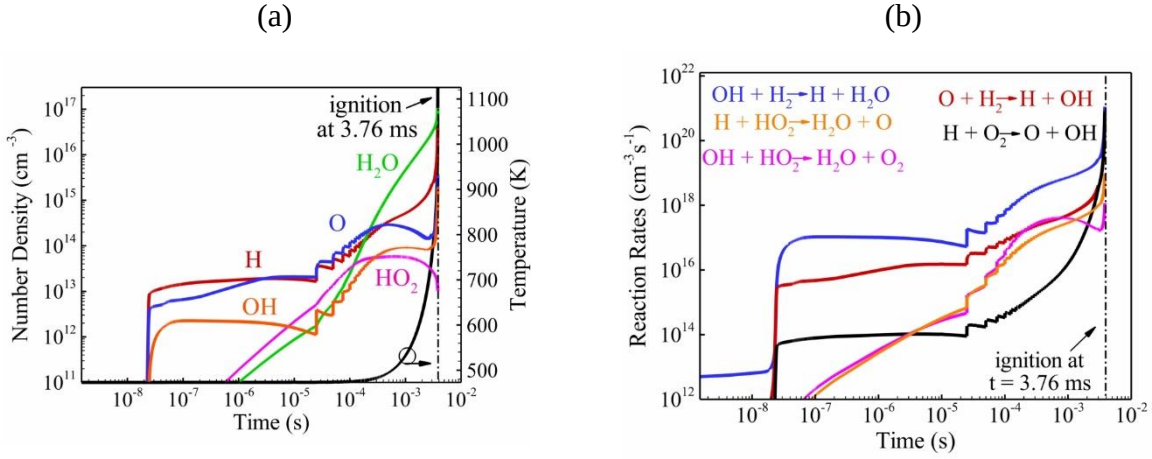

Figure 4.8. (a) Evolution of species densities and temperature and (b) dominant chain branching and oxidation reaction rates at center of discharge volume leading to ignition after a burst of 120 pulses (80 torr, 473 K, 40 kHz, CPT pulser, ε_g = 3.8, ε_s = 9).

It must be emphasized that in the presence of a large pool of radicals generated by a nanosecond discharge burst, heating the gas mixture by exothermic chemical reactions to ~700 K is sufficient to achieve ignition after a delay after the burst. Ignition can never be achieved if the nanosecond plasma source is replaced with a uniform heating device which is turned off when the temperature reaches ~730 K (heating caused by recombination of all radicals generated during the nanosecond discharge burst can at

most result in a temperature rise of 30 K under present conditions). This suggests that the radicals generated by the plasma initiate oxidation reactions, thereby releasing some of the chemical energy “locked" in the fuel molecules. The temperature rise in Fig. 4.7(a) after the end of the pulse burst (after 3 ms) is entirely due to this effect. The rapid heating process continuously accelerates the temperature-sensitive chain branching reactions leading to ignition. A detailed analysis of nanosecond plasma kinetics and ignition was performed by Yin et al. [28]. No ignition was observed in calculations performed by switching off the dominant plasma radical generation processes after a discharge burst (end temperature 700 K). The mixture had to be heated to a centerline temperature of 900 K in order to achieve thermal ignition.

The spatial evolution of temperature, shown in Fig. 4.9, reveals further interesting features of nanosecond plasma assisted ignition. The operating conditions are the same as in Fig. 4.7. The model prediction on a relatively short timescale (burst duration less than 0.5 ms) is shown in Fig. 4.9(a). During each discharge pulse, ion Joule heating in the cathode sheath layers results in rapid increase in temperature of ~30 K near the walls. A similar behavior was observed for nanosecond discharges in air (see Chapter 3). Quenching of excited species in the plasma volume results in a steady and uniform rise in temperature of ~1 K/pulse throughout the discharge burst. Temperature profiles on the longer timescale are shown in Fig. 4.9(b). The temperature distribution after 60 pulses is almost flat, with lower values near the boundaries because of heat loss by conduction to the walls. By the end of the discharge burst (after 120 pulses), the peak temperature at the center is ~730 K. As discussed earlier, heat release from partial fuel oxidation continues to increase the temperature after the plasma source is turned off. The temperature profile,

however, exhibits a more pronounced maximum near the centerline, as seen at 3.75 ms. Ignition is first observed at the center where a sudden jump in temperature is observed at approximately 3.76 ms. The ignition kernel expands rapidly outwards at a rate of ~30 ms^{-1}. For comparison, the unstretched laminar flame speed for a stoichiometric H_2-air mixture at 0.2 atm has been reported to be ~2 ms^{-1} [78]. It must be emphasized that under present conditions, flame (if present) is propagating into a preheated mixture doped with radicals from the discharge burst. Hence, the actual flame speed may be higher the speed of a laminar flame propagating into an unburnt mixture.

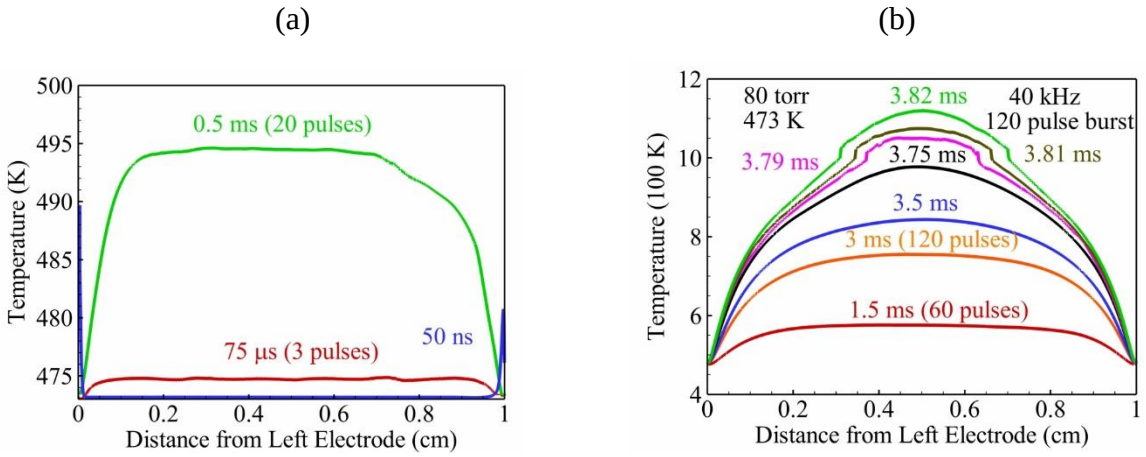

Figure 4.9. Spatial distribution of temperature at different times showing the expansion of the ignition kernel after a 120 pulse burst (80 torr, 473 K, 40 kHz, CPT pulser, ε_g = 3.8, ε_s = 9).

There are two possible mechanisms controlling the growth of the ignition kernel. (a) Local plasma radical chemistry processes can bring the mixture to ignition threshold, after which it ignites after a time delay. (b) Heat transport from the core of the ignition kernel raises the temperature near the boundaries to the ignition threshold, leading to flame propagation into the unburnt mixture. In order to explore the role of heat transport, we simulated ignition in a decaying plasma after the pulse burst with the species diffusion

coefficients and thermal conductivity reduced by a factor of 100. The other operating conditions are same as in Fig. 4.9. Note that all the transport effects were present during the burst and "switched off" only after the last pulse. The spatial evolution of temperature with and without modifications to the heat transport properties is shown in Fig. 4.10. It is clear that the ignition kernel expands at nearly the same rate with or without heat transport. This demonstrates that ignition is achieved in a "lagging" fashion at different locations in the discharge volume, when the radicals and heating produced by the plasma take the mixture above a threshold temperature (~700 K under present conditions).

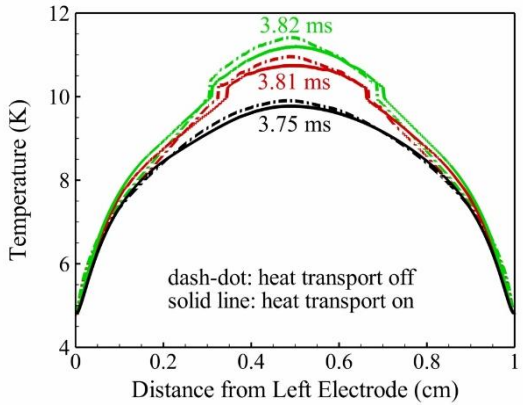

Figure 4.10: Spatial distribution of temperature during ignition with and without considering heat transport processes after a 120 pulse burst (80 torr, 473 K, 40 kHz, CPT pulser, ε_g = 3.8, ε_s = 9).

Figure 4.11 shows a series of ICCD camera images of nanosecond discharge and ignition in a stoichiometric H_2-air mixture. The initial pressure and temperature are 104 torr and 473 K respectively (CPT pulser, 40 kHz repetition rate). The plasma images were taken during individual discharge pulses, whereas the flame images were taken after the end of the burst. It is clear that the plasma is uniform and diffuse throughout the burst after the first few pulses. Ignition is first observed near the edge of electrodes, but the kernel expands rapidly to encompass the whole discharge volume in less than 0.2 ms.

This is clear evidence of large volume ignition by the nanosecond plasma source. In the flame image taken at 5.1 ms, it can be seen that ignition first occurs near the center of the discharge gap at different axial locations and spreads towards the boundaries, consistent with the predictions of the present one-dimensional model.

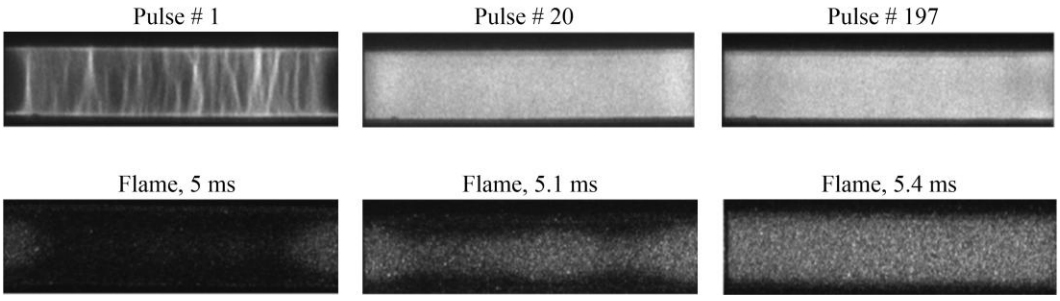

Figure 4.11. ICCD images of nanosecond plasma and ignition in a stoichiometric H_2-air mixture (104 torr, 473 K, 40 kHz, CPT pulser). The camera gate is 2 μs for plasma images and 30 μs for flame images.

Figures 4.12 and 4.13 show the spatial distribution of dominant chemical species across the discharge gap for ignition in a stoichiometric H_2-air mixture after a 120 pulse burst. The operating conditions are the same as in Fig. 9. The peak H atom density increases ~12 times from $2x10^{15}$ cm^{-3} at 3 ms to $25x10^{15}$ cm^{-3} after ignition (3.82 ms), as evident in Fig. 4.12(a). The evolution of atomic oxygen is similar, as shown in Fig. 4.12(b). A small increase in temperature near ignition significantly increases the chain branching reaction rates. As a consequence, the radical concentration profiles are much steeper than the temperature distribution, with well pronounced maxima near the centerline.

OH and H_2O distributions are shown in Figs. 4.13(a) and (b) respectively. Peak value of OH concentration increases by ~20 times after ignition from the end of the pulse

burst (3 ms), from $1x10^{14}$ cm^{-3} to $2x10^{15}$ cm^{-3}. The water concentration increases at a somewhat slower rate, rising by 10 times after ignition, although the absolute values are much higher. It is interesting to notice that both OH and H_2O profiles exhibit secondary peaks near the dielectric boundaries. During the discharge burst, higher E/N values near cathode sheath edges result in rapid excitation and radical production. However, in the decaying plasma after the burst, electric field effects are completely absent and cannot account for the secondary peaks near the boundaries. It is more plausible that the low temperatures near the boundaries aid the accumulation of HO_2, which is slowly converted to H_2O by reactions of Eqns 10 and 11. OH is produced by HO_2 from the reaction in Eqn. 4.

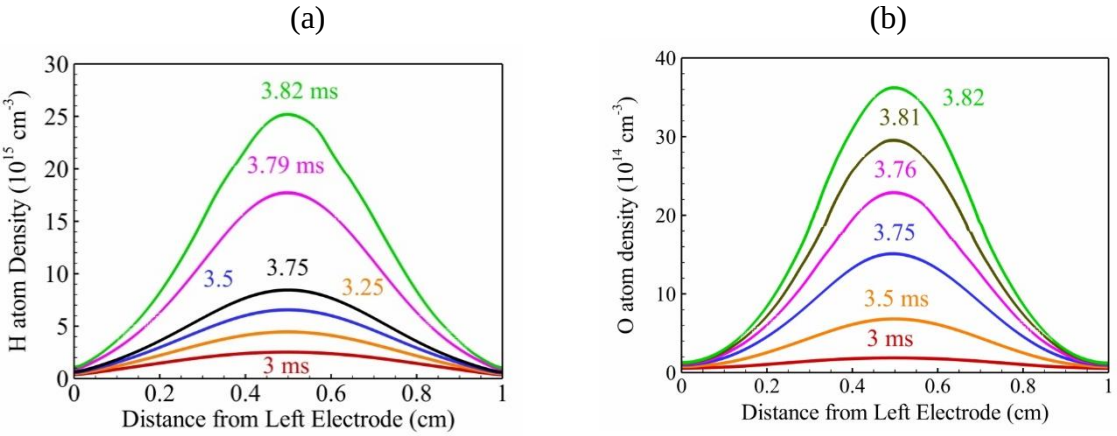

Figure 4.12: Spatial distribution of (a) H and (b) O number densities across the discharge gap at different times leading to ignition after a 120 pulse burst (80 torr, 473 K, 40 kHz, CPT pulser, ε_g = 3.8, ε_s = 9).

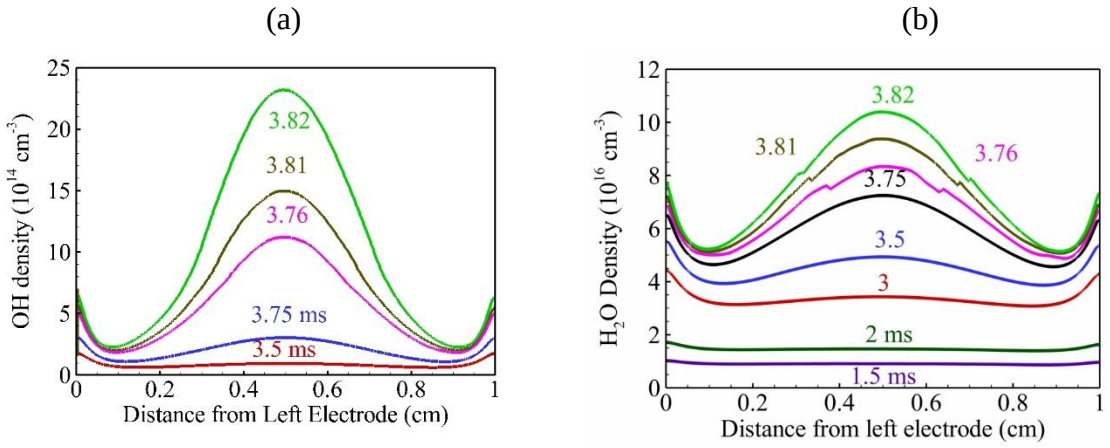

Figure 4.13: Spatial distribution of (a) OH and (b) H_2O number densities across the discharge gap at different times leading to ignition after a 120 pulse burst (80 torr, 473 K, 40 kHz, CPT pulser, ε_g = 3.8, ε_s = 9).

4.5 Conclusions

One-dimensional simulations were conducted to provide insight into the ignition of H_2-air mixtures excited by pulsed nanosecond dielectric barrier discharges. The gas mixture was mildly preheated (400-500 K) to create diffuse and uniform plasma in a parallel plate discharge cell. The studies were performed in a decaying plasma after a burst of high-voltage pulses. A self-consistent plasma fluid framework was utilized to simulate the species and temperature evolution across the electrode gap in ns-ms timescales. A reduced chemistry mechanism consisting of 19 species and 112 reactions was inferred through sensitivity analysis. The model predictions showed good agreement with OH concentration, temperature and ignition delay measurements. At the present conditions, since the energy was added to the plasma relatively slowly, vibrational nonequilibrium did not play a significant role in plasma kinetics (due to rapid relaxation). However, this may not be the case when energy is added rapidly, such as in a discharge filament.

Both the experiments and simulations showed that the ignition characteristics were highly sensitive to input plasma energy. Changing the dielectric constant of Kalrez from 5 to 9 produced significant variations in ignition delay predictions, with ε_s = 6 provided the best match between measurements and calculations. The effectiveness of plasma generated radicals in triggering partial fuel oxidation was found to depend on the temperature at the end of the pulse burst (T_f). When T_f exceeded 700 K, the temperature continued to rise even after the plasma source was switched off. Acceleration of the conventional H_2-O_2 chain branching pathways resulted in ignition after a short time delay after the burst. Both ICCD camera images and model predictions showed that ignition first occurs at the center of the discharge volume. The kernel, however, expanded rapidly towards the boundaries at a speed of ~30 ms^{-1}. The expansion rate of the ignition kernel remained unaltered even when the heat transport coefficients were reduced by a factor of 100 in the model. This suggested that the ignition kernel growth is primarily due to local plasma chemistry effects rather than flame propagation, and heat transport does not play a significant role. The nanosecond pulse discharge plasma excitation resulted in nearly simultaneous ignition over a large volume, in sharp contrast to hot-spot igniters. This work demonstrated that the low-temperature plasma-assisted ignition in H_2-air is well understood, i.e. that kinetics incorporated into the model described fuel oxidation by reactions of plasma-generated radicals, resultant temperature rise, and ignition adequately.

CHAPTER 5

A "FROZEN ELECTRIC FIELD" APPROACH TO SIMULATE REPETITIVELY PULSED NANOSECOND PLASMA DISCHARGES

5.1 Introduction

In this chapter, we put forward a novel numerical strategy to tackle the multi-scale nature of NRPD, with the help of physical insight gained from our previous studies of the electrical characteristics of pulsed nanosecond discharges. We propose a "frozen electric field" modeling approach to expedite the NRPD simulations without adverse effects on the correctness of the solutions. The procedure involves two steps. First, a burst of nanosecond voltage pulses is simulated using a self-consistent, nonequilibrium plasma modeling framework described in [12-13]. The simulation is continued until the discharge reaches a stationary state, i.e., the electrical characteristics during two consecutive voltage pulses show variations within a specified bound. The calculated spatial distributions and temporal evolution of the electric field, electron density and electron energy are then stored in a library. Next, the calculations of these properties are suspended. The electrical characteristics of subsequent pulses are frozen at the values in the library. By adopting this strategy, the timestep for numerical integration can be increased by four orders of magnitude (from 10^{-13} s to 10^{-9} s), thereby significantly improve the computational efficiency.

The validity of such frozen electric field modeling approach is based upon the periodic behavior of pulsed nanosecond discharges. During a voltage pulse, the production rate of electrons is a function of the gas number density, mixture composition and initial electron concentration (residual or remnant charges from the previous pulse) in

the discharge gap. The residual electron density is dependent on the ion-electron recombination and electron attachment rates which are sensitive to the pressure and mixture composition, respectively. In addition, the flow residence time and pulsing frequency affects the residual charge concentrations. The flow field has negligible impact on the discharge dynamics so long as $U_f \times T_i << d_g$, where U_f is the flow velocity, T_i the time interval between two consecutive pulses, and d_g the gap between the electrodes. The plasma generated radicals and excited species have a weak impact on the discharge development due to their low concentrations (typically less than 1%). Consequently, the electrical dynamics during a burst of nanosecond discharge pulses may exhibit periodic behavior for low flow velocities and in the absence of significant variations in the gas number density or mixture composition. Tholin et al. [14] observed similar behavior in their 2D simulations of pulsed nanosecond discharges in a pin-pin geometry at 1 atm pressure. The plasma reached a "quasi-periodic" glow regime with repetitive application of voltage waveforms. The spatio-temporal evolution of the electric field and electron density remained constant during each pulse.

We conduct one-dimensional simulations of pulsed nanosecond dielectric barrier discharges in plane-to-plane geometry at low pressures in H_2-air mixtures with detailed chemical kinetics. The paper is organized as follows. Section 2 describes the simulation configuration and the modeling framework. In Sec. 3.1, a burst of 10 nanosecond voltage pulses is simulated using a detailed plasma model with electrical characteristics calculated during each pulse, in order to demonstrate the periodic nature of NRPD. The frozen electric field modeling approach is then described in Sec. 3.2, and its predictions are benchmarked against those by the detailed plasma model. In Sec. 3.3, ignition of H_2-

air mixtures subject to dielectric barrier NRPD is simulated using the frozen approach over a range of pressures (54-144 torr) and equivalence ratios (0.7-1.2). The calculated ignition delay and temperature are compared with experimental measurements reported in [14] to critically assess the accuracy and robustness of the frozen modeling strategy.

5.2 Theoretical Framework

5.2.1 Physical Configuration

Figure 5.1(a) shows schematically the physical configuration of concern, simulating the plasma flow reactor experiment described in [27]. The quartz walls are 1.75 mm thick, and separated from each electrode by a 1.58 mm thick high temperature dielectric adhesive sheet (silicone rubber). The discharge gap is 1 cm wide and is filled with a mixture of H_2 and dry air (79 % N_2, 21 % O_2). The dielectric constant for quartz is $\varepsilon_g = 3.8$. The dielectric constant of silicone rubber is strongly dependent on its chemical composition and temperature ($\varepsilon_s = 3.2 - 9.8$). This introduces significant uncertainty in the coupled energy during nanosecond voltage pulses. We performed a sensitivity study and found that $\varepsilon_s = 6.0$ provide the best match between the calculated and measured ignition delay times. In all the simulations presented in this work, the dielectric constant of silicone rubber is fixed at 6.0. The right electrode is connected to a high voltage power supply (CPT pulser), whereas the left electrode is grounded. Figure 5.1(b) shows the measured nanosecond waveforms along with the curve-fits used in the present simulations. The CPT waveform consists of a bipolar pulse of duration 100 ns with peak voltages of -22.5 kV and 17.5 kV in the negative and positive half cycles respectively. The simulations are conducted with pressures in the range of 54 - 144 torr, and equivalence ratios between 0.7 - 1.2.

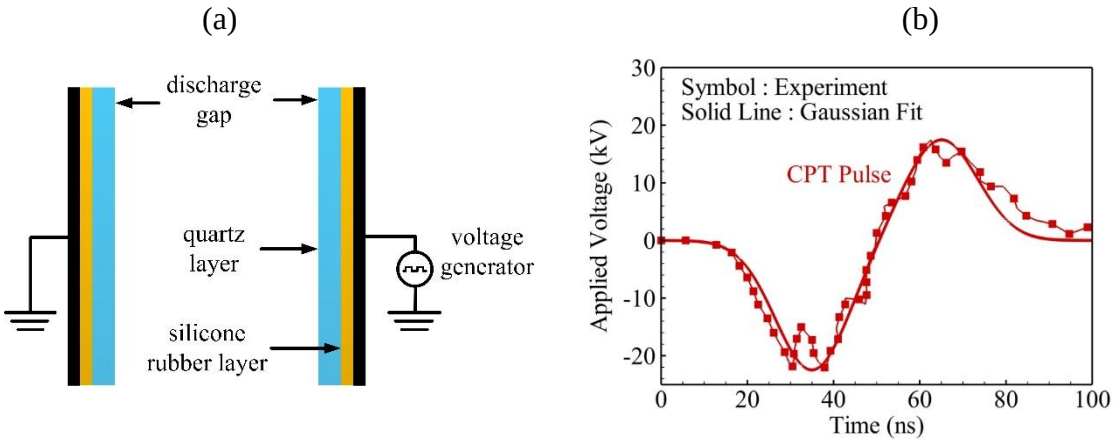

Figure 5.1: (a) Schematic of simulation configuration. (b) CPT experimental waveform and corresponding curve-fit used in model calculations.

5.2.2 Governing Equations

The details about the self-consistent NRPD model employed in the present work are described in chapter 2. Conservation equations for the electric potential, electron energy, and charged and neutral species continuities are considered. The formulation also accommodates conservation of mass, momentum and energy of the gas mixture to characterize flow motions. The electron transport and reaction coefficients are expressed as functions of electron energy using BOLSIG software [17]. Details about the numerical methods, and associated initial and boundary conditions can be found in chapter 2.

In the frozen approach, the electric field dynamics are calculated for a few voltage pulses until the discharge reaches a stationary state. The electrical characteristics in the subsequent pulses then remain fixed, with calculations of the electric potential, electron density and electron energy suspended until the end of the simulation.

5.2.3 Initial and Boundary Conditions

At solid walls, a zero flux boundary condition is imposed for the conservation equations of mass, momentum and neutral species concentrations. Ion and electron fluxes at the boundaries are expressed as the sum of the drift (due to electric field) and thermal velocity components. The electron flux also includes a secondary emission component at the cathode. Boundary conditions for the gas energy equation must be properly specified to predict the temperature evolution in the discharge volume. In this work, we make use of the wall boundary conditions derived in chapter 2 by treating the dielectric layer as a semi-infinite solid. The initial $H_2/O_2/N_2$ densities are determined by the initial pressure, temperature and equivalence ratio information. The remaining species densities are initialized to 10^8 cm^{-3} except for electron density which is initially set at $2x10^8$ cm^{-3} to ensure charge neutrality.

5.2.4 Numerical Methods

The conservation equations are solved by means of a second-order Strang splitting method to treat convection-diffusion and chemical source terms separately. Implicit time integration is performed for stiff chemical source terms, whereas species and flow transport are solved explicitly for improved computational efficiency. A domain decomposition approach with MPI (message passing interface) is implemented to facilitate parallel computation over 48 processors. In all the simulations, a non-uniform mesh with 600 nodes is used to obtain grid independent solutions.

5.2.5 H_2-air Nanosecond Plasma Ignition Kinetics

The baseline H_2-air chemistry mechanism used in the present work has been carefully validated previously. The scheme consists of 19 species and 111 reactions. It

incorporates the neutral species N_2, H_2, O_2, H, O, O_3, OH, HO_2, and H_2O; charged species N_2^+, HN_2^+, H_3O^+, O_2^-, and e^-; and excited species $N_2(A^3)$, $N_2(B^3)$, $N_2(C^3)$, $N_2(a^1)$ and $O(^1D)$. A detailed plasma kinetic analysis showed that dominant positive and negative ions in pulsed nanosecond $H_2/O_2/N_2$ discharges are H_3O^+ and O_2^- respectively. Atomic oxygen and hydrogen atoms are produced during discharge pulses via electron impact dissociation of O_2 and H_2 molecules respectively. In the time duration between the voltage pulses, quenching of excited N_2 species by O_2 and H_2 also contribute to production of O and H atoms respectively. At temperatures below 700 K, OH is primarily generated from reactions of HO_2 with O and H radicals.

Takashima et al. [18] measured N_2 vibrational temperature in air at 60 torr pressure after a burst of nanosecond plasma pulses in a plane-to-plane geometry. The reported values were quite low, 850 K after 50 pulses and 1050 K after 100 pulses. This behavior was attributed to the slow rate of plasma energy addition (0.8-1.0 mJ/pulse) and fast vibrational relaxation. In the present work, since the operating conditions are similar to those in [18], vibrational processes are not considered as part of the chemistry mechanism (i.e. instantaneous vibrational relaxation is assumed).

5.3 Results and Discussions

5.3.1 Periodicity of pulsed nanosecond discharge dynamics

Detailed discussions about the electrical characteristics of NRPD in H_2-air mixtures can be found in the previous chapter. The focus here is to demonstrate the periodic nature of the discharge dynamics under repetitive application of nanosecond voltage pulses. The self-consistent 1D plasma model described in chapter 2 is used to perform the simulations described in this section. The spatial uniformity of nanosecond

plasma at low pressures justifies the 1D assumption [27-28]. Figure 5.2(a) shows the temporal evolution of electron density at the center of the discharge volume for a burst of 20 pulses at a pressure of 114 torr, an initial temperature of 473 K and a pulsing rate of 40 kHz. It is evident that the electron density reaches a stationary state after about 8 pulses. The electron production and decay rates remain the same during each pulse for the reminder of the burst at this spatial location. Figure 5.2(b) shows the spatial distribution of the electron density in the discharge gap at the end of the 1st, 3rd, 10th and 20th pulses, respectively. The maximum differences in the electron density after the 3rd and 10th pulses is about 10%, whereas it is less than 5% between the 10th and 20th pulses.

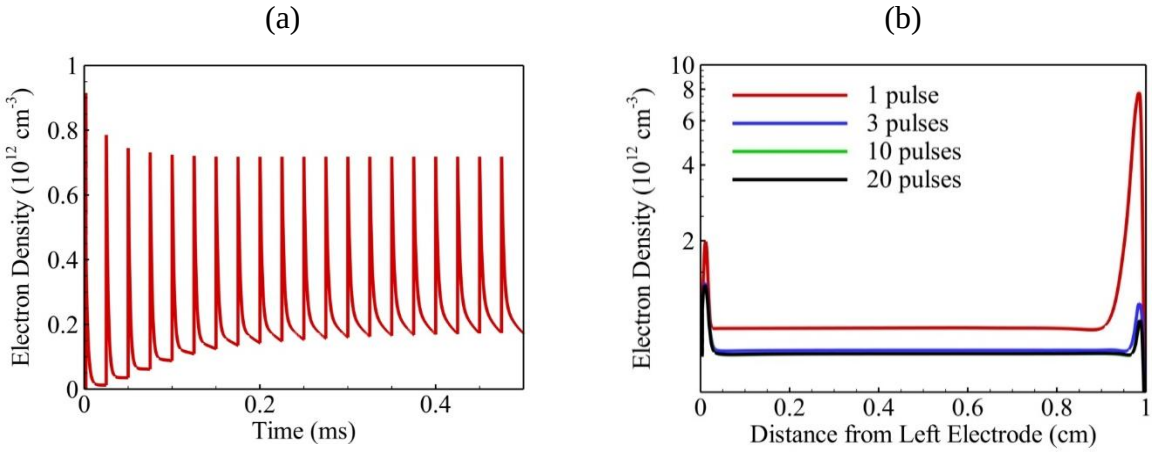

Figure 5.2: (a) Temporal evolution of electron density vs time at the center of the discharge domain, and (b) spatial distribution of electron density immediately after 1st, 3rd, 10th and 20th pulses (P_i = 114 torr, T_i = 473 K, ϕ = 1, f = 40 kHz).

The time evolution of the electron energy at the center of the physical domain is plotted in Fig. 5.3, indicating an asymptotic behavior after 8 pulses, with a peak value of approximately 6.5eV. The discharge dynamics at different pulsing frequencies is shown in Fig. 5.4. The evolution of the electron density at the center of the physical domain is

for 20, 30 and 40 kHz, respectively. The initial pressure and temperature are 114 torr and 473 K, respectively, with the equivalence ratio, ϕ = 1. In all the three cases, the electron production and decay rates reach a stationary state after a few voltage pulses. It is interesting to note that the peak value of the electron density at steady state is inversely proportional to the pulsing rate, decreasing from 9×10^{11} cm^{-3} at the 20 kHz to 8.5×10^{11} cm^{-3} at the 40 kHz pulsing rate, respectively. This behavior can be attributed to the increase in residual electron density with increase in repetition rates (i.e. smaller time available for electron-ion recombination between pulses). High residual charges result in earlier electrical breakdown during a discharge pulse, consequently leading to reduced ionization rates.

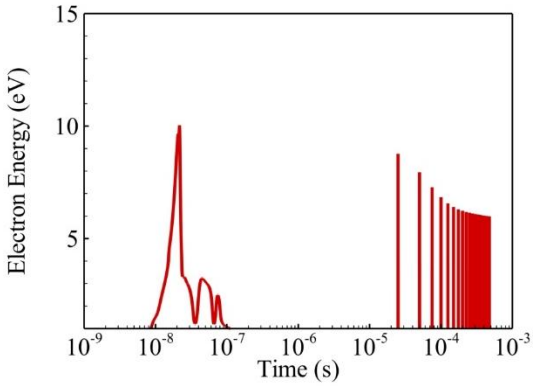

Figure 5.3: Temporal evolution of electron energy at the center of the discharge domain (P_i = 114 torr, T_i = 473 K, ϕ = 1, f = 40 kHz).

Figure 5.5 shows the temporal evolution of electron density at the center of the discharge volume at three different pressures of 54, 114 and 144 torr. The initial temperature is 473 K and the equivalence ratio is unity. The electron density exhibits a periodic behavior after a few pulses, irrespective of the pressure. The peak electron density at steady state increases with increase in pressure, from 7.5×10^{11} cm^{-3} at 54 torr to 9.5×10^{11} cm^{-3} at 144 torr, respectively. Faster recombination rates at high pressures result

in lower residual charge densities, which lead to increase in the ionization rates, and result in higher peak electron density.

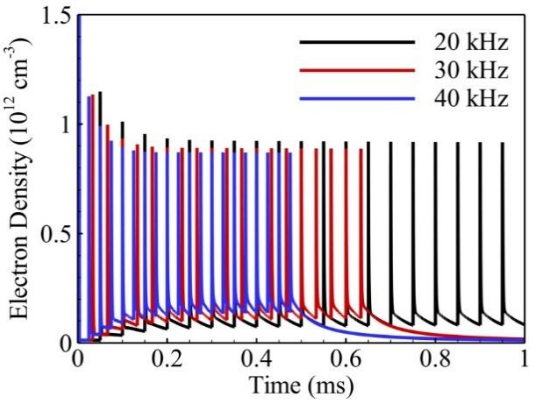

Figure 5.4: Time evolution of electron density at the center of the discharge domain for 20 pulses at 20, 30 and 40 kHz repetition rates (P_i = 114 torr, T_i = 473 K, ϕ = 1).

In summary, the NRPD reach an asymptotic regime after a few voltage pulses. The electrical characteristics such as electron production and decay rates remain unchanged in subsequent pulses. This behavior was observed at different pulsing rates and pressures. Although not shown, a similar situation occured over a wide range of H_2-air equivalence ratios as well.

5.3.2 "Frozen Electric Field" Modeling Approach

In this section, we take advantage of the periodic behavior shown previously, in order to formulate an efficient strategy to expedite simulations of NRPD. The "frozen electric field" approach consist of the following steps,

(i) At given operating conditions, a burst of a small number of pulses is simulated using the complete plasma model, with electrical properties calculated during each pulse.

(ii) The spatial information about the electron density, electron energy and electric field at the end of the pre-specified burst is stored in a look-up library.

(iii) The simulation of subsequent voltage pulses is carried out with the electrical characteristics frozen at the values in the library. The equations for the electric field, electron density and electron energy are switched off.

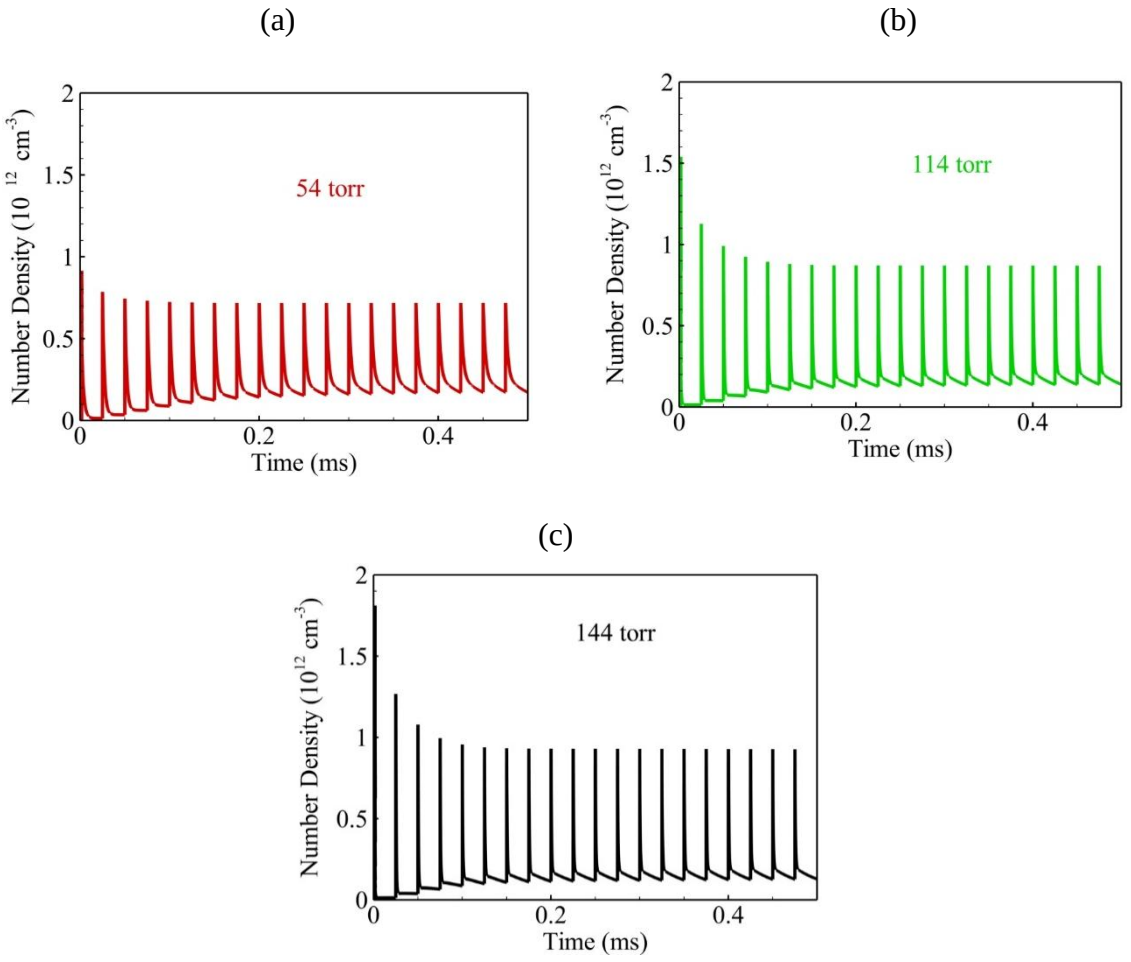

Figure 5.5: Time evolution of electron density at the center of the discharge domain for 20 pulses at (a) 54 torr, (b) 114 torr and (c) 144 torr pressures respectively. The other operating conditions are T_i = 473 K, ϕ = 1, f = 40 kHz.

As a benchmark case, we consider a burst of 50 nanosecond voltage pulses using both the complete model with the electrical properties calculated in each pulse, and the

frozen approach with electrical properties unchanged after the 10th pulse. Figure 5.6(a) shows the time evolution of the temperature and number densities of O, H, OH, and H_2O at the center of the discharge gap, predicted by the two models. The simulations are conducted at an initial condition of 144 torr, and 473 K with a pulsing frequency of 40 kHz. For all the species, the predictions from the frozen approach deviate from those of the complete model by less than 20%. Figure 5.6(b) shows the spatial distribution of the atomic oxygen density at the end of the 18th, 30th and 40th pulses. The frozen approach under-predicts the O atom density by approximately 20 % throughout the discharge gap, except for the boundary sheath regions where larger deviations (about 30 %) are observed. It must, however, be noted that the prediction error reduces with increasing pulse number. After the 40th pulse, the error in O number density predicted by the frozen approach is less than 10%.

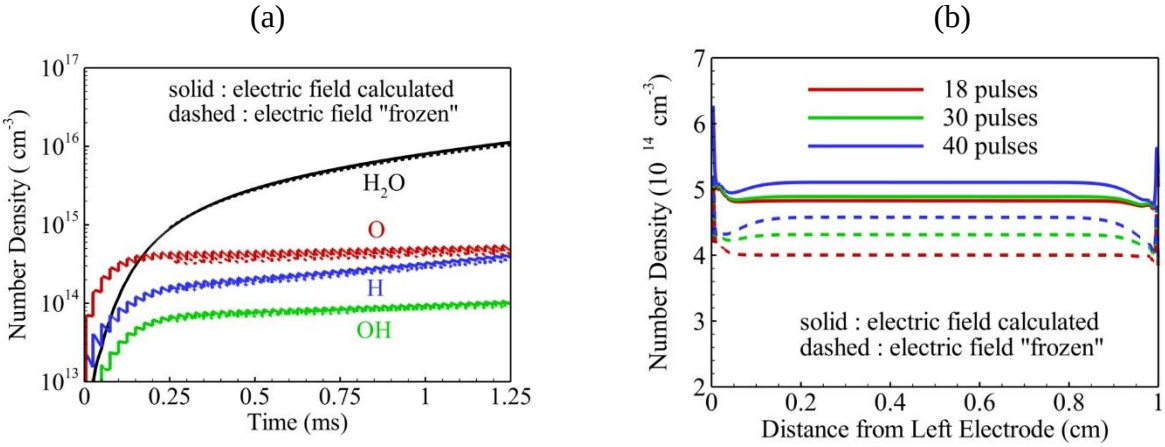

Figure 5.6: (a) Temporal evolution of O, H, OH and H_2O number densities at the center of the discharge domain. (b) Spatial distribution of O number density after 18, 30 and 40 pulses. (P_i = 144 torr, T_i = 473 K, ϕ = 1, f = 40 kHz).

Figure 5.7 shows the temporal evolution of the temperature at two different locations of x = 0.1 and 0.5 cm from the left electrode. Results from the frozen approach

agree closely with the detailed plasma model predictions, with less than 5% deviations at both locations.

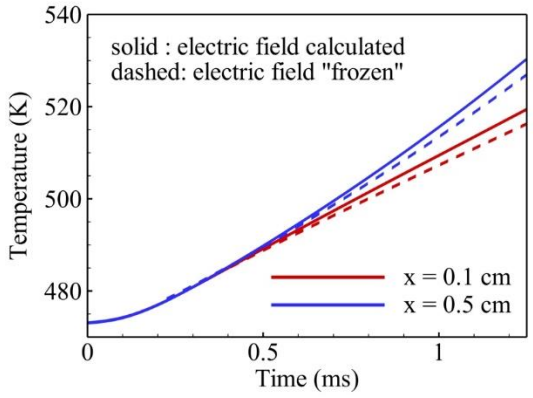

Figure 5.7: Temporal evolution of temperature at x = 0.1 and 0.5 cm locations (P_i = 144 torr, T_i = 473 K, ϕ = 1, f = 40 kHz).

The computational efficiency enhanced by the frozen approach is demonstrated in Fig. 5.8 as a function of number of pulses. The operating conditions are identical to that in Fig. 5.6(a). The simulations were conducted in parallel over 48 AMD Opteron 2.4 GHz processors connected through Infiniband Fabric switches. The complete model requires approximately 45 hours for simulating 50 discharge pulses, where the frozen approach requires only 12 hours. A major contributor to this speedup is the use of larger timesteps during each discharge pulse (10^{-9} s when the electric field is frozen as opposed to 10^{-13} - 10^{-12} s when the field is calculated). It is worth mentioning that a substantial portion of the computational time with the frozen approach is taken in simulating the first 10 pulses (approximately 1 hour per pulse, with the electric field calculated like in the complete model). In constrast, the time to simulate the dynamics of a discharge pulse when the electrical characteristics are frozen is less than 2 minutes. The savings in computational time increases rapidly with increasing number of pulses. Under the present operating

conditions, the ignition of H_2-air mixtures subjected to NRPD requires 200 - 300 voltage pulses (see the next section for details). For such large scale simulations, the frozen approach is 20 to 30 times faster than the detailed plasma model.

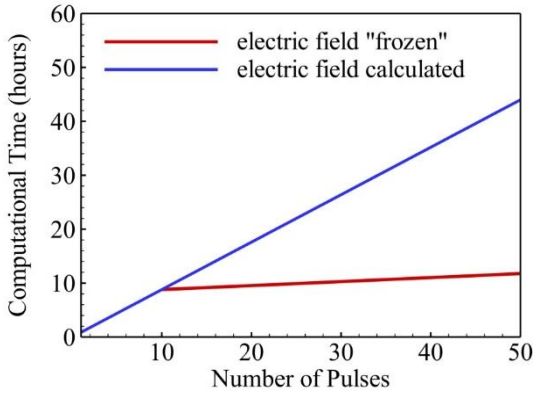

Figure 5.8: The computational time as a function of number of pulses with the electric field calculated during each pulse compared to the corresponding values with the field frozen after the 10th pulse (P_i = 114 torr, T_i = 473 K, and f = 40 kHz)

5.3.3 H_2-Air ignition characteristics

The frozen approach described in the previous section substantially improves the computational efficiency. It is thus employed to investigate the effects of pressure and eq. ratio on NRPD enhanced ignition of H_2-air mixtures. The predicted ignition delay and temperature rise are compared experimental measurements [17] to further validate the frozen modeling approach.

Figure 5.9 compares the predicted and measured temperatures at the center of the discharge volume as a function of time at the equivalence ratio of ϕ = 1. The initial conditions are 104 torr, 473 K, and pulsing frequency of 40 kHz. The frozen model results show excellent agreement with experimental data until 3 ms (120 pulses). Beyond this juncture, the temperature is over-predicted by about 20%, resulting in faster ignition compared to the measurements. In addition, the model slightly under-predicts the peak

temperature after ignition (1500 K as compared to the measured value of 1600 K). The rapid rise in temperature near the ignition point results in a dramatic reduction in the gas number density, which has a significant impact on the discharge dynamics. The validity of the frozen approach becomes questionable at this juncture, due to the fact that the "frozen" quantities correspond to the discharge development at lower temperatures. Interestingly, the overall temperature rise predicted by the frozen model deviates less than 20% from the measured data. This phenomenon can be attributed to the partial fuel oxidation triggered by the NRPD beyond a threshold temperature of ~ 700 K [28]. Subsequent application of discharge pulses has a weak effect on the temperature rise because the plasma heating is much smaller than the heat release by fuel oxidation.

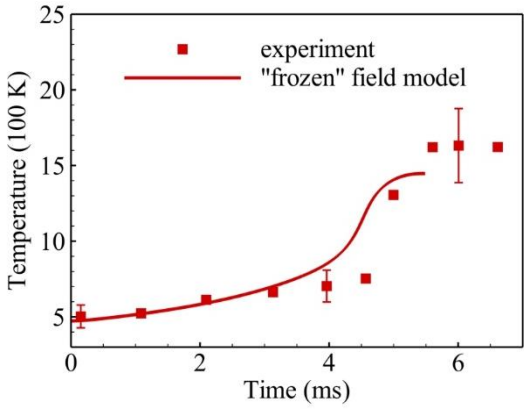

Figure 5.9: Temperature rise at the center of the discharge domain predicted by the frozen electric field model compared against the measurements from Yin et al. [17] (P_i = 114 torr, ϕ = 1.0, T_i = 473 K, and f = 40 kHz).

Figure 5.10 shows the number of discharge pulses required to ignite a stoichiometric (ϕ=1) H_2-air mixture subjected to NRPD as a function of pressure. The initial temperature is 473 K, and the pulsing frequency is 40 kHz. Ignition delay time is defined herein as the time for the temperature to rise to 1200 K at the center of the

discharge volume. The prediction errors are within 20% of the measurements for all the four pressures considered (54, 84, 114 and 144 torr).

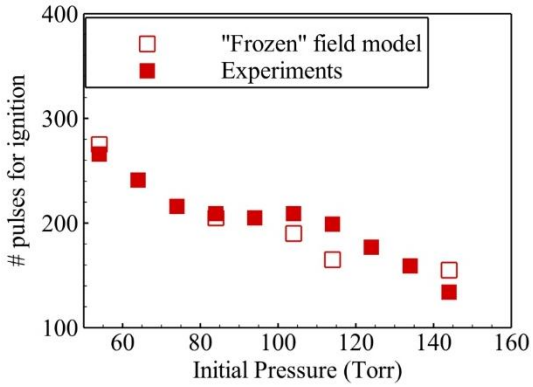

Figure 5.10: Number of discharge pulses required for ignition as a function of pressure predicted by the frozen electric field model and measurements from [17] (T_i = 473 K, ϕ = 1, and f = 40 kHz).

Figure 5.11(a) shows the time evolution of O, H, OH, and HO_2 number densities at the center of the discharge volume. Atomic oxygen is primarily produced in NRPD by quenching of N_2 by O_2, and through electron impact dissociation of oxygen molecules [21]. H atom is produced with similar kinetic pathways involving H_2 molecules. The following three-body reaction is the primary production pathway for HO_2 and is a major consumption channel of H radicals,

$$H + O_2 + M \rightarrow HO_2 \quad (5.1)$$

The rate of the above reaction increases with pressure, which explains the accumulation of HO_2 and reduction in H density with pressure in Fig 5.11(a). OH is produced at low temperatures from HO_2 through the following reactions

$$O + HO_2 \rightarrow OH + O_2 \quad (5.2)$$

$$H + HO_2 \rightarrow OH + OH \quad (5.3)$$

Higher HO_2 concentration at 114 torr results in rapid production of OH from reactions in Eqns. 2 and 3. Figure 5.11 (b) shows the time evolution of temperature at three locations

(x = 0.1, 0.3 and 0.5 cm from the left electrode) for different pressures (54, 84, and 114 torr). The temperature rises linearly with time and is independent of pressure until approximately 1 ms (40 discharge pulses). The higher OH concentration at 84 and 114 torr facilitates partial fuel oxidation and heat release from the following reaction,

$$OH + H_2 \rightarrow H + H_2O \tag{5.4}$$

After 1 ms, the temperature increases in a nonlinear fashion because of heat release from partial fuel oxidation. Finally, the conventional H_2-O_2 chain branching pathways are triggered when the temperature reaches 700 K (at 3 ms for 114 torr), followed by an exponential increase in temperature indicative of ignition. Such a temperature profile is typical of ignition of fuel-air mixtures subjected to NRPD as discussed in chapter 4. Note that the temperature rise at x = 0.3 cm closely follows the evolution at x = 0.5 cm location, suggesting simultaneous, volumetric ignition. A small time delay in the increase in temperature occurs at x = 0.1 cm because of the close proximity to the wall where heat losses are important.

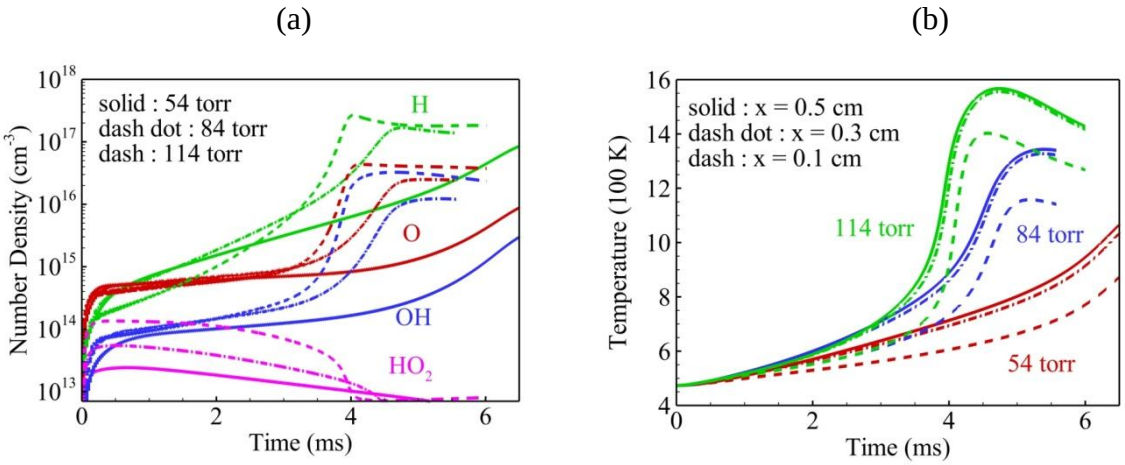

Figure 5.11: (a) Temporal evolution of (a) O, H, OH and HO_2 number densities at the center of the discharge domain, and (b) temperature rise

at x = 0.1, 0.3 and 0.5 cm locations predicted by the frozen electric field model for 54, 84 and 114 torr pressures respectively (T_i = 473 K, ϕ = 1, and f = 40 kHz).

Figure 5.12 shows that the number of pulses required for ignition is a weak function of the equivalence ratio, decreasing from 205 forϕ = 0.5 to 195 for ϕ = 1.2. In general, the frozen model predictions differs from the measurements by less than 10%. The largest deviation is seen in the case of ignition in rich mixtures (i.e. ϕ = 1.2).

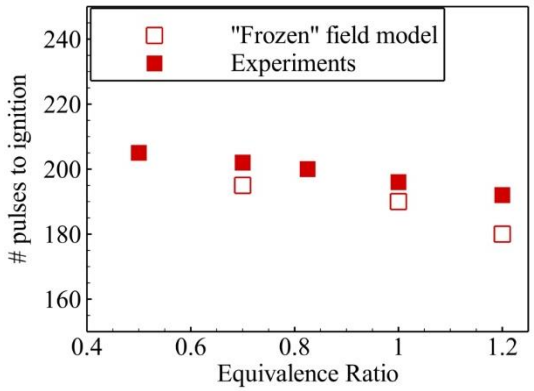

Figure 5.12: Number of discharge pulses required for ignition as a function of equivalence ratio predicted by the frozen electric field model and experimental data from [17] (P_i = 114 torr, T_i = 473 K, and f = 40 kHz)

Figure 5.13(a) shows the temporal evolution of O, H and OH densities at the center of the discharge domain for ϕ = 0.7, 1.0 and 1.2. The H concentration is sensitive to the variation in equivalence ratio. The H number density at ϕ = 1.2 is 1×10^{15} cm^{-3} (at 2 ms, after 80 pulses), almost 40% higher than the value at the same timescale for ϕ = 0.7 (7×10^{14} cm^{-3}). In contrast, the O and OH number densities are relatively insensitive to the equivalence ratio. Figure 5.13(b) shows the time evolution of temperature at three locations (x = 0.1, 0.3 and 0.5 cm from the left electrode) for different equivalence ratios (ϕ = 0.7, 1.0 and 1.2). The ignition delay time increase by approximately 20% when the equivalence ratio varies from 0.7 to 1.2. The ignition delay time at x = 0.1 cm is

approximately 10% higher than the corresponding value at the center of the discharge gap, mainly due to heat losses to the walls.

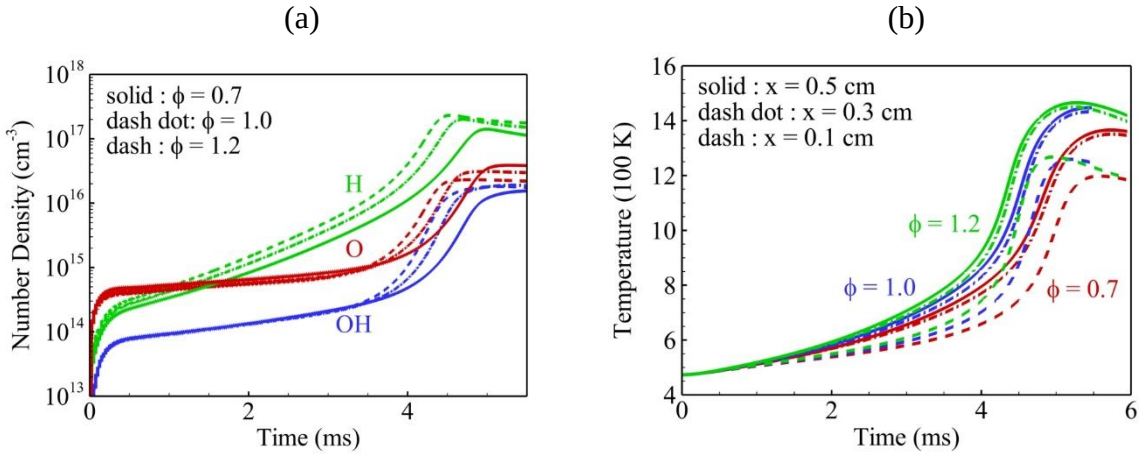

Figure 5.13: Temporal evolution of (a) O, H, and OH number densities at the center of the discharge domain, and (b) temperature rise at x = 0.1, 0.3 and 0.5 cm locations predicted by the frozen electric field model for equivalence ratios of 0.7, 1.0 and 1.2 respectively. The other operating conditions are P_i = 114 torr, T_i = 473 K, and f = 40 kHz.

5.4 Conclusions

An effective numerical strategy was proposed to expedite the simulations of nanosecond repetitively pulsed discharges (NRPD) without compromise on the solution accuracy. The "frozen electric field" modeling approach was based on the periodic nature of NRPD, wherein the electrical characteristics reached a stationary state after a few voltage pulses. The spatial distributions and temporal evolution of the electric field, electron density and electron energy were stored in a lookup library. The subsequent pulses were simulated by freezing the electrical properties to the values in the library. This allowed for the timestep size to be increased by four orders of magnitude from 10^{-13}s to 10^{-9}s. It was found that the frozen model was 5 times faster than the complete model in simulating 50 pulses, and showed a speedup of upto 30 times for large scale simulations

(200 - 300 pulses). The simulation results compared favorably with the complete plasma model predictions, and showed good agreement with the ignition delay and temperature measurements of H_2-air mixtures subjected to pulsed nanosecond dielectric barrier discharges at different pressures (54 - 144 torr), and equivalence ratios (0.7 - 1.2). The ignition delay reduced by a factor of 2 with increase in pressure from 54 to 144 torr. This was attributed to the increase in OH density with pressure which triggered a low temperature fuel oxidation process and led to rapid temperature rise and ignition. In contrast, increase in H_2-air equivalence ratio from 0.7 to 1.2 marginally decreased the ignition delay by about 20 %. This behavior was due to the insensitivity of OH production rates to the variation in the equivalence ratio.

CHAPTER 6

EFFECT OF PULSED NANOSECOND DISCHARGES ON TWO-STAGE IGNITION OF N-HEPTANE

6.1 Introduction

Owing to the complexity of plasma/chemistry interactions and lack of a reliable kinetic database, most of the previous work in this area has focused on hydrogen or small hydrocarbon fuels (C_1-C_5). Larger hydrocarbons (C_6 and above) and realistic transportation fuels, however, exhibit rich low-temperature chemistry, which is weak or completely absent in the case of small hydrocarbon fuels [17]. Motivated by this observation, the objective of this study is to numerically investigate the effect of non-equilibrium plasma on the ignition properties of n-heptane (nC_7H_{16}), which features important low-temperature chemistry and is a primary reference fuel. The kinetic and thermal effects of nanosecond pulsed discharges on the two-stage ignition process of nC_7H_{16} will be studied in detail. In addition, the chemical kinetic aspects of the plasma/chemistry interaction, including the catalytic effects of plasma-generated NO_x on the ignition process, will be examined.

6.2 Model Framework

6.2.1 Physical Configuration

Figure 6.1 shows schematically the physical configuration considered herein. Two copper electrodes are placed in a parallel plate configuration, each covered with a 1.75

mm quartz layer (dielectric constant, ε_g = 3.8). The gap between the dielectric boundaries (0.25 cm) is filled with a mixture of pre-vaporized nC_7H_{16} and dry air (79 % N_2 and 21 % O_2) at 20.3 kPa with the equivalence ratio and initial temperature in the range of 0.75-1.5 and 550-650 K, respectively. Gaussian voltage pulses (peak voltage of 20 kV and pulse duration of 40 ns) are applied at the right electrode, whereas the left electrode is grounded. The pulse repetition frequency is fixed at 60 kHz. We have shown in our previous work [11] that under this condition, one-dimensional approximation is sufficient to self-consistently simulate the nanosecond plasma dynamics and the development of the ignition kernel.

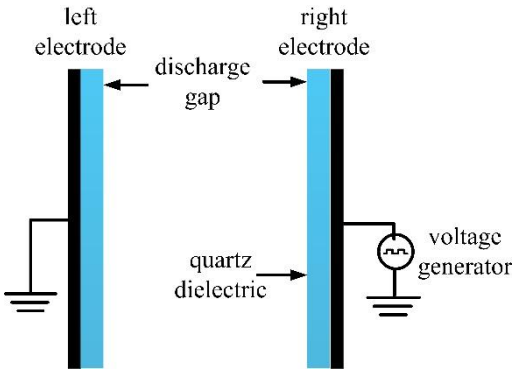

Figure 6.1 Schematic of the dielectric barrier discharge cell

6.2.2 Governing Equations

The details of the theoretical formulation and numerical model used in the present work are described in [18]. Only a brief summary is given here. Governing equations for electric potential, electron energy, and charged and neutral species continuity are considered. In addition, the conservation equations of mass, momentum and energy for the gas mixture are solved simultaneously to treat flow motion. The electron transport and reaction coefficients are expressed as functions of electron energy using BOLSIG [19] and updated at every time step through interpolation. An adaptive time-step

approach is utilized to tackle the large disparity in the timescales of the various physical phenomena of interest. Implicit time integration is performed for stiff chemical source terms, whereas species and flow transport are treated explicitly for computational efficiency. A non-uniform mesh consisting of 300 grid points, with highest resolution near the two dielectric boundaries, is used to obtain grid convergent solutions. A domain decomposition approach with MPI (message passing interface) is implemented to compute the solution in parallel over multiple processors.

The predictive capability of the numerical code has been well validated with measurements of the input electrical energy, atomic oxygen and temperature in nanosecond pulsed plasma in air [11]. In addition, the model was benchmarked against experimental data on temperature, OH and ignition delay in H_2-air mixtures subjected to pulsed nanosecond discharges [18].

6.2.3 Kinetic models of nC_7H_{16} - air plasma

In order to understand the effect of radicals generated by pulsed discharges on the low- and high-temperature chemical pathways in the ignition of nC_7H_{16}, an optimized kinetic model is developed. The scheme combines a reduced nC_7H_{16} chemical kinetic model [17, 20] fuel and air plasma reactions [21-22] and NO_x reactions [23-24]. The entire scheme consists of 166 species and 611 reactions, incorporating charged species N_2^+, O_2^+, HN_2^+, H_3O^+, $C_7H_{15}^+$, $C_6H_{13}^+$, $C_5H_{11}^+$, O_2^-, and e^-; excited species $N_2(A^3)$, $N_2(B^3)$, $N_2(C^3)$, $N_2(a^1)$, and $O(^1D)$; and neutral species. Electron impact processes (ionization, dissociation, excitation and attachment) along with quenching, detachment and recombination reactions are considered. The rate coefficients of electron-based reactions are calculated at each instant (at every spatial node) by solving the electron

Boltzmann equation with two-term expansion using the BOLSIG software [19]. For this purpose, self-consistent sets of electron impact cross-sections are used for O_2 [25] and N_2 [26]. There are, however, no cross-section data available for nC_7H_{16}. It is therefore assumed that the electron impact cross-sections for nC_7H_{16} are similar to that of C_2H_6 taken from [27]. A sensitivity analysis was conducted by varying (up to 5 times) the rate constants of electron impact and quenching reactions of nC_7H_{16}. Negligible impact on ignition delay predictions was found.

NO_x kinetics (from GRI Mech 3.0 [23]) is included in the kinetic model to study the catalytic effect of NO on ignition [4]. Plasma can efficiently generate *NO* through the following pathways [24],

$$N_2 + e \rightarrow N(^2D) + N + e \tag{6.1}$$

$$N(^2D) + O_2 \rightarrow NO + O \tag{6.2}$$

$$N_2(A^3) + O \rightarrow NO + N(^2D) \tag{6.3}$$

Takita et al. [24] and Ombrello et al. [4] demonstrated that NO can have a catalytic effect on hydrocarbon fuel ignition via reactions 4 to 7, which have also been included in the present kinetics mechanism,

$$NO + HO_2 \leftrightarrow NO_2 + OH \tag{6.4}$$

$$CH_3 + O_2 + M \leftrightarrow CH_3O_2 + M \tag{6.5}$$

$$CH_3O_2 + NO \leftrightarrow CH_3O + NO_2 \tag{6.6}$$

$$CH_3 + NO_2 \leftrightarrow CH_3O + NO \tag{6.7}$$

6.3 Results and Discussion

Application of a nanosecond voltage pulse in a mixture of nC_7H_{16} and air (equivalence ratio, ϕ = 1.0, p = 20.3 kPa, T = 600 K) causes electrical breakdown at ~5.5

kV, resulting in a surge in the current as shown in Fig. 6.2. Charge accumulation on the dielectric layers shields the plasma from further increase in applied voltage, and a rapid fall in current is observed. The E/N ratio at the center of the discharge volume is also shown as a function of time. The total input energy is found to be ~0.6 mJ per pulse. It is evident that a significant portion of the input pulse energy is coupled at E/N values greater than 100 Td, resulting in rapid electron impact dissociation, excitation and ionization of neutral species.

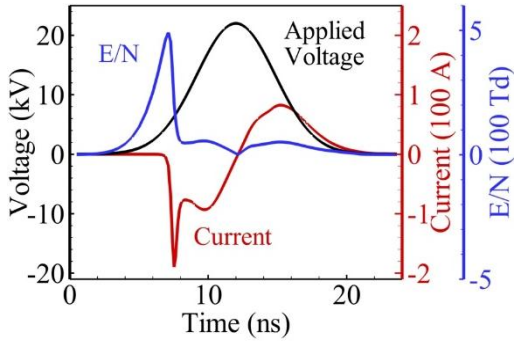

Figure 6.2 Applied voltage, current and E/N at the center of the domain as a function of time during a discharge pulse in nC_7H_{16} and air mixture (ϕ = 1.0, P = 20.3 kPa, T = 600 K).

6.3.1 Plasma Species Production

The reactive species generated by the plasma have a critical effect on the nC_7H_{16} ignition properties. Figure 6.3 shows the mole-fractions of O, H, OH and NO after a burst of 5 voltage pulses (at 0.1 ms) at 60 kHz pulsing frequency as a function of distance from the left electrode. The operating conditions are the same as in Fig. 6.2. Atomic oxygen O is predominantly produced via electron impact dissociation of O_2, and quenching of excited N_2 by O_2. Two small peaks are noticed in the spatial profile of the O atom near the boundaries, where the mole-fraction is ~2 times the value at the center. This behavior

can be attributed to higher E/N and electron densities during breakdown, near the boundary sheath edges, as compared to corresponding values in the bulk plasma region. As a result, the electron impact dissociation and excitation rates are higher near the boundaries than at the center of the discharge gap. The H atom exhibits trend similar to that of O, and is produced via electron impact dissociation and quenching reactions of nC_7H_{16}. The H mole-fraction, however, is ~5 times lower than that of O because the concentration of nC_7H_{16} (0.019 mole-fraction) is much smaller than the concentration of O_2 (0.2 mole fraction) under the present operating conditions. The relatively low temperature (600 K) favors uniform generation of HO_2 via three body reactions between H and O_2 in the discharge volume. The concentration of NO in the discharge volume is ~10 ppm after 6 pulses, and is produced by the plasma via reactions 1-3. The effect of NO on the ignition kinetics will be discussed later in more detail. OH radicals can be produced by the reaction between HO_2 and NO (Eq. 4), but are generated predominantly from the following reactions,

$$O + HO_2 \leftrightarrow OH + O_2 \tag{6.8}$$

$$H + HO_2 \leftrightarrow OH + OH \tag{6.9}$$

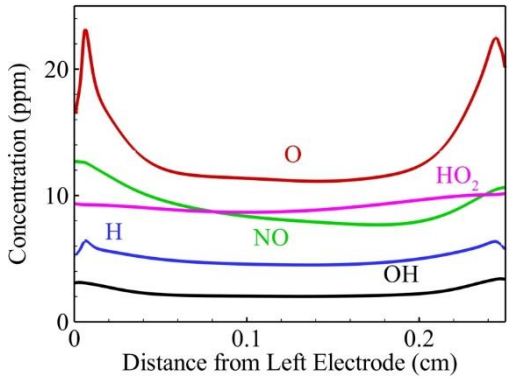

Figure 6.3 Spatial distribution of O, H, OH, NO and HO_2 concentrations after 5 discharge pulses in a n-C_7H_{16} and air mixture (ϕ = 1.0, P = 20.3 kPa, T = 600 K).

6.3.2 Effect of Plasma on Low Temperature nC_7H_{16} Chemistry

Figure 6.4 shows the temporal evolution of temperature at the center of the computational domain with and without the application of nanosecond discharge pulses. The operating conditions are the same as in Fig. 6.2. It is evident that pulsed nanosecond plasma accelerates the onset of the first-stage temperature rise (from 600 K to 800 K) nearly 10 times, from ~0.3 s (in the case of auto ignition) to ~35 ms (for 5 discharge pulses). The radicals generated by the plasma initiate the H abstraction from fuel molecules through the following and similar reactions,

$$nC_7H_{16} + OH/O/H \rightarrow n\text{-}C_7H_{15} + H_2O/OH/H_2 \quad (6.10)$$

For comparison, 2 and 8 pulses are applied to initiate the first stage of the nC_7H_{16} ignition process. It is observed that the plasma enhancement is a weak function of the number of pulses, and the difference is ~5%. This behavior can be attributed to the "self-acceleration" of the low temperature chain branching after some alkyl radicals, R, have been generated. As shown in Fig. 6.5, the alkyl radical triggers an exothermic cycle through the formation of RO_2, which isomerizes and adds another O_2 to form alkylperoxide O_2ROOH, followed by partial decomposition to smaller hydrocarbons, aldehydes and radical species such as OH and HO_2 [28-29]. These radicals further accelerate the initial H abstraction step, thereby creating a positive feedback loop. The nanosecond plasma acts as a catalyst by providing a small amount of seed radicals to initiate this "self-accelerating" process, and the quantity of radicals introduced initially is not of critical importance. A small amount of radical addition at low temperature conditions can dramatically change the time scales of low temperature kinetics.

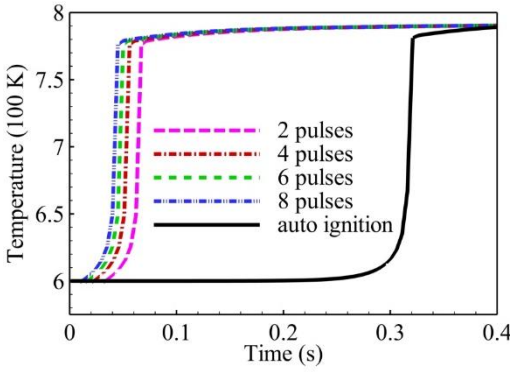

Figure 6.4: Temporal evolution of temperature at the center of the discharge gap for cases with no plasma (auto-ignition), 2, 4, 6 and 8 discharge pulses applied at the beginning of the corresponding simulations (ϕ = 1.0, P = 20.3 kPa, and T = 600 K).

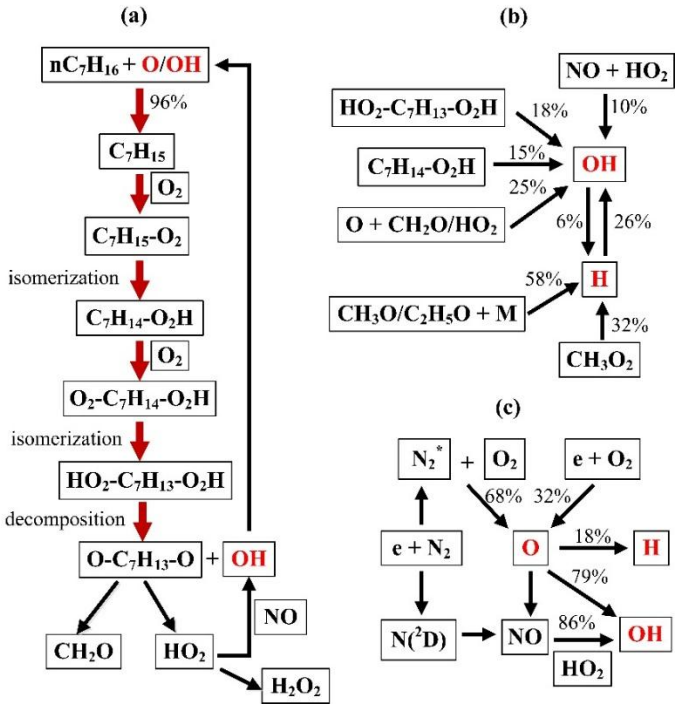

Figure 6.5: Path flux analysis describing the first stage heat release. (a) nC_7H_{16} consumption, (b) OH and H formation, and (c) O production and consumption pathways (ϕ = 1.0, P = 20.3 kPa, and T = 600 K).

Figure 6.6 shows the corresponding spatial distributions of temperature at various times after a burst of 5 pulses. The boundary conditions for the gas energy equation play

an important role in determining the temperature profiles in the discharge gap. Although the plasma radical production is higher near the electrodes (see Fig. 3), heat losses keep the temperature low and delay the initiation of the first-stage heat release close to the boundaries. The exothermic process is fastest at the center, resulting in parabolic temperature profiles up to ~20 ms. Beyond this juncture, the temperature rise at the center slows down, and heat conduction towards the boundaries flattens the temperature profile.

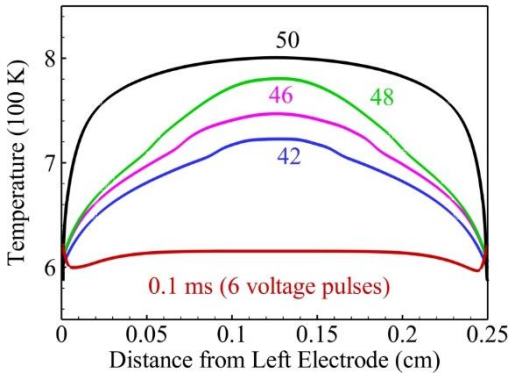

Figure 6.6: Spatial distributions of temperature at various times depicting the first-stage heat release process (ϕ = 1.0, P = 160 torr, and T = 600 K).

The ignition delay time for nC_7H_{16} comprises of the initiation time for the first-stage temperature rise and the intermediate induction period prior to the thermal explosion. The effect of the equivalence ratio on the plasma enhancement is shown in Fig. 6.7(a), which depicts the temperature rise at the center of the discharge gap as a function of time. The simulations were conducted at 600 K and 20.3 kPa with ϕ = 0.75, 1.0 and 1.5, respectively. In each case, 5 discharge pulses were applied at the beginning of the simulation. The corresponding auto-ignition curves are also shown for comparison. The plasma enhancement is identical in each case, suggesting that the addition of radicals has a strong impact on the initiation time, irrespective of the equivalence ratio. It is worth

noting that the ignition delay time is shorter for rich mixtures, with or without plasma, because of the smaller induction period after the first stage temperature rise.

Since the kinetic reaction pathways of nC_7H_{16} are highly temperature sensitive, the plasma enhancement is also studied at different initial temperature conditions. Figure 6.7(b) shows the temperature evolution at the center of the discharge gap with initial temperatures of 550, 575, 600 and 650 K, respectively. The simulations were conducted for stoichiometric nC_7H_{16} -air mixtures at 20.3 kPa. The corresponding auto-ignition curves are also shown for comparison. At 550 K, the initiation time for the first-stage temperature rise constitutes a major portion of the overall ignition delay. In this case, application of only 5 discharge pulses at the beginning reduces the ignition delay by 70%, from 4.5 to 1.5 s. With increase in initial temperature, the initiation time decreases but the induction period increases. Hence, the impact of plasma in terms of percentage reduction in the ignition delay decreases. At a higher initial temperature (above 650 K), the initiation time is negligible compared to the ignition delay. Application of nanosecond discharge pulses at the beginning has negligible impact under this condition. It is of interest to understand the effect of discharge pulses after the first-stage heat release on the induction and overall ignition delay times.

6.3.3 Effect of Plasma on Second Stage Ignition of nC_7H_{16}

A staggered application of discharge pulses is found to have the greatest effect on the overall ignition delay time at low initial temperatures (below 800 K). A few pulses (2-6) are first applied at the beginning of the event, and the high voltage pulser is then switched off. The seed radicals generated by the plasma greatly accelerate the first-stage temperature rise. At this juncture, the pulser is switched on and a larger number of

discharge pulses (10-20) are applied to further reduce the induction time of nC_7H_{16} ignition.

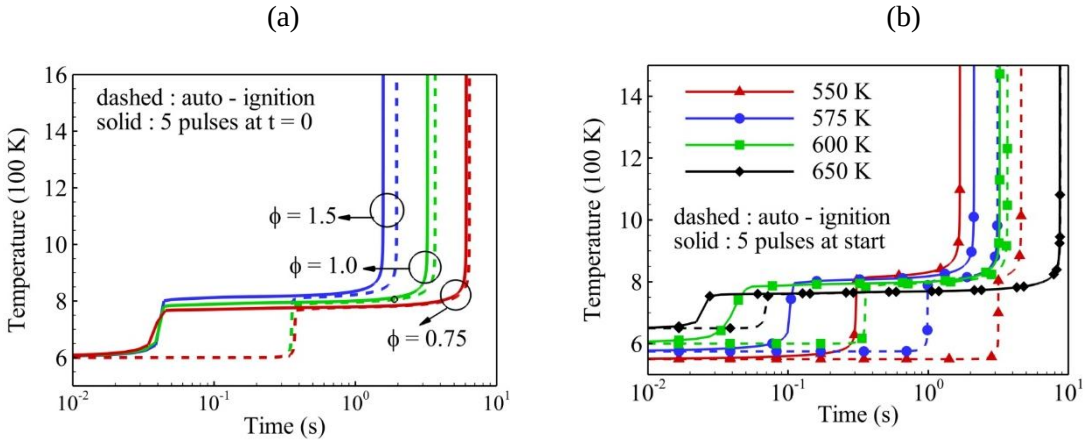

Figure 6.7: The evolution of temperature at the center of the computational domain with and without 5 discharge pulses applied at the beginning of corresponding simulations at 20.3 kPa for (a) ϕ = 0.75, 1.0 and 1.5 (600 K), and (b) for initial T = 550 K, 575 K, and 600 K (ϕ = 1.0).

Figure 6.8 shows the temperature evolution at the center of the discharge gap, demonstrating the effect of staggered application of discharge pulses on the ignition delay. All simulations were conducted for a stoichiometric nC_7H_{16}-air mixture at an initial pressure and temperature of 20.3 kPa and 600 K, and respectively. For comparison, the temperature evolution without plasma (auto ignition) and with 5 discharge pulses applied at the beginning are included in the same figure. The staggered pulsing consists of 5 pulses applied at the beginning, with the remaining pulses applied at 0.2 s after the first-stage temperature rise. Staggered application of 25 discharge pulses results in 40% reduction in the ignition delay as compared to the auto-ignition case. Reduction of the number of pulses in the staggered mode from 25 to 15 results in 15% increase in the ignition delay from 2.1 to 2.5 s. This is in contrast to the lack of sensitivity of the first-stage heat release to the number of discharge pulses in the burst (see Fig. 6.4).

Further analysis suggests that the plasma effect after the first-stage ignition is primarily thermal. A thermal heating simulation is therefore included in the results shown in Fig. 6.8. Five pulses are applied at t = 0. Thermal energy (equivalent to 20 pulses) is then provided after the first-stage ignition. This case produces an ignition delay similar to that with staggered application of 25 discharge pulses. The ignition delay is slightly shorter for the plasma case because radical production from pulsed discharges introduces more heat release. Quenching of excited species and recombination of radicals generated by the plasma result in a temperature rise of ~0.8 K/pulse. Application of 20 nanosecond pulses during the induction period gives rise to a temperature rise of ~15 K within 0.5 ms. Higher temperatures promote faster decomposition of H_2O_2 to OH radicals. It is for this reason that increasing the number of pulses (increasing the heating rate) has a direct impact on reducing the induction time.

It must be emphasized that the quantity of radicals generated by the plasma is too small to make a significant impact on combustion chemistry during the induction period in this study, because the total input plasma energy accounts for only 1.8% of the fuel heat release. The effect is thus predominantly thermal. If the production rate of radicals from each discharge pulse increases, the positive influence of plasma on the induction period after first stage ignition may be more significant as compared to thermal heating. Application of thermal energy in the same amount of plasma before the first stage temperature rise has negligible impact on the ignition delay. For example, 25 discharge pulses applied at t = 0 will result in a temperature rise of ~20 K. If the initial temperature were raised to the same level, the change in the ignition delay would be insignificant.

The importance of including low temperature NOx kinetics like reactions 4-7 is also shown in Fig. 6.8 for staggered application of 15 discharge pulses. Removing NO- and NO_2-based reactions from the chemistry mechanism results in ~10% increase in the ignition delay. As mentioned in Sec. 6.2.4, nanosecond discharge pulses generate NO through reactions 1-3, whose rates are independent of the gas temperature. An analysis of reaction pathways (see Fig. 6) suggests that under low temperature conditions, nearly 86% of NO is consumed in reaction 4 with the remaining via reaction 5, to produce OH, which significantly accelerates H abstraction reactions of fuel molecules at low temperatures. The quantity of NO generated is proportional to the number of discharge pulses (approximately 1 ppm/pulse). Application of a larger number of pulses (50-100) may increase the NO concentration and the associated low-temperature catalytic effect will be more pronounced.

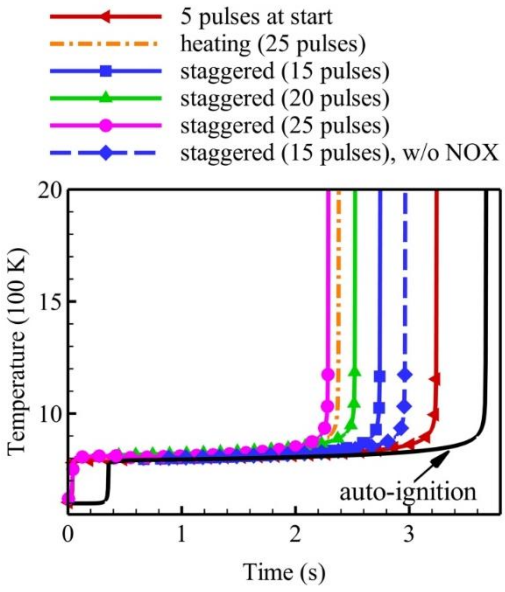

Figure 6.8: Temporal evolution of temperature at the center of the computational domain for case with no plasma (auto - ignition), 5 pulses applied at beginning, and staggered application of 15, 20 and 25 pulses respectively. An additional case without NOX kinetics is shown for staggered application of 15 pulses (ϕ = 1.0, P = 20.3 kPa, and T = 600 K).

6.4 Conclusions

The effect of non-equilibrium, nanosecond pulsed plasma discharges on the ignition characteristics of nC_7H_{16} and air was studied by means of a self-consistent numerical analysis at a reduced pressure of 20.3 kPa. The plasma generated radicals initiated and significantly accelerated the H abstraction reaction from fuel molecules and triggered a "self-accelerating" feedback loop via low-temperature kinetic pathways. Application of only a few discharge pulses at the beginning was sufficient to reduce the initiation time of the first-stage temperature rise by a factor of 10. The plasma effect on the low temperature chemistry was independent of the equivalence ratio, but became more pronounced at lower initial temperatures (550-650 K). A staggered application of discharge pulses (a few pulses at the beginning and a larger number of pulses immediately after the first-stage temperature rise) was found to be optimal, reducing the ignition delay by nearly 40%. The plasma effect after the first stage was shown to be predominantly thermal. Temperature rise, introduced by quenching of excited species, radical induced fuel oxidation and radical/ion-electron recombination, accelerated the decomposition of H_2O_2 and reduced the induction period before ignition. NO produced by plasma pulses reacted with HO_2 at low temperatures to generate OH, which accelerated the low temperature nC_7H_{16} ignition.

This work also demonstrated that non-equilibrium plasma can dramatically modify the time scales of fuel kinetics, and therefore can be used to control the ignition timing for advanced engine technologies.

CHAPTER 7

NANOSECOND PLASMA ENHANCED $H_2/O_2/N_2$ PREMIXED FLAT FLAMES

7.1 Introduction

Sun et al. [34] showed that *in situ* generated nanosecond plasma had a significant effect on ignition-extinction characteristics of $CH_4/He/O_2$ counterflow diffusion flames, replacing the conventional S-curve with a new monotonic stretched ignition curve. In general, due to the complexity of the interaction between plasma and flame kinetics, the fundamental enhancement mechanisms are poorly understood.

Recently, Li et al. [79] developed a burner platform to study the coupling between laminar, low-pressure, premixed flames and *in situ* generated nanosecond plasma discharges. The combination of diffuse plasma and a steady, laminar, quasi-one-dimensional flame in this configuration is conducive to both laser-based measurements and numerical modeling with detailed kinetic mechanisms. In the present work, we investigate the effect of pulsed nanosecond discharges on a lean (ϕ = 0.5), premixed $H_2/O_2/N_2$ flame operating at 25 torr with the burner platform described in [79]. Spatially-resolved OH and temperature measurements are performed with and without a burst of 200 discharge pulses. A self-consistent, one-dimensional numerical model, described in chapter 2, capable of resolving electric field transients over nanosecond timescales (during each discharge pulse) and radical kinetics and transport processes occurring at micro-to-millisecond timescales is used to develop insight into the complex plasma/flame interactions. A particular focus is given to understand the role of thermal vs kinetic effects of the plasma on the laminar premixed flame.

7.2 Model Framework

7.2.1 Plasma - Flame Configuration

As shown in Fig. 7.1, the configuration referred to as “direct flame coupling” (DFC) is investigated, which consists of encapsulating the “entire” combustion process (preheating, high-temperature reaction zone, and products) within the plasma discharge. The burner surface acts as the ground electrode, and the high-voltage electrode is a 12-cm-diameter Tungsten mesh (open area = 90%) located 40 mm above the burner surface, which is supported by four ceramic posts mounted to the outer portion of the McKenna burner. This location of the high-voltage electrode results in direct coupling of the plasma processes to the combustion chemistry of interest, while providing minimal disturbance to the laminar flow field.

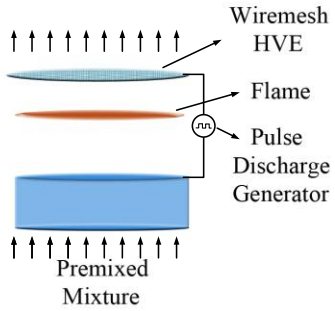

Figure 7.1 Schematic of simulation configuration for plasma enhanced premixed flame.

7.2.2 Numerical Methods

In order to obtain more insight into the multi-scale interactions between the laminar flame and nanosecond pulsed discharges, one dimensional, self-consistent simulations are performed with detailed chemistry. The details of the numerical framework are described previously in chapter 2. Briefly, equations for electric potential, electron energy, and charged and neutral species continuity are considered. In addition, continuity, momentum

and gas temperature equations are solved. The electron transport and reaction coefficients are expressed as functions of electron energy using predictions of a Boltzmann equation solver BOLSIG [17], and updated at every timestep through interpolation. The mixture-averaged formulation from CHEMKIN package [73] is used to obtain thermal conductivities and diffusion coefficients.

A non-uniform mesh consisting of 600 grid points is used to obtain grid converged solutions, with high resolution near the flame location and close to the electrodes. Temperature, velocity, and species mole fractions are specified at the inlet. Vanishing gradient boundary condition is applied for the energy equation, whereas species mole fractions are extrapolated at the outlet. Charged species fluxes include a drift component (due to electric field), and electron flux at the cathode boundary has contribution from secondary emission. Owing to the pulsed nature of the discharge process considered in this work, photoionization is not important and residual electrons from previous pulses provide seed electrons for initiation of the next pulse. The predictive capability of the present numerical code has been validated previously for pulsed nanosecond discharges in air (chapter 3) and H_2-air mixtures (chapter 4 and 5).

7.2.3 $H_2/O_2/N_2$ Plasma Flame Chemistry

A detailed kinetics mechanism consisting of 42 species and 310 reactions was compiled by combining $H_2/O_2/N_2$ plasma chemistry data [27,59] with conventional H_2-O_2 combustion kinetics [60] and NO_x kinetics [61-63]. The mechanism incorporates charged species O^+, N_2^+, O_2^+, N_4^+, O_4^+, H_2^+, H_3^+, HN_2^+, HO_2^+, H_2O^+, H_3O^+, O^-, O_2^-, and e^-, excited species $N_2(A^3\Sigma)$, $N_2(B^3\Pi)$, $N_2(C^3\Pi)$, $N_2(a'^1\Sigma)$, $N(^2D)$, $O_2(a^1\Delta)$, $O_2(b^1\Sigma)$, $O_2(c^1\Sigma)$, and $O(^1D)$; neutral species N_2, H_2, O_2, H, O, N, O_3, OH, HO_2, H_2O_2, H_2O, NO, NO_2, NH,

NNH, NH_2, NH_3, N_2O and HNO. The plasma chemistry processes pertaining to H_2O (ionization, dissociation etc.) have also been included since they are important in accurately predicting the discharge development downstream of the flame. The present model does not incorporate vibrational excitation by electron impact and vibrational energy transfer processes. Previous results [18] have demonstrated that vibrational non-equilibrium in plane-to-plane nanosecond pulse discharges in air and H_2-air is insignificant.

A simulation is performed at 25 torr with the discharge pulser switched off (no plasma) to obtain a steady-state flame solution shown in Fig. 7.2. Mole fractions of H_2, O_2 and N_2 at the inlet are 0.2327, 0.2327 and 0.5346 respectively (obtained from the experimental operating conditions). The temperature and velocity at the inlet are fixed at T_{in} = 345 K and u_{in} = 0.36 m/s respectively. Spatially-resolved OH and temperature data from the experiments, also shown in Fig. 7.2, compare well with the predictions, validating the transient flame model without the plasma. The flame solution provides initial neutral species and temperature distributions for the pulsed discharge simulations. The charged species mole fractions are initialized to 1×10^{-10}, except for electron density fraction, which is initially fixed at 6×10^{-10} to ensure charge neutrality.

7.3 Results and Discussion

The experiments make use of a high-voltage, short duration fast ionization dynistor (FID) plasma generator. Voltage and current pulse shapes during pulser operation were measured with a Tektronix P6015A high-voltage probe and Pearson (model 2877) current monitor and are shown in Fig. 7.3. The pulse width, as defined by the full width at half maximum (FWHM) value, is approximately 7 ns and the estimated pulse energy is 3

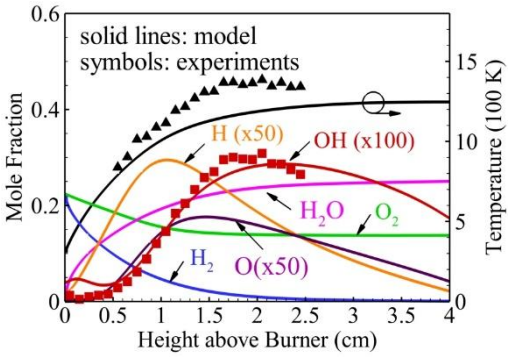

Figure 7.2 The steady-state temperature and species concentrations as a function of height above burner with discharge source switched off at 25 torr for a $H_2/O_2/N_2$ (ϕ = 0.5) flame.

mJ/pulse, which is independent of the flame conditions. We observe a delay between the voltage and the current, with the latter achieving a peak value of ~60 A, nearly 6 ns after the voltage reaches its maximum value. The corresponding curve-fit to the FID voltage waveform used in the simulations, and the calculated current are also shown in Fig. 7.3. The model is able to accurately predict the shape of the current pulse, although it under-predicts the peak value by 20%. The predicted coupled energy is 3.4 mJ per pulse, which is close to the value calculated from the voltage and current measurements.

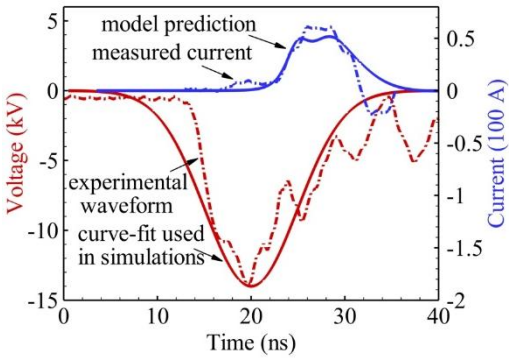

Figure 7.3 FID waveform applied at the high voltage electrode and the curve-fit used in the simulations, along with the measured and predicted current at 25 torr in a $H_2/O_2/N_2$ (ϕ = 0.5) flame.

Figure 7.4 shows the model predictions of electron number density and reduced electric field (E/N) as a function of space and time during a discharge pulse in presence of a lean, premixed $H_2/O_2/N_2$ flame. The inlet conditions and initial flame conditions (i.e., without plasma) are the same as in Fig. 3. The E/N profiles are similar to that of temperature, with lower values in the pre-heat zone because of higher number density. The E/N attains much higher values (up to 1500 Td) for a short duration near the right boundary because of the cathode sheath formation. A significant portion of the input energy is expended to electron impact ionization in the high-temperature, post-flame gases because of high E/N (700-1000 Td). Due to the lower temperatures near the burner and in the preheating zone, input energy is coupled at E/N values of 100-700 Td, resulting in efficient generation of radicals and excited species via electron impact dissociation and excitation processes, as well as quenching of excited electronic states of N_2. The electron density evolves in a spatially-uniform manner with a peak value of ~7×10^{12} cm^{-3} attained at ~21 ns.

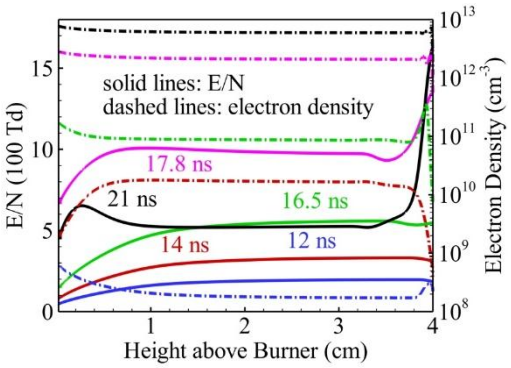

Figure 7.4 Spatial distributions of reduced electric field, E/N and electron number density during a FID voltage pulse predicted by the model at 25 torr in a $H_2/O_2/N_2$ (ϕ = 0.5) flame.

Figure 7.5(a) shows spatially-resolved OH density and temperature measurements as a function of height above the burner surface, with and without the application of 200 discharge pulses at a 40-kHz repetition rate. A significant increase in OH concentration is observed after the pulse burst, with a 40% increase in the peak mole fraction from 0.003 to 0.004 at 2 cm location above the burner. The plasma effect also results in approximately 20% rise in temperature in the burnt gas region. While the temperature rise in the preheat zone (0.5 cm to 1.5 cm above the burner surface) is similar (20%), the increase in OH mole fraction is substantially higher. For example, the OH mole fraction increases from 0.001 to 0.0025 9 mm above the burner surface, which corresponds to an increase of 140%. Larger increases are observed closer to the burner surface.

Numerical simulations were performed to gain further insight into the plasma flame interactions. A burst of 200 FID pulses applied at 40 kHz repetition rate were simulated at the same operating conditions as in the experiments. The predicted temperature and OH profiles with and without the burst of 200 pulses are also shown in Fig. 7.5(a). The inlet conditions and initial flame conditions (i.e., without plasma) are the same as in Fig. 7.2. The model performs well in predicting the OH mole fraction and temperature rise in the pre-heat zone. In the burnt-gas regions, OH concentration is over-predicted, whereas the calculated temperatures are ~10% below the measured values. However, the trend is correctly predicted in both cases, giving confidence in utilizing the model framework to investigate the plasma and flame interactions.

Figure 7.5(b) shows the spatial distribution of O and H radicals predicted by the model at various points in time during the 200 pulse simulation. A significant rise in species concentrations is observed because of the pulsed discharge processes, with peak values of

H and O increasing by approximately a factor of 4 and a factor of 6, respectively. It is interesting to note that the gradients of radical concentrations and temperature are substantially higher in the pre-heat zone from the plasma energy addition. This suggests that the plasma chemistry accelerates ignition, resulting in the species concentration profiles moving upstream by approximately 0.2 cm.

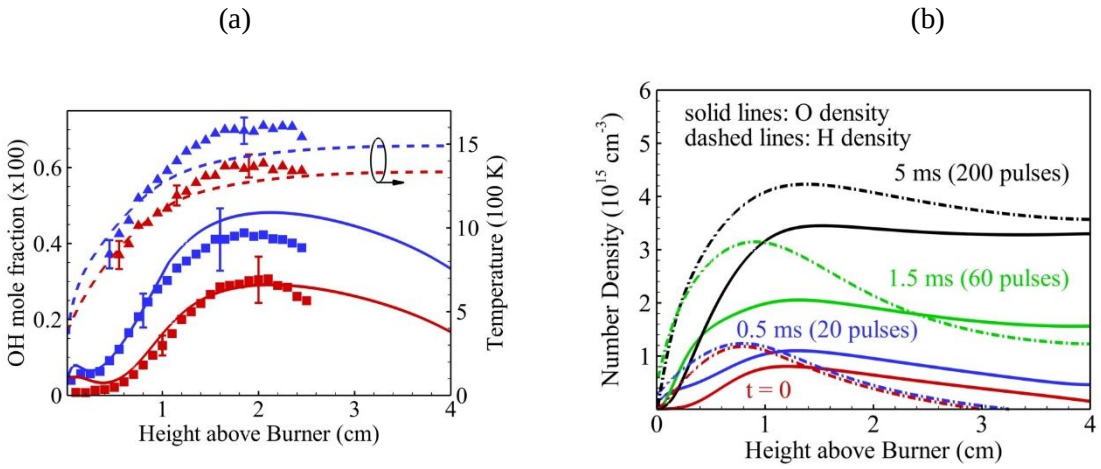

Figure 7.5 (a) Measured and predicted OH concentration and temperature, (b) predicted O and H densities as a function of height above burner before and after a burst of 200 FID pulses at 25 torr in a $H_2/O_2/N_2$ (ϕ = 0.5) flame.

Figure 7.6 shows a path flux analysis quantifying the key production pathways of O, H and OH at 0.6 cm location above the burner. A substantial fraction of O and H radicals are generated directly by dissociation of O_2 and H_2 molecules through collisions with high-energy electrons (electron impact) and excited N_2 species (dissociative quenching). On the other hand, OH is a secondary radical generated by reactions of O and H with HO_2, in addition to other chain-branching reactions. Note that OH produced by the pulsed plasma triggers heat release by reactions of OH with H_2, to generate H_2O and H. The resultant increase in temperature accelerates the conventional H_2 - O_2 chain branching

processes, thereby creating a positive feedback loop for rapid production of radicals. At locations closer to the burner, lower temperatures aid in the formation of O_3 and HO_2 from O and H radicals, respectively. Ozone is transported a short distance downstream before it decomposes to O when the temperature rises above 500 K. HO_2 persists for a longer distance until the temperature increases to about 700 K.

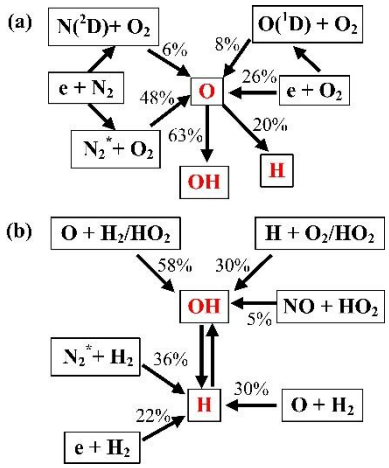

Figure 7.6 Path flux analysis describing the major formation/destruction pathways of (a) O, (b) H and OH after a burst of 200 FID pulses at 0.6 cm location above the burner at 25 torr in a $H_2/O_2/N_2$ (ϕ = 0.5) flame.

In the present configuration, the time-averaged discharge power during the burst is nearly 50% of the heat of combustion. Thus, it is not surprising that the pulsed plasma source has a significant impact on flame properties. It is, however, critical to understand if the plasma effect is predominantly thermal, or if non-equilibrium kinetics play an important role in modifying the flame structure. To determine this, we performed an additional simulation, considering only the Joule heating effect during each pulse and with the electron impact chemistry processes switched off. The Joule heating term is given by the following equation,

$$J_H = \left| e\vec{E}.(\vec{\Gamma}_+ - \vec{\Gamma}_- - \vec{\Gamma}_e) \right| \tag{7.1}$$

where $\vec{E}$ is the electric field, $\vec{\Gamma}_+$, $\vec{\Gamma}_-$, and $\vec{\Gamma}_e$ are the fluxes of positive ions, negative ions, and electrons, respectively, and *e* the electron charge. This quantity was calculated as a function of space and time from electric field and flux data predicted by the pulsed discharge simulation in Fig. 7.4. J_H is used as a source term in the gas temperature equation, while all electron impact processes during the discharge pulses are turned off. Figure 7.7 shows spatial distributions of temperature as well as O, H, and OH number densities after a burst of 200 discharge pulses with and without incorporating electron impact kinetics (in the latter case, only Joule heating is incorporated). The peak values of O and H densities decrease by nearly 30% when the non-equilibrium electron chemistry effects are not taken into account in the model. As seen in Fig. 6, adding pulsed plasma results in O and H densities increase by a factor of 4 and 6, respectively. We can therefore conclude that Joule heating is responsible for a significant fraction of the plasma enhancement of the flame. Non-equilibrium chemistry effects, however, are of critical importance in the lower-temperature regions upstream of the flame. It is evident that species and temperature gradients are less steep when only Joule heating effect is considered. Also, adding all discharge energy in form of heat results in 20% lower temperature compared with the case considering non-equilibrium chemistry effects. The difference in temperature can be attributed to the heat release triggered by partial oxidation of fuel molecules by the plasma-generated radicals. Joule heating alone cannot move the temperature and species profiles as far upstream (i.e. closer to the burner surface) as the pulsed plasma source of the same total power.

Future work will focus on techniques to increase the energy coupled in the pre-heat zone through the use of upstream plasma configuration [79], and understanding the plasma and premixed flame interactions for hydrocarbon fuels.

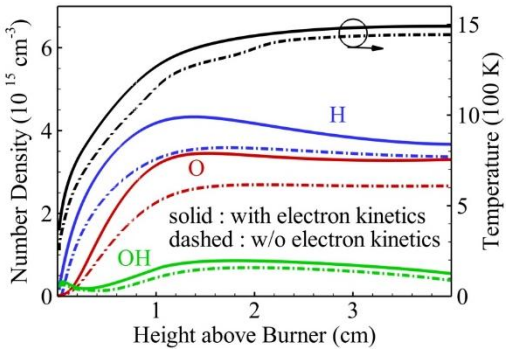

Figure 7.7 Predicted O, H, OH densities and temperature as a function of height above burner after a burst of 200 FID pulses with and without considering electron impact kinetics in the model at 25 torr in a $H_2/O_2/N_2$ (ϕ = 0.5) flame.

7.4 Conclusions

A novel plasma-flame modeling framework has been developed to study the direct coupling of steady, laminar, low-pressure, premixed flames to highly non-equilibrium, nanosecond-pulsed plasma discharges. A one-dimensional, multi-scale, pulsed discharge modeling framework with detailed plasma combustion kinetics was used to develop insight into the complex plasma- flame interactions. OH LIF diagnostics was used to measure temperature and quantitative OH mole fraction profiles, with high spatial resolution. The measurements were performed with and without a burst of 200 nanosecond discharge pulses to quantify the effect of non-equilibrium plasma on a pre-existing lean premixed $H_2/O_2/N_2$ (ϕ = 0.5) flame. Temperature increased by approximately 20% at all spatial locations and OH mole fraction increased by 100-500 % in the preheat region and 40% in the post-flame gases due to the application of discharge

pulses. Simulation results showed a significant increase in O and H densities due to plasma chemistry, with peak values increasing by a factor of 6 and a factor of 4, respectively. Additional simulations were conducted considering only Joule heating, to compare the thermal effect vs kinetic (plasma chemistry) effect. Joule heating was found responsible for a significant fraction of the plasma enhancement of the combustion processes, although electron impact processes were shown to play an important role in radical production and heat release in the pre-heat zone. It was demonstrated that Joule heating alone cannot move the temperature and species profiles as far upstream (i.e. closer to the burner surface) as the pulsed plasma source of the same total power.

CHAPTER 8

NANOSECOND PLASMA ENHANCED IGNITION OF TRANSVERSE H_2 JETS INJECTED INTO SUPERSONIC O_2 CROSSFLOW

8.1 Introduction

High speed air-breathing propulsion systems such as ramjets and scramjets suffer from problems with fuel and air mixing, ignition, and flame stabilization due to flow residence timescales being of same order as chemical kinetics timescales [3]. Creating regions of lower speed flow and recirculation through modifications in geometry such as addition of cavities [4, 80], or using ramp injectors [81], help somewhat mitigate the characteristic time disparity, but lead to significant pressures losses and difficulties in thermal management. Consequently, exploration of new methods to enhance ignition, and flame stabilization have attracted much attention.

Among the various injector designs for high speed combustion, a transverse fuel jet injected through a wall orifice offers a simple but effective solution for rapid fuel-air mixing and efficient flameholding [83]. Although this configuration is simple to realize, the generated flow structures are complicated, as shown in Fig. 8.1. A large bow shock appears ahead of the injector due to expansion of wall jet, effectively blocking the supersonic crossflow. The bow shock - boundary layer interaction results in flow separation, and creation of a subsonic recirculation region where efficient fuel-air mixing, ignition and subsequent flame holding occurs. Four types of coherent structures, the shear layer vortices, the streamwise counter-rotating vortex pairs, the horseshoe vortex, and the

wake vortices have been identified to play important roles in enhancing mixing characteristics of jet into crossflow (JICF) interactions [4].

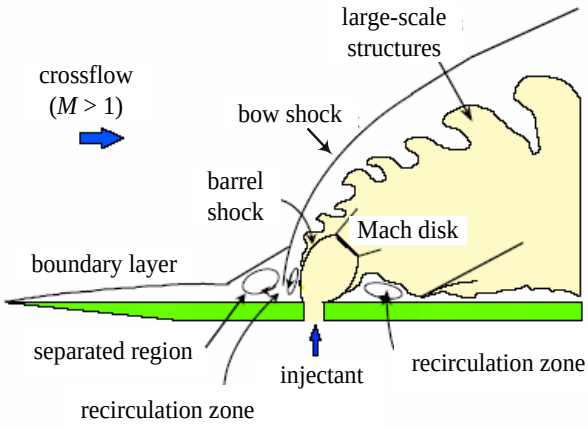

Figure 8.1. Schematics of the flowfield for a jet injected into a supersonic crossflow [4].

In order to enhance the ignition of H_2 injected into supersonic O_2 crossflow without any geometrical features, Do et al. [43] developed a novel dual fuel injection configuration, with a nanosecond, nonequilibrium plasma source located on a flat plate between an upstream oblique subsonic fuel injector, and a transverse primary fuel injector downstream. The oblique upstream jet was used to seed the hot boundary layer with fuel, which was subsequently ignited by the discharge, and serving as a pilot heat and radical source for combustion of the primary transverse jet downstream. OH PLIF data suggested a weak fragmented and detached flame when both jets were used without the discharge. With the nonequilibrium discharge, the flame appeared significantly enhanced and closer to the surface. The authors performed a simple kinetic analysis to show that rather small concentration of O and H radicals (10^{-5} mole-fraction) generated by the discharge is sufficient to partially ignite the fuel injected upstream. This process resulted in rapid rise in radical concentration (upto 10^{-2} mole-fraction) downstream of the

discharge, leading to enhanced ignition of the primary transverse fuel jet. However, lack of quantitative experimental data, especially of the role played by complex flow structures in fuel – air mixing and ignition, prevented further analysis. Recent advances in computational software and hardware make numerical approaches an attractive alternative to experiments to gain insight into role played by plasma chemical pathways and unsteady flow structures in the JICF configuration with nanosecond discharge source.

In the present study, three dimensional Large Eddy Simulations (LES) are performed using a high-fidelity compressible flow solver to investigate the complex, unsteady reacting flow-field of H_2 jets injected into supersonic O_2 crossflow. A physics-based, nonequilibrium plasma model is loosely coupled with the LES flow solver to treat the plasma-flow interactions.

8.2 Theoretical Framework

8.2.1 Physical Configuration

The front view of the physical configuration of concern consisting of two fuel injectors is shown in Fig. 8.2. It closely matches the flat plate experimental setup used in Do et al. [43].

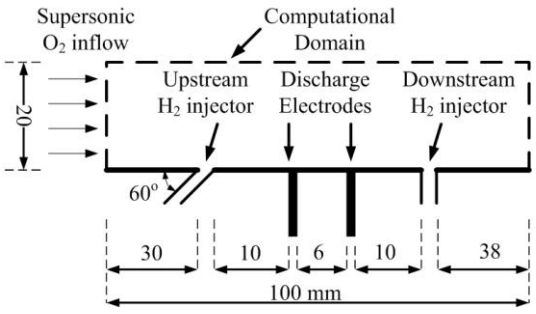

Figure 8.2. Front view of the jet in crossflow configuration used in present study, same as experimental setup in [43].

The computational domain consists of a duct of length 100 mm, breadth 20 mm and width 20 mm. H_2 gas is injected into the domain through two 2 mm diameter circular injectors. The upstream injector introduces the fuel at an angle of 60° to the axial direction. The second injector introduces fuel normal to the axis of the flat plate, and is located 26 mm downstream of the angled injector. Two copper electrodes of thickness 1 mm are flush mounted into the flat plate. The electrodes are separated by 6 mm, with the left electrode placed 10 mm downstream of the angled injector. The electrodes are connected to a high voltage generator capable of producing pulses of upto 15 kV peak voltage, and 30 ns duration at a repetition rate of 100 kHz.

8.2.2 Inlet Flow Conditions

The inlet flow conditions for this numerical study have been summarized in Table 8.1. The jet momentum ratio, J_n is defined by the following equation [43],

$$J_n = \sin\theta \frac{(\rho u^2)_{jet}}{(\rho u^2)_\infty} = \sin\theta \frac{(\gamma \mathrm{PM}^2)_{jet}}{(\gamma \mathrm{PM}^2)_\infty} \tag{8.1}$$

where, J_n is the ratio of the normal component of the jet momentum flux to the freestream momentum flux, respectively. θ, ρ, u, γ, p, and M are jet injection angle, density, velocity, ratio of specific heats, pressure and Mach number of the jet (subscript *jet*) and freestream (subscript ∞) flow. The J_n of the oblique (θ = 60°) upstream jet and the transverse (θ = 90°) downstream jet are approximately 3.5 and 9.5, respectively.

8.2.3 Computational Grid

Under present operating conditions, the Reynolds number of the transverse hydrogen jet is $Re_D = 2.5\times10^5$ for the inlet conditions provided in Table 8.1, for injector

diameter of 2 mm. Using Re_D as reference, the Taylor microscale can be calculated as λ_T = 6.7 μm. In order to ensure the LES filter width is close to the Talyor microscale, we generated a grid system consisting of 40 million grid points divided into 768 blocks. The mesh points are clustered near the plate walls to accurately resolve the fine turbulent structures. The grid is also refined near the fuel inlets to capture the jet breakdown in the injector near field. The smallest length scale near the wall is 32 μm, and the finest resolution near the injectors is 60 μm.

Freestream Conditions (O_2 crossflow)	Mach Number	2.1
	Stagnation Enthalpy (MJ/kg)	1.0
	Static Pressure (kPa)	16.0
	Static Temperature (K)	1250
	Mean Flow Velocity (m/s)	1380
Fuel Inlet Conditions (H_2 upstream injector)	Jet momentum ratio	3.5
	Mach Number	0.8
	Static Temperature (K)	300
	Ratio of specific heats	1.4
	Inflow angle	30°
Fuel Inlet Conditions (H_2 downstream injector)	Jet momentum ratio	9.5
	Mach Number	1.0
	Static Temperature (K)	300
	Ratio of specific heats	1.4
	Inflow angle	90°

Table 8.1 Inlet flow conditions for the supersonic O_2 crossflow and the two H_2 fuel injectors.

8.2.4 Boundary Conditions

Supersonic inflow boundary conditions are specified for O_2 crossflow injet. Subsonic and sonic inflow conditions are specified at the upstream and downstream H_2 fuel injector locations respectively. Viscous wall boundary conditions with zero normal velocity are enforced for the bottom wall region. For all other boundaries, supersonic outflow conditions are specified to prevent spurious reflections of shocks etc.

8.2.5 Numerical Methods

The Favre average filtered mass, momentum, energy and species equations are solved to account for the variable density effects. The conservation equations are solved using a central and upwind hybrid spatial discretization scheme to accurately capture shock discontinuities and turbulent structures [83] simultaneously. The algebraic Smagorinksy model is used to calculate the sub grid scale terms to achieve turbulence closure within the LES framework. The details of the numerical framework and validation studies are provided in [83].

8.2.6 Reduced Order Plasma Model

Emission images of nanosecond discharge [18] in the current configuration indicate that the plasma filament is produced in form of a narrow rod like structure close to the wall, and stretch uniformly from one electrode to another. In order to alleviate the computational burden in simulating the complex plasma discharge JICF interactions, we propose to use a simplified discharge model loosely coupled with the LES based flow solver. A narrow cuboidal region of 6 mm length, 2 mm width, 2mm breadth is assumed to the discharge domain in the current configuration. We fix the E/N (ratio of electric field and number density) at 300 Td (where 1 Td = 10^{-17} V/cm^2), and the electron density is fixed at n_e = 10^{14} cm^{-3}. Both quantities are assumed to be uniform in the entire discharge domain. The E/N and n_e values are chosen such that the total coupled energy per voltage pulse of 3 mJ, calculated from the voltage and current trace measurements provided in Do et al. [43]. The pulse repetition frequency is fixed at 100 kHz.

8.2.7 H_2-O_2 Plasma Combustion Chemistry Mechanism

In order to alleviate the computational burden, we make use of an optimized H_2-O_2 plasma combustion chemistry mechanism consisting of 9 species and 78 reactions. The kinetics scheme includes H_2, O_2, H_2O, HO_2, H_2O_2, O, H, OH and $O(^1D)$. The electron based reaction rates are calculated using a pre-generated BOLSIG [17] library as a function of E/N. Electron impact dissociation reactions of H_2 to give H, and dissociation of O_2 to give O and $O(^1D)$ are considered.

8.3 Results and Discussion

The primary goal of this study is to accurately simulate the complex unsteady flow structures and how they interact and transport the plasma generated radicals from the discharge domain to the core combustion region downstream where primary H_2 transverse jet is injected into the supersonic crossflow. Two sets of simulations were conducted with and without the pulsed discharges. The operating conditions in each case are identical and given in Table 8.1.

8.3.1 Flow Dynamics and Combustion of H_2 jets in supersonic O_2 crossflow

Figure 8.3 (a), (b) and (c) show the spatial distribution of Mach number, U_x and U_z velocities respectively along a x-z slice with y = 15 mm (center plane). The quantities are plotted 45 μs after the beginning of the simulation. The effect of two H_2 jets penetrating into the O_2 crossflow can be clearly seen in Fig. 8.3(a). Three distinct bow shocks can be noticed, corresponding to the flow obstruction due the boundary layer at the inlet, and due to the two jets respectively. The upstream jet is injected at an angle of 60º to the vertical axis and at a Mach number of 0.8. On the other hand, the downstream jet is transversely injected at sonic velocity. Due to the differences in inlet conditions, the flow structures from the penetration of the jets are different.

In general, as the jet penetrates the crossflow boundary layers, typical JICF coherent structures tend to appear. Since the jet has a larger pressure than the environment it enters, it soon expands far enough to reduce the exit pressure to that of its surroundings. A Prandtl-Meyer expansion fan emanates immediately at the jet exit, creating a region with decreasing pressure and flow slowdown. As the jet passes the expansion fan, it develops a supersonic core which cannot sense the information at the outer area; therefore, the jet over-expands and the pressure of the surrounding flow pushes the jet back toward its axis, leading to the formation of a converging conical shock called the barrel shock. Note that the barrel shock has a strong effect in slowing down the flow and $|u|$ drops sharply as the flow passes through it. Since the pressure mismatch between the jet and the crossflow is large, the barrel shock reflects at the perimeter of a Mach disk - a strong shock normal to the flow direction.

The jet acts as a blockage to the crossflow and retards the incoming flow ahead of it, leading to the formation of a primary shock wave - the bow shock and the separation of the boundary layer. Due to the subsequent thickening of the boundary layer, a weak λ-structure shock is also created in the lower region close to the wall. Two vortex structures are formed ahead of the jet, as seen in Fig. 8.3 (b) and (c). The larger one is centered at with a long and narrow clockwise recirculating zone; the smaller one is counterclockwise rotating and is located in the immediate-outer region of the expansion wave. The first is created by the separation of the crossflow boundary layer, and the latter is due to the roll-up of the jet shear layer. These recirculation regions resemble those in the subsonic case and were also observed in the experimental work of Santiago et al. [84] and the numerical simulation of Génin and Menon [85]. Notice that the low-speed and high-temperature

region downstream of the jets plays a significant role in the ignition and stabilization of supersonic combustion.

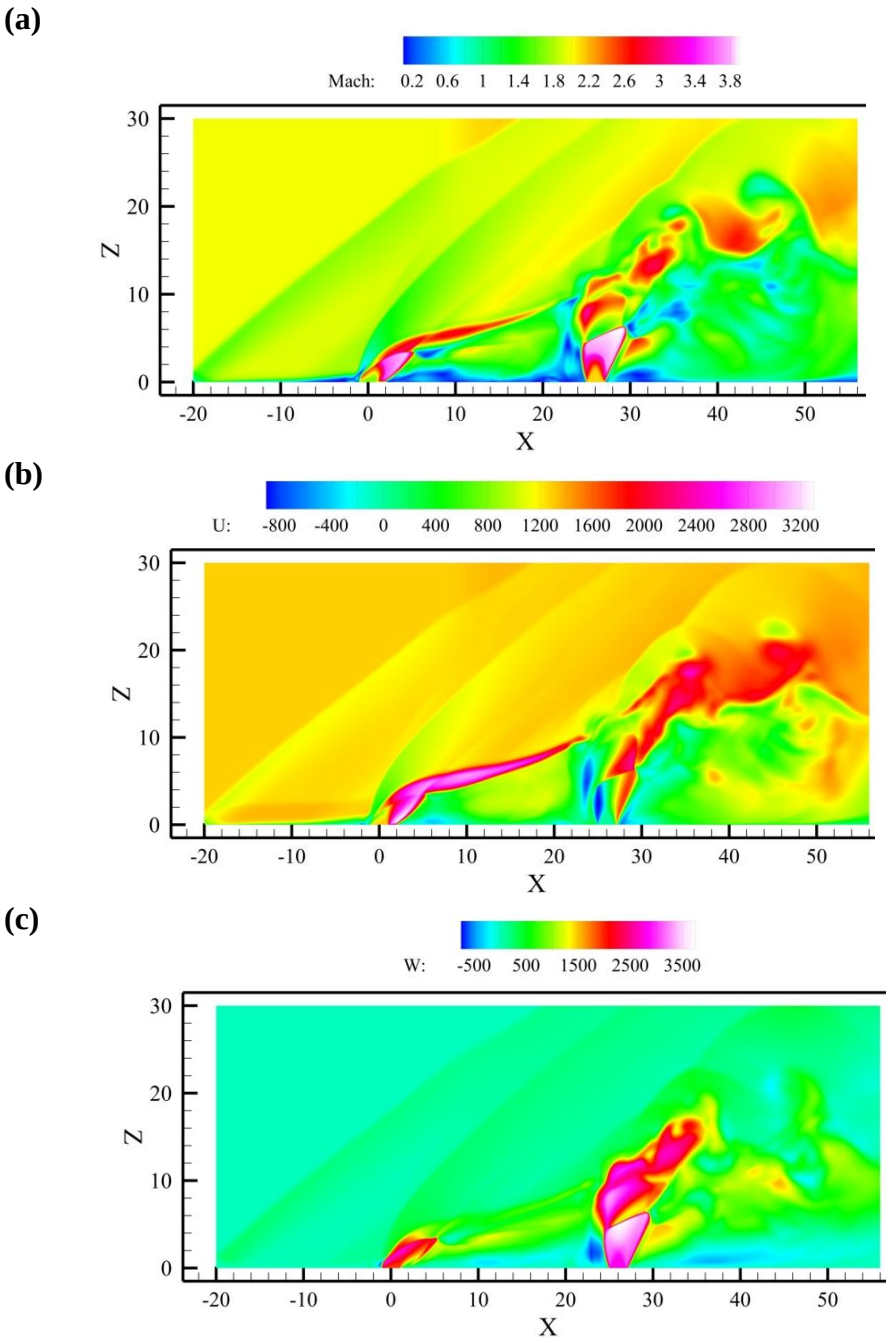

Figure 8.3: Spatial distributions of (a) Mach Number, (b) U, and (c) W velocities at y = 15 mm plane, at 45 μs from the beginning of the simulation.

Figure 8.4(a) shows the spatial distribution of temperature at y = 15 mm plane at 45 μs from the beginning of the simulation. The inlet static temperature of the O_2 crossflow is 1250 K, whereas H_2 fuel is injected at 300 K from the two injectors. The high temperature regions correspond to the strong shock at the inlet, as well as close to the bow shocks formed due to jet blockage of the crossflow. In addition, higher temperatures are observed near the wall, close to the injectors where the boundary layer is separated and a strong recirculation region exists. The angled jet plays an important role in creating a large high-temperature, recirculation region downstream which merges with a similar flow field created by the transverse jet. In effect a large low-speed, high temperature region is created between the axial locations of 5 and 20 mm from the origin. This plays a critical role in ignition and flame-holding in this configuration. The mixing of the cold fuel with the hot crossflow is evident downstream of the two jets. The shear layer instabilities of the transverse fuel jet create large vertical structures which enhance the mixing process between the cold fuel and hot oxidizer streams. Fig 8.4(b) show the temperature distribution on the y-z plane at x = 0, 25 and 50 mm locations. The expansion of the mixing region as fuel moves downstream is clearly seen.

The spatial distribution of fuel mass fraction is shown in Fig. 8.5(a) and (b). As earlier, Fig. 8.5(a) is a slice at y = 15 mm location. Most of the mixing occurs downstream of the transverse jet beyond the axial location of x = 30 mm. No shear layer instabilities are observed in the case of the upstream jet. We believe this is caused by the artificial viscosity used in the present numerical formulation to obtain stable solutions near regions with sharp gradients such as shocks. The fine-scale turbulent structures are damped by the artificial viscosity term as they pass through the bow shock, and hence the

mixing of the jet with the crossflow is under-predicted. Improvements in our numerical formulation is a work in progress. Fig. 8.5(b) shows three slices at x = 0, 25 and 50 mm locations from the origin. It is evident that mixing occurs in the y direction downstream of the transverse jet. As observed by numerous authors [80-83], effective mixing of the fuel stream with the oxidizer flow is the critical step in ignition and combustion in supersonic conditions. It can be observed that very small fraction of fuel has mixed upstream of the second injector. Penetration of the fuel upstream of the transverse injector is essential for ignition and flame-holding in the present configuration.

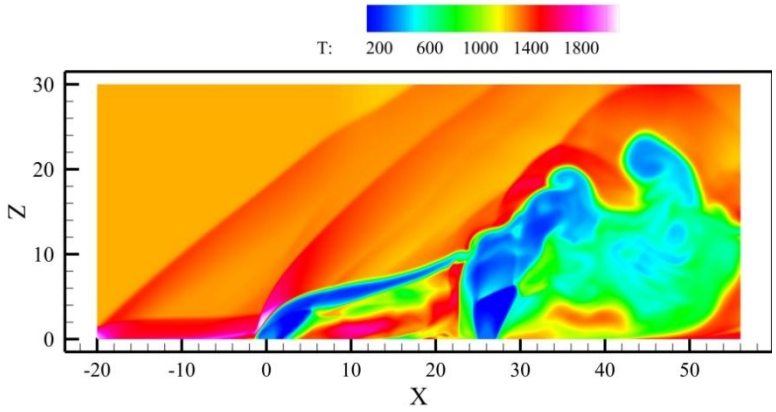

(a)

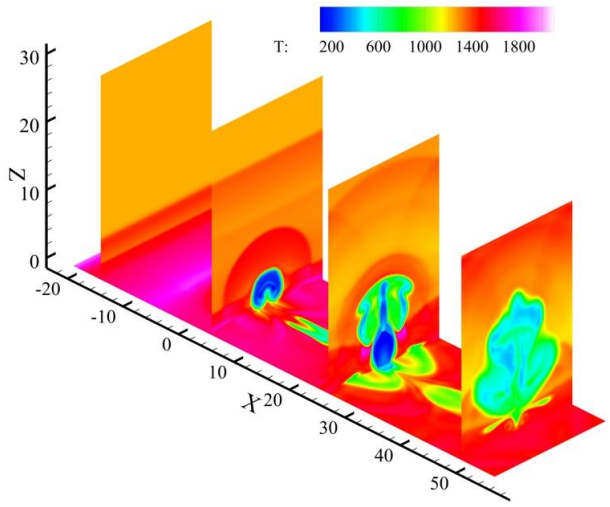

(b)

Figure 8.4: Spatial distributions of temperature at (a) y = 15 mm plane (b) x = 0, 25 and 50 mm locations, obtained at 45 μs from the beginning of the simulation.

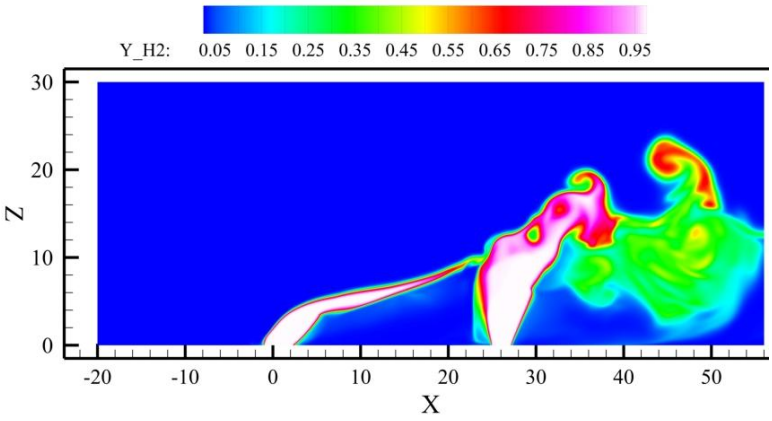

(a)

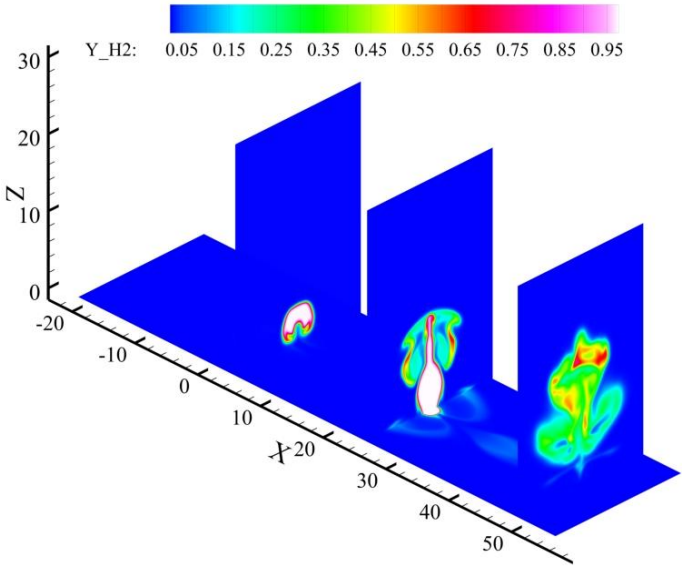

(b)

Figure 8.5: Spatial distributions of H_2 mass fraction at (a) y = 15 mm plane (b) x = 0, 25 and 50 mm locations, obtained at 45 μs from the beginning of the simulation.

Figure 8.6 shows the distribution of O_2 mass fraction in the x-z plane at y = 15 mm location. The mixing features are similar to those observed in case of H_2 mass fraction in Fig. 8.4(a). It is evident that hardly any mixing occurs upstream of the transverse injector. This behavior has a significant effect on the H_2O distribution as shown in Fig. 8.7. Prominent water concentration is observed in the recirculation zones just behind the two jets. The H_2O mass fraction downstream of the transverse injector

remains less than 0.1 suggesting that temperatures and fuel penetration downstream are low. Note that the flame kernel created by ignition upstream of the transverse jet is unable to spread downstream because of the high jet momentum (J_n = 9.5 for the present case). Essentially the cold fuel jet strongly penetrates the crossflow and blows off any flame trying to move downstream. Alternately, operating at a lower jet momentum ratio may provide more effective flameholding. It can be observed in Fig. 8.7(b) that the oxidation of fuel is higher near the boundary layers compared to the freestream region. This is because of higher temperature and low-speeds which aid in better mixing and combustion.

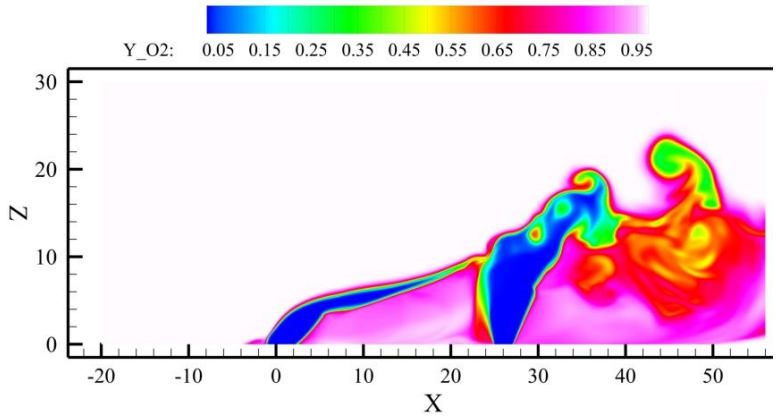

Figure 8.6: Spatial distributions of O_2 mass fraction at y = 15 mm plane obtained at 45 μs from the beginning of the simulation.

In order to obtain deeper insight into the ignition and combustion processes, Fig. 8.8 shows the spatial distribution of H and OH radicals in the x-z plane at y = 15 mm location. H is formed close to the fuel jets and downstream where the H_2 concentrations are higher. The maximum H mass fractions are seen just behind the transverse jet where high H_2O concentrations are also observed. The OH mass fractions shown in Fig. 8.8(b) are high in the ignition kernel as well as in the high temperature zone immediately

downstream the first injector. This is produced by the reaction between O_2 and fuel penetrated from the injector upstream.

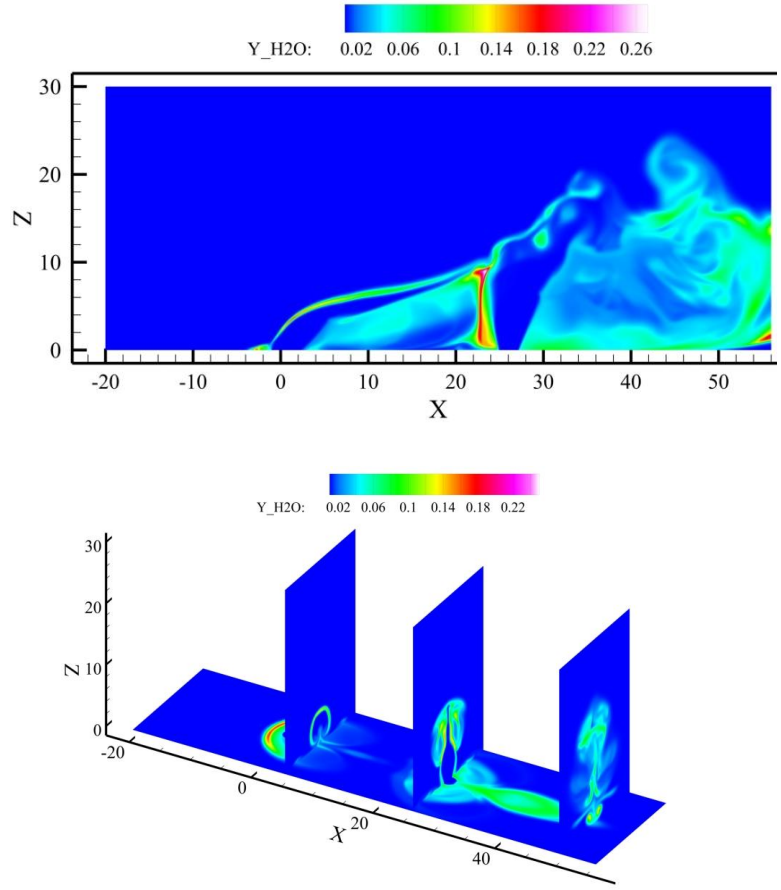

(a)

(b)

Figure 8.7: Spatial distributions of H_2O mass fraction at (a) y = 15 mm plane (b) x = 0, 25 and 50 mm locations, obtained at 45 µs from the beginning of the simulation.

Figure 8.9(a) and (b) show the mass fractions of HO_2 and H_2O_2 in the x-z plane at y = 15 mm location. HO2 is formed predominantly at the interface region where the fuel jet meets the oxidizer flow. The maximum HO_2 concentration of approximately 6.5×10^{-4} is observed inside the vortices generated by the rolling up of the shear layer downstream of the second jet. H_2O_2 is observed as a precursor to ignition, and found near regions where H_2O concentrations are high.

(a)

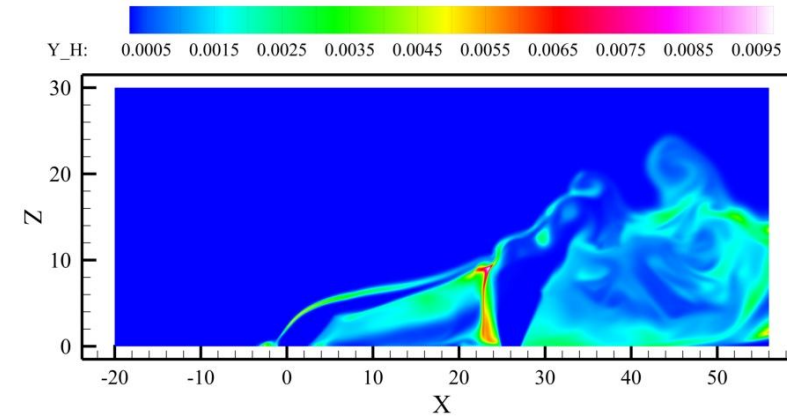

(b)

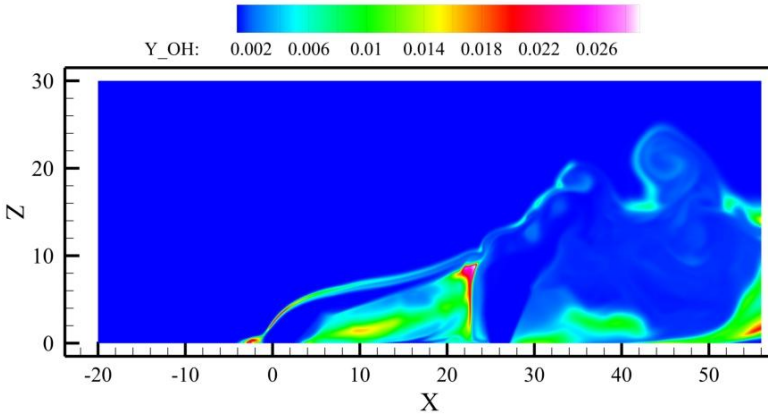

Figure 8.8: Spatial distributions of (a) H, and (b) OH mass fraction at y = 15 mm plane obtained at 45 μs from the beginning of the simulation.

8.3.2 Effect of nanosecond discharges on O atom concentration

In order to improve the ignition of H_2 jets injected into the supersonic O_2 crossflow, the potential of nanosecond discharges was investigated. As explained in Sec. 8.2.6, the discharge is numerically treated using a reduced order model. Plasma is assumed to be produced during each nanosecond voltage pulse in a cubic region between the two electrodes, of dimensions 6×2×2 mm^3. The E/N and electron density are fixed at constant values of 300 Td and 10^{14} cm^{-3} in the discharge domain during the voltage pulse. The pulse duration is taken as 20 ns, and the repetition frequency is fixed at 100 kHz. By doing so, we are effectively considering only the plasma kinetic effect in the present

work. The ion Joule heating near the electrodes are not considered. Electron impact dissociation of O_2 and H_2 were included in the chemistry mechanism.

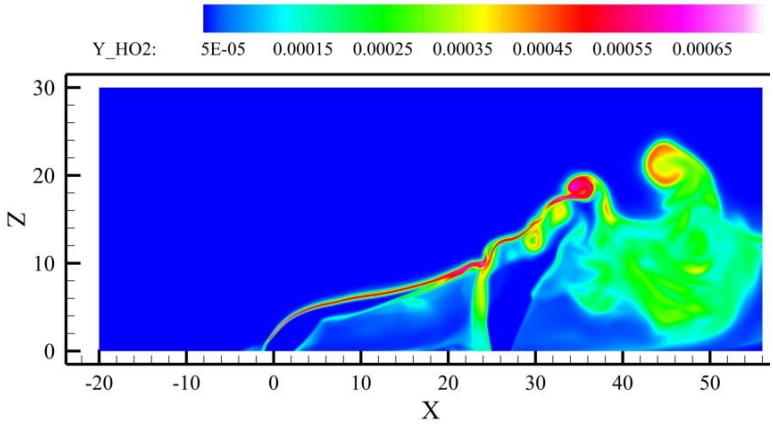

(a)

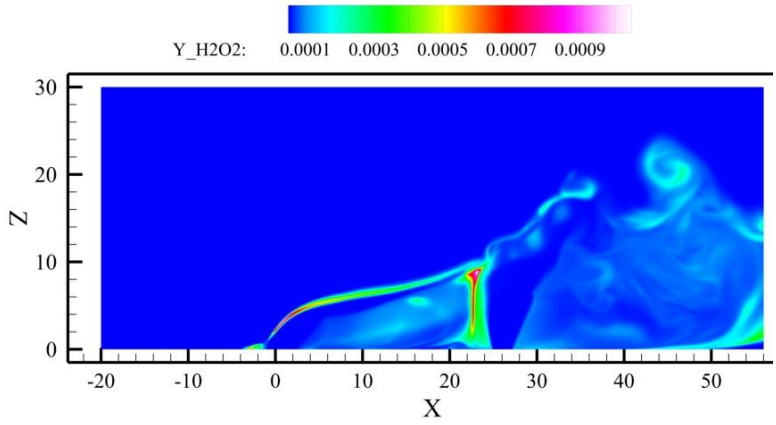

(b)

Figure 8.9: Spatial distributions of (a) HO_2, and (b) H_2O_2 mass fraction at y = 15 mm plane obtained at 45 µs from the beginning of the simulation.

The fuel mass fractions in the discharge region are negligible as seen in Fig. 8.4. Hence, the plasma effect was completely related to generation of O atoms from electron impact dissociation of O_2 during the voltage pulses. Figure 8.10 show the spatial distribution of O mass fractions after 6 µs (1 pulse), 20 µs (2 pulses), and 33 µs (3 pulses) from the beginning of the simulation. In Fig. 8.10(a), we can observed the O atoms

produced during the first voltage pulse moving downstream because of the crossflow. Atomic oxygen is produced in the cubic region between x = 10 and x = 16 mm locations. In 6 μs, the plasma produced radicals convect nearly 6 mm, reaching the left rim of the second injector. Fig. 8.10(b) shows the spatial distribution at a later time. Atomic oxygen freshly generated by the 2^{nd} pulse can be observed in the discharge domain. At this juncture, the radicals generated from the previous pulse reach the downstream jet region. At 33 μs, the mixing and combustion occurring downstream of the second jet generates O atoms. However, atomic oxygen produced in the region between the two jets is almost exclusively from the plasma pulses.

Figure 8.11 compares the spatial O atom distributions with and without the nanosecond discharges on the x-z plane at y = 15 mm location at 33 μs after the beginning of the simulation. It is clear that the plasma discharges have a significant impact on the O atom concentration in the region between the two jets. With the plasma pulses, the average concentration of atomic oxygen in the discharge domain is close to 0.05. The nanosecond discharges, however, have almost no impact on the O atom distribution downstream of the second jet. We also observed that the plasma has no effect on the distributions of other species including H_2O in the entire computational domain. We believe the reason for this behavior is the high jet momentum ratios considered in the present study. The plasma generated radicals are unable to have an effect on the flame development downstream because of the strong penetration of the cold fuel jet.

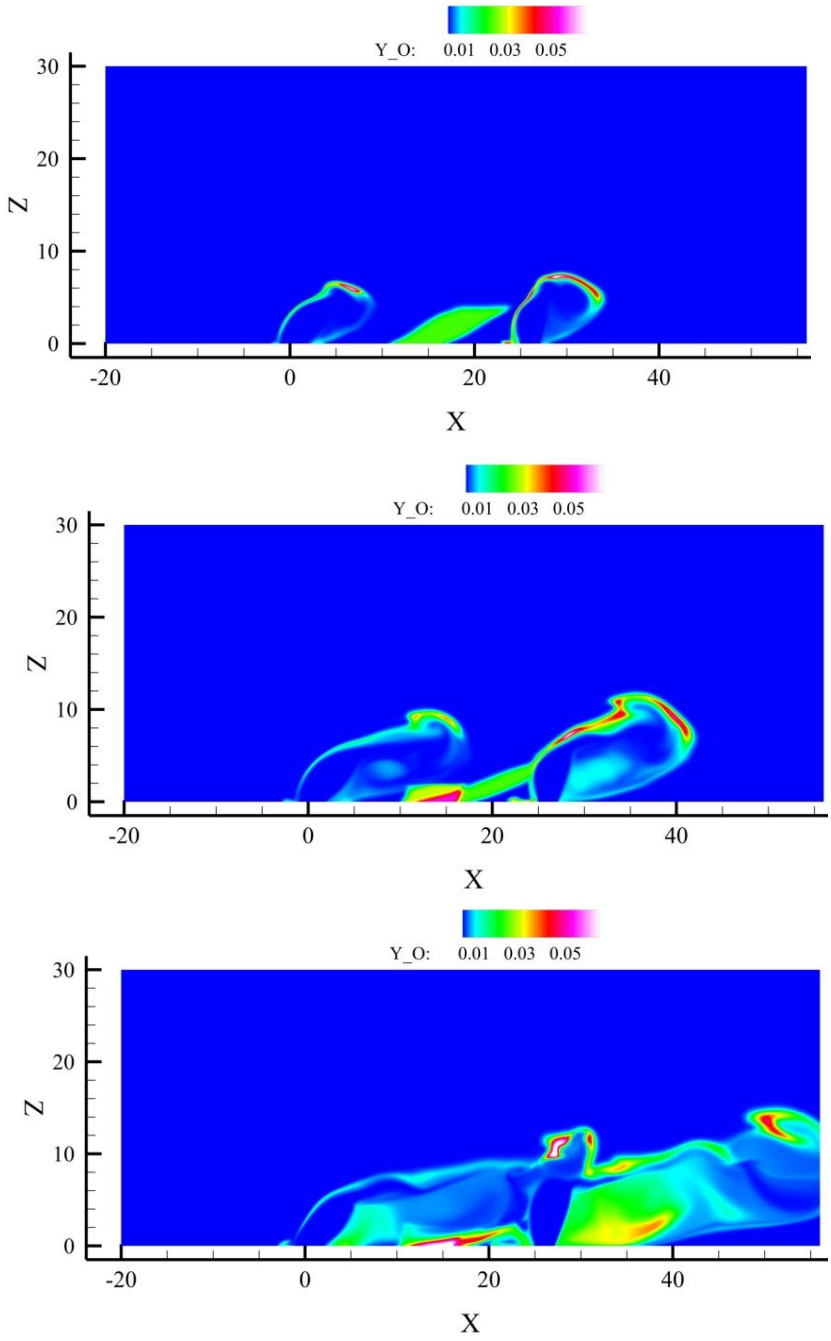

Figure 8.10: Spatial distributions of O mass fraction at y = 15 mm plane obtained at (a) 6 µs, (b) 20 µs, and (c) 33 µs from the beginning of the simulation, with application of the nanosecond voltage pulses at a pulsing rate of 100 kHz.

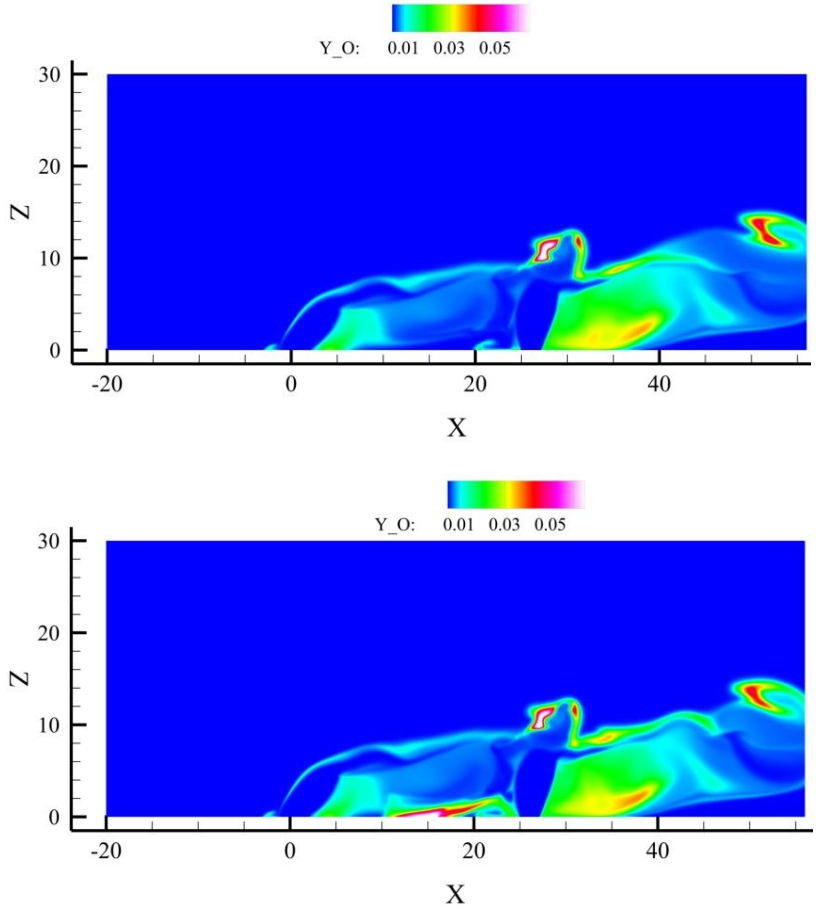

Figure 8.11: Spatial distributions of O mass fraction at y = 15 mm plane obtained at 33 μs (a) without, and (b) with application of the nanosecond voltage pulses at a pulsing rate of 100 kHz.

8.4 Conclusions

The ignition and combustion of H_2 jets injected into a supersonic O_2 crossflow was studied using high fidelity Large Eddy Simulations. Nanosecond plasma discharges were studied for their potential to produce radicals and impact on the flame-holding process. A subsonic H_2 jet was injected at an angle of 60 to the vertical axis upstream of the plasma zone, whereas a sonic jet was injected transversely downstream, with the jet momentum ratios of 3.5 and 9.5 respectively. Ignition was observed in the leeward side of the second injector where a strong recirculation region exists due to jet penetration and

separation of the boundary layer. The cold transverse jet inhibited the spreading of the flame because of the high jet momentum ratio. As a consequence only a weak flame with moderate to low concentrations of H_2O was observed downstream of the second jet. The plasma discharge was simulated using a reduced-order plasma model. The discharge domain was assumed to be a cube with pre-specified constant values of E/N and electron density. It was observed that atomic oxygen was the primary radical produced by the plasma pulses through electron impact dissociation of O_2. The plasma had a significant effect on the O atom distribution near the discharge domain as well as in the leeward side of the second jet. The other species distributions, however, remained unchanged with or without plasma. We believe the reason for this behavior was the high jet momentum ratios considered in the present study. The plasma generated radicals were unable to have an effect on the flame development downstream because of the strong penetration of the cold fuel jet.

In a future work, we will explore the plasma effect at lower jet momentum ratios, where the radicals and heat generated in the discharge domain can be effectively transported downstream of the second jet to provide effective flame holding capability.

CHAPTER 9

CONCLUSIONS

This dissertation established a multi-scale modeling framework to simulate the physical and chemical effects of nonequilibrium, nanosecond plasma discharges on reacting flows. Equations for charged and neutral species, electric field and electron energy were solved. In addition, conservation equations for mass, momentum and energy were considered to simulate flow dynamics. The electron transport and reaction rate coefficients were calculated as functions of electron energy in advance using a Boltzmann equation solver, BOLSIG [17]. During the simulation, the coefficients were read from a lookup table and interpolated every timestep. The model was capable of resolving electric field transients and electron impact dynamics in sub-*ns* timescales, as well as calculating the cumulative effects of multiple discharge pulses over *ms* timescales. Detailed chemistry mechanisms were incorporated to provide deep insight into the plasma kinetic pathways.

A comprehensive analysis was performed to study the dynamics of energy coupling, gas heating, and generation of active species by repetitively pulsed nanosecond dielectric barrier discharges (NS DBD) in air. The simulations were performed with pressures between 40 and 100 *torr*, and pulsing frequency in the range of $1\text{-}10^5$ *Hz*. Results show good agreement with measurements of coupled energy, O atom density, and temperature in the discharge. The input electrical energy is directly proportional to the number density, and remains fairly constant on a per molecule basis from pulse to pulse. Repetitive pulsing causes uniform production of atomic oxygen in the discharge volume

via electron impact dissociation during voltage pulses, and through quenching of excited nitrogen molecules in the afterglow. A uniform temperature profile developed in the discharge volume after multiple pulses (~100 pulses) as a consequence of the chemical heat release from quenching of excited species.

One-dimensional simulations were conducted to provide insight into the ignition of H_2-air mixtures excited by pulsed nanosecond dielectric barrier discharges. The gas mixture was mildly preheated (400-500 K) to create diffuse and uniform plasma in a parallel plate discharge cell. The studies were performed in a decaying plasma after a burst of high-voltage pulses. A reduced chemistry mechanism consisting of 19 species and 112 reactions was inferred through sensitivity analysis. The model predictions showed good agreement with OH concentration, temperature and ignition delay measurements. The ignition characteristics were highly sensitive to input plasma energy. The effectiveness of plasma generated radicals in triggering partial fuel oxidation was found to depend on the temperature at the end of the pulse burst (T_f). When T_f exceeded 700 K, the temperature continued to rise even after the plasma source was switched off. Acceleration of the conventional H_2-O_2 chain branching pathways resulted in ignition after a short time delay after the burst. Both ICCD camera images and model predictions showed that ignition first occurs at the center of the discharge volume. The kernel, however, expanded rapidly towards the boundaries at a speed of ~30 ms^{-1}. The expansion rate of the ignition kernel remained unaltered even when the heat transport coefficients were reduced by a factor of 100 in the model. This suggested that the ignition kernel growth is primarily due to local plasma chemistry effects rather than flame propagation, and heat transport does not play a significant role. The nanosecond pulse discharge

plasma excitation resulted in nearly simultaneous ignition over a large volume, in sharp contrast to hot-spot igniters.

An effective numerical strategy was proposed to expedite the simulations of nanosecond repetitively pulsed discharges (NRPD) without compromise on the solution accuracy. The "frozen electric field" modeling approach was based on the periodic nature of NRPD, wherein the electrical characteristics reached a stationary state after a few voltage pulses. The spatial distributions and temporal evolution of the electric field, electron density and electron energy were stored in a lookup library. The subsequent pulses were simulated by freezing the electrical properties to the values in the library. This allowed for the timestep size to be increased by four orders of magnitude from 10^{-13}s to 10^{-9}s. It was found that the frozen model was 5 times faster than the complete model in simulating 50 pulses, and showed a speedup of upto 30 times for large scale simulations (200 - 300 pulses). The simulation results compared favorably with the complete plasma model predictions, and showed good agreement with the ignition delay and temperature measurements of H_2-air mixtures subjected to pulsed nanosecond dielectric barrier discharges at different pressures (54 - 144 torr), and equivalence ratios (0.7 - 1.2).

The effect of non-equilibrium, nanosecond pulsed plasma discharges on the ignition characteristics of nC_7H_{16} and air was studied by means of a self-consistent numerical analysis at a reduced pressure of 20.3 kPa. The plasma generated radicals initiated and significantly accelerated the H abstraction reaction from fuel molecules and triggered a "self-accelerating" feedback loop via low-temperature kinetic pathways. Application of only a few discharge pulses at the beginning was sufficient to reduce the initiation time of the first-stage temperature rise by a factor of 10. The plasma effect on

the low temperature chemistry was independent of the equivalence ratio, but became more pronounced at lower initial temperatures (550-650 K). A staggered application of discharge pulses (a few pulses at the beginning and a larger number of pulses immediately after the first-stage temperature rise) was found to be optimal, reducing the ignition delay by nearly 40%. The plasma effect after the first stage was shown to be predominantly thermal. Temperature rise, introduced by quenching of excited species, radical induced fuel oxidation and radical/ion-electron recombination, accelerated the decomposition of H_2O_2 and reduced the induction period before ignition. NO produced by plasma pulses reacted with HO_2 at low temperatures to generate OH, which accelerated the low temperature nC_7H_{16} ignition. This work also demonstrated that non-equilibrium plasma can dramatically modify the time scales of fuel kinetics, and therefore can be used to control the ignition timing for advanced engine technologies.

A novel plasma-flame modeling framework has been developed to study the direct coupling of steady, laminar, low-pressure, premixed flames to highly non-equilibrium, nanosecond-pulsed plasma discharges. A one-dimensional, multi-scale, pulsed discharge modeling framework with detailed plasma combustion kinetics was used to develop insight into the complex plasma- flame interactions. The calculations were performed with and without a burst of 200 nanosecond discharge pulses to quantify the effect of non-equilibrium plasma on a pre-existing lean premixed $H_2/O_2/N_2$ ($\phi = 0.5$) flame. Temperature increased by approximately 20% at all spatial locations and OH mole fraction increased by 100-500 % in the preheat region and 40% in the post-flame gases due to the application of discharge pulses. Simulation results showed a significant increase in O and H densities due to plasma chemistry, with peak values increasing by a

factor of 6 and a factor of 4, respectively. Joule heating was found responsible for a significant fraction of the plasma enhancement of the combustion processes, although electron impact processes were shown to play an important role in radical production and heat release in the pre-heat zone. It was demonstrated that Joule heating alone cannot move the temperature and species profiles as far upstream (i.e. closer to the burner surface) as the pulsed plasma source of the same total power.

The ignition and combustion of H_2 jets injected into a supersonic O_2 crossflow was studied using high fidelity Large Eddy Simulations. Nanosecond plasma discharges were studied for their potential to produce radicals and impact on the flame-holding process. A subsonic H_2 jet was injected at an angle of 60 to the vertical axis upstream of the plasma zone, whereas a sonic jet was injected transversely downstream, with the jet momentum ratios of 3.5 and 9.5 respectively. Ignition was observed in the leeward side of the second injector where a strong recirculation region exists due to jet penetration and separation of the boundary layer. The cold transverse jet inhibited the spreading of the flame because of the high jet momentum ratio. As a consequence only a weak flame with moderate to low concentrations of H_2O was observed downstream of the second jet. The plasma discharge was simulated using a reduced-order plasma model. The discharge domain was assumed to be a cube with pre-specified constant values of E/N and electron density. It was observed that atomic oxygen was the primary radical produced by the plasma pulses through electron impact dissociation of O_2. The plasma had a significant effect on the O atom distribution near the discharge domain as well as in the leeward side of the second jet. The other species distributions, however, remained unchanged with or without plasma. We believe the reason for this behavior was the high jet momentum

ratios considered in the present study. The plasma generated radicals were unable to have an effect on the flame development downstream because of the strong penetration of the cold fuel jet.

REFERENCES

[1] Birol, F. (2010). World energy outlook 2010. *International Energy Agency*.

[2] Newell, R. G., and Iler, S. (2013). *The global energy outlook* (No. w18967). National Bureau of Economic Research.

[3] Curran, E. T. (2001). Scramjet engines: the first forty years. *Journal of Propulsion and Power*, *17*(6), 1138-1148.

[4] Ben-Yakar, A., & Hanson, R. K. (2001). Cavity flame-holders for ignition and flame stabilization in scramjets: an overview. *Journal of Propulsion and Power*, *17*(4), 869-877.

[5] S. M. Starikovskaia. Plasma assisted ignition and combustion. *Journal of Physics D-Applied Physics*, 39(16): R265-R299, 2006.

[6] A. Starikovskiy and N. Aleksandrov. Plasma-assisted ignition and combustion. *Progress in Energy and Combustion Science*, 39(1):61-110, 2013.

[7] A. Dutta, Z. Yin, and I. V. Adamovich. Cavity ignition and flameholding of ethylene-air and hydrogen-air fows by a repetitively pulsed nanosecond discharge. *Combustion and Flame*, 158(8):1564-1576, 2011.

[8] S. B. Leonov, D. A. Yarantsev, A. P. Napartovich, and I. V. Kochetov. Plasma-assisted combustion of gaseous fuel in supersonic duct. *Plasma Science, IEEE Transactions on*, 34(6):2514-2525, 2006.

[9] S. B. Leonov, D. A. Yarantsev, A. P. Napartovich, and I. V. Kochetov. Plasma-assisted chemistry in high-speed flow. *Plasma Science and Technology*, 9(6):760, 2008.

[10] C. D. Cathey, T. Tang, T. Shiraishi, T. Urushihara, A. Kuthi, and M. A. Gundersen. Nanosecond plasma ignition for improved performance of an internal combustion engine. *Plasma Science, IEEE Transactions on*, 35(6):1664{1668, 2007.

[11] K. Criner, A. Cessou, J. Louiche, and P. Vervisch. Stabilization of turbulent lifted jet flames assisted by pulsed high voltage discharge. *Combustion and flame*, 144(1-2), 2006.

[12] W. Kim, H. Do, M. G. Mungal, and M. A. Cappelli. Plasma-discharge stabilization of jet diffusion flames. *IEEE Transactions on Plasma Science*, 34(6):2545-2551, 2006.

[13] F, Wang, J. B. Liu, J. Sinibaldi, C. Brophy, A. Kuthi, C. Jiang, P. Ronney, and M. A. Gundersen. Transient plasma ignition of quiescent and owing air/fuel mixtures. *IEEE Transactions on Plasma Science*, 33(2):844-849, 2005.

[14] E. S. Stockman, S. H. Zaidi, R. B. Miles, C. D. Carter, and M. D. Ryan. Measurements of combustion properties in a microwave enhanced flame. *Combustion and Flame*, 156(7):1453-1461, 2009.

[15] T. Ombrello, Y. Ju, and A. Fridman. Kinetic ignition enhancement of diffusion flames by nonequilibrium magnetic gliding arc plasma. *AIAA Journal*, 46(10):2424-2433, 2008.

[16] Raizer, Y. P., and Allen, J. E. (1991). *Gas discharge physics* (Vol. 1). Berlin: Springer-Verlag.

[17] G. J. M. Hagelaar and L. C. Pitchford. Solving the Boltzmann equation to obtain electron transport coefficients and rate coefficients for fluid models. *Plasma Sources Science and Technology*, 14(4):722, 2005.

[18] Montello A, Yin Z, Burnette D, Adamovich I and Lempert W 2012 Picosecond CARS Measurements of Nitrogen Vibrational Loading and Rotational/Translational

Temperature In Non-Equilibrium Discharges In: *50th AIAA Aerospace Sciences Meeting*, Nashville, Tennessee
[19] Starikovskaia, S. M., Starikovskii, A. Y., & Zatsepin, D. V. (2001). Hydrogen oxidation in a stoichiometric hydrogen-air mixture in the fast ionization wave. *Combustion Theory and Modelling*, *5*(1), 97-129.
[20] Bozhenkov, S. A., Starikovskaia, S. M., & Starikovskiia, A. Y. (2003). Nanosecond gas discharge ignition of H_2- and CH_4− containing mixtures. *Combustion and flame*, *133*(1), 133-146.
[21] G. P. Smith, D. M. Golden, M. Frenklach, N. W. Moriarty, B. Eiteneer, M. Goldenberg, C. T. Bowman, R. K. Hanson, S. Song, W. C. Gardiner, Jr., V. V. Lissianski, and Z. Qin http://www.me.berkeley.edu/gri_mech/
[22] Kosarev, I. N., Aleksandrov, N. L., Kindysheva, S. V., Starikovskaia, L. S., & Starikovskii, A. Y. (2009). Kinetics of ignition of saturated hydrocarbons by nonequilibrium plasma: C_2H_6 to C_5H_{12} containing mixtures. *Combustion and flame*, *156* (1), 221-233.
[23] Lou, G., Bao, A., Nishihara, M., Keshav, S., Utkin, Y. G., Rich, J. W. Lempert, W., and Adamovich, I. V. (2007). Ignition of premixed hydrocarbon–air flows by repetitively pulsed, nanosecond pulse duration plasma. *Proceedings of the Combustion Institute*, *31*(2), 3327-3334.
[24] Mintusov, E., Serdyuchenko, A., Choi, I., Lempert, W. R., & Adamovich, I. V. (2009). Mechanism of plasma assisted oxidation and ignition of ethylene–air flows by a repetitively pulsed nanosecond discharge. *Proceedings of the Combustion Institute*, *32*(2), 3181-3188.
[25] Uddi, M., Jiang, N., Mintusov, E., Adamovich, I. V., & Lempert, W. R. (2009). Atomic oxygen measurements in air and air/fuel nanosecond pulse discharges by two photon laser induced fluorescence. *Proceedings of the Combustion Institute*, *32*(1), 929-936.
[26] Tan, Y., Fotache, C. G., & Law, C. K. (1999). Effects of NO on the ignition of hydrogen and hydrocarbons by heated counterflowing air. *Combustion and flame*, *119*(3), 346-355.
[27] Uddi, M., Jiang, N., Adamovich, I. V., & Lempert, W. R. (2009). Nitric oxide density measurements in air and air/fuel nanosecond pulse discharges by laser induced fluorescence. *Journal of Physics D: Applied Physics*, *42*(7), 075205.
[28] Yin, Z., Takashima, K., & Adamovich, I. V. (2011). Ignition time measurements in repetitive nanosecond pulse hydrogen–air plasmas at elevated initial temperatures. *Plasma Science, IEEE Transactions on*, *39*(12), 3269-3282.
[29] Choi, I., Yin, Z., Adamovich, I. V., & Lempert, W. R. (2011). Hydroxyl radical kinetics in repetitively pulsed hydrogen–air nanosecond plasmas. *Plasma Science, IEEE Transactions on*, *39*(12), 3288-3299.
[30] Takashima, K., Yin, Z., & Adamovich, I. V. (2013). Measurements and kinetic modeling of energy coupling in volume and surface nanosecond pulse discharges. *Plasma Sources Science and Technology*, *22*(1), 015013.
[31] Yin, Z., Adamovich, I. V., & Lempert, W. R. (2013). OH radical and temperature measurements during ignition of H_2-air mixtures excited by a repetitively pulsed nanosecond discharge. *Proceedings of the Combustion Institute*, *34*(2), 3249-3258.

[32] Ombrello, T., Qin, X., Ju, Y., Gutsol, A., Fridman, A., & Carter, C. (2006). Combustion enhancement via stabilized piecewise nonequilibrium gliding arc plasma discharge. *AIAA journal*, *44*(1), 142-150.
[33] Sun, W., Uddi, M., Ombrello, T., Won, S. H., Carter, C., & Ju, Y. (2011). Effects of non-equilibrium plasma discharge on counterflow diffusion flame extinction. *Proceedings of the Combustion Institute*, *33*(2), 3211-3218.
[34] Sun, W., Won, S. H., Ombrello, T., Carter, C., & Ju, Y. (2013). Direct ignition and *S*-curve transition by *in situ* nano-second pulsed discharge in methane/oxygen/helium counterflow flame. *Proceedings of the Combustion Institute*, *34*(1), 847-855.
[35] Sun, W., Won, S. H., & Ju, Y. (2014). *In situ* plasma activated low temperature chemistry and the *S*-curve transition in DME/oxygen/helium mixture. *Combustion and Flame*.
[36] Pilla, G., Galley, D., Lacoste, D. A., Lacas, F., Veynante, D., and Laux, C. O., "Plasma-Enhanced Combustion of a Lean Premixed Air-Propane Turbulent Flame using a Repetitively Pulsed Nanosecond Discharge", IEEE Transactions on Plasma Science, vol. 34, pp. 2471- 2477, 2006.
[37] Pancheshnyi, S., Lacoste, D. A., Bourdon, A., and Laux, C.O., "Ignition of Propane-Air Mixtures by a Repetitively Pulsed Nanosecond Discharge," IEEE Transactions on Plasma Science, vol. 34, pp. 2478-2487, 2006.
[38] Pai, D. Z., Lacoste, D. A., and Laux, C. O., 'Transitions between corona, glow, and spark regimes of nanosecond repetitively pulsed discharges in air at atmospheric pressure," J. Appl. Phys., 107, 093303, 2010 (15 p).
[39] Stancu, G. D., Kaddouri F., Lacoste D. A., Laux C. O., "Atmospheric pressure plasma diagnostics by OES, CRDS and TALIF," J. Phys. D: Appl. Phys., 43, 124002, 2010 (10 p)
[40] Lacoste, D. A., Xu, D. A., Moeck, J. P., and Laux, C. O., "Dynamic response of a weakly turbulent lean-premixed flame to nanosecond repetitively pulsed discharges," Proceedings of the Combustion Institute, Vol. 34, pp 3259-3266, 2013.
[41] Lacoste, D. A., Moeck, J. P., Durox, D., Laux, C. O., Schuller, T., "Effect of Nanosecond Repetitively Pulsed Discharges on the Dynamics of a Swirl-Stabilized Lean Premixed Flame," Journal of Engineering for Gas Turbines and Power, Vol. 135 / 101501-7, October 2013.
[42] Do, H., Mungal, M. G., & Cappelli, M. A. (2008). Jet flame ignition in a supersonic crossflow using a pulsed nonequilibrium plasma discharge. *Plasma Science, IEEE Transactions on*, *36*(6), 2918-2923.
[43] Do, H., Im, S. K., Cappelli, M. A., & Mungal, M. G. (2010). Plasma assisted flame ignition of supersonic flows over a flat wall. *Combustion and Flame*, *157*(12), 2298-2305.
[44] Kim, W., Do, H., Mungal, M. G., & Cappelli, M. A. (2006). Plasma-discharge stabilization of jet diffusion flames. *Plasma Science, IEEE Transactions on*, *34*(6), 2545-2551.
[45] Macheret S O, Shneider M N and Miles R B 2002 Modeling of air plasma generation by repetitive high-voltage nanosecond pulses *Plasma Science, IEEE Transactions on* **30** 1301-14

[46] Pancheshnyi S, Nudnova M and Starikovskii A 2005 Development of a cathode-directed streamer discharge in air at different pressures: Experiment and comparison with direct numerical simulation *Phys Rev E* **71**
[47] Unfer T and Boeuf J P 2009 Modelling of a nanosecond surface discharge actuator *J Phys D Appl Phys* **42**
[48] Poggie J, Adamovich I V, Bisek N and Nishihara M 2013 numerical simulation of nanosecond pulse electrical discharges *Plasma Sources Sci T* **22** 015001
[49] Breden D, Miki K, and Raja L 2011 Computational study of cold atmospheric nanosecond pulsed helium plasma jet in air *Applied Physics Letters* **99** 111501
[50] Tholin F, and Bourdon A 2013 Simulation of the stable 'quasi-periodic'glow regime of a nanosecond repetitively pulsed discharge in air at atmospheric pressure. *Plasma Sources Science and Technology* **22** 045014.
[51] Hsieh S Y and Vigor Y 1997 A preconditioned flux-differencing scheme for chemically reacting flows at all Mach numbers *International Journal of Computational Fluid Dynamics* **8** 31-49
[52] Davoudabadi M, Shrimpton J and Mashayek F 2009 On accuracy and performance of high-order finite volume methods in local mean energy model of non-thermal plasmas *Journal of Computational Physics* **228** 2468-79
[53] Gogolides E and Sawin H H 1992 Continuum modeling of radio-frequency glow discharges. I. Theory and results for electropositive and electronegative gases *J Appl Phys* **72** 3971-87
[54] Wang Q, Economou D J and Donnelly V M 2006 Simulation of a direct current microplasma discharge in helium at atmospheric pressure *J Appl Phys* **100** 023301--10
[55] Incropera F D, Bergman D and Lavine T A.(2007) Fundamentals of Heat and Mass Transfer *John Wiley & Sons.*
[56] Itikawa Y 2006 Cross sections for electron collisions with nitrogen molecules *Journal of physical and chemical reference data* **35** 31-54
[57] Sieck L W, Heron J T and Green D S 2000 Chemical Kinetics Database and Predictive Schemes for Humid Air Plasma Chemistry. Part I: Positive Ion–Molecule Reactions *Plasma Chem Plasma P* **20** 235-58
[58] Montello A, Yin Z, Burnette D, Adamovich I and Lempert W 2012 Picosecond CARS Measurements of Nitrogen Vibrational Loading and Rotational/Translational Temperature In Non-Equilibrium Discharges In: *50th AIAA Aerospace Sciences Meeting,* Nashville, Tennessee
[59] Popov N A 2008 Effect of a pulsed high-current discharge on hydrogen-air mixtures. *Plasma Physics Reports,* **34** 376-391.
[60] Konnov A A 2008 Remaining uncertainties in the kinetic mechanism of hydrogen combustion. *Combustion and flame,* **152** 507-528.
[61] Smith G P, Golden D M, Franklach M, et al. 1999 GRI-Mech 3.0, available at http://www.me.berkeley.edu/gri_mech/
[62] Takita K, Abe N, Masuya G, and Ju Y, 2007 Ignition enhancement by addition of NO and NO_2 from a N_2/O_2 plasma torch in a supersonic flow, *Proc. Combust. Inst.* **31** 2489-2496.
[63] Ju Y, Sun W, Burke M P, Gou X, Chen Z, 2011 Multi-timescale modeling of ignition and flame regimes of n-heptane-air mixtures near spark assisted homogeneous charge compression ignition conditions. *Proc. Combust. Inst.* 33 1245-1251.

[64] Seiser H, Pitsch H, Seshadri K, Pitz W J, and Curran H J, 2000 Extinction and autoignition of n-heptane in counterflow configuration *Proc. Combust. Inst.* **28** 2029-2037.
[65] Ionin, A. A., Kochetov, I. V., Napartovich, A. P., & Yuryshev, N. N. 2007. Physics and engineering of singlet delta oxygen production in low-temperature plasma. *Journal of Physics D: Applied Physics*, 40 R25.
[66] Phelps, A. V., & Pitchford, L. C. 1985. Anisotropic scattering of electrons by N_2 and its effect on electron transport. *Physical Review A*, **31**, 2932.
[67] M. Hayashi, in: L.C. Pitchford, B.V. McCoy, A. Chutjian, S. Trajmar (Eds.), *Swarm Studies and Inelastic Electron–molecule Collisions*, Springer Verlag, New York, 1987, pp. 167-187.
[68] Haydon S and Williams O 2001 Combined spatial and temporal studies of ionization growth in nitrogen *Journal of Physics D: Applied Physics* **9** 523
[69] Tarasenko V F and Yakovlenko S. I. 2007 The electron runaway mechanism in dense gases and the production of high-power subnanosecond electron beams *Physics-Uspekhi* **47** 887
[70] Tkachev A N and Yakovlenko S. I. 2004 Runaway of electrons in dense gases and mechanism of generation of high-power subnanosecond beams *Central European Journal of Physics* **2** 579-635
[71] Viehland, L. A., & Mason, E. A. 1995 Transport properties of gaseous ions over a wide energy range, IV. *Atomic Data and Nuclear Data Tables*, **60**, 37-95.
[72] Nelson, D., Benhenni, M., Eichwald, O., & Yousfi, M., 2003 Ion swarm data for electrical discharge modeling in air and flue gas mixtures. *Journal of applied physics*, **94**, 96-103.
[73] R. J. Kee, F. M. Rupley, J. A. Miller, et al. TRANSPORT: A software package for the evaluation of gas-phase, multicomponent transport properties, CHEMKIN Collection, Release 3.6, Reaction Design, Inc., San Diego, CA (2000).
[74] Kulikovsky A 1999 Two-dimensional simulation of the positive streamer in N_2 between parallel-plate electrodes *Journal of Physics D: Applied Physics* **28** 2483
[75] Hindmarsh A C, Brown P N, Grant K E, Lee S L, Serban R, Shumaker D E and Woodward C S 2005 SUNDIALS: Suite of nonlinear and differential/algebraic equation solvers *ACM Transactions on Mathematical Software (TOMS)* **31** 363-96
[76] Arslanbekov R R and Kolobov V I 2003 Two-dimensional simulations of the transition from Townsend to glow discharge and subnormal oscillations *Journal of Physics D: Applied Physics* **36** 2986
[77] Adamovich I V, Nishihara M, Choi I, Uddi M and Lempert W R 2009 Energy coupling to the plasma in repetitive nanosecond pulse discharges *Physics of Plasmas* **16** 113505
[78] M. Kuznetsov, S. Kobelt, J. Grune, and T. Jordan, Flammability limits and laminar flame speed of hydrogen-air mixtures at sub-atmospheric pressures. *International Journal of Hydrogen Energy*, 37(22):17580-17588, 2012.
[79] T. Li, I.V. Adamovich, and J. A. Sutton, 2013 A Burner Platform for Examining the Effects of Non-Equilibrium Plasmas on Oxidation and Combustion Chemistry *Combustion Science and Technology* 185 990-998.

[80] Gruber, M. R., Donbar, J. M., Carter, C. D., & Hsu, K. Y. (2004). Mixing and combustion studies using cavity-based flameholders in a supersonic flow. *Journal of Propulsion and Power*, *20*(5), 769-778.
[81] Anderson, C. D., & Schetz, J. A. (2005). Liquid-fuel aeroramp injector for scramjets. *Journal of propulsion and power*, *21*(2), 371-374.
[83] Zhang, L., and Yang V., Flow Dynamics and Mixing of a Sonic Jet in Supersonic Crossflow AIAA 2012 - 0478.
[84] Santiago, J. G., and Dutton, J. C. (1997). Velocity measurements of a jet injected into a supersonic crossflow. *Journal of Propulsion and Power*, *13*(2), 264-273.
[85] Génin, F., and Menon, S. (2010). Dynamics of sonic jet injection into supersonic crossflow. *Journal of Turbulence*, (11).